Nanoparticle Synthesis For Magnetic Hyperthermia

This thesis is submitted in partial fulfilment of the requirements for the Degree of Doctor of Philosophy (Chemistry)

Luanne Alice Thomas

Supervised by Professor I. P. Parkin

University College London
Christopher Ingold Laboratories,
20 Gordon Street,
WC1H 0AJ

2010

I, Luanne A. Thomas, confirm that the work presented in this thesis is my own. Where information has been derived from other sources, I confirm that this has been indicated in the thesis.

Abstract

This work reports on an investigation into the synthesis, control, and stabilisation of iron oxide nanoparticles for biomedical applications using magnetic hyperthermia. A new understanding of the factors effecting nanoparticle growth in a coprecipitation methodology has been determined. This thesis challenges the highly cited Ostwald Ripening as the primary mechanism for nanoparticulate growth, and instead argues that in certain conditions, such as increasing reaction temperature, a coalescence mechanism could be favoured by the system. Whereas in a system with a slower rate of addition of the reducing agent, Ostwald ripening is the favoured mechanism.

The iron oxide nanoparticles made in the study were stabilised and functionalised for the purpose of stability in physiological environments using either carboxylic acid or phosphonate functionalised ligands. It was shown that phosphonate ligands form a stronger attachment to the nanoparticle surface and promote increased stability in aqueous solutions, however, this affected the magnetic properties of the particles and made them less efficient heaters when exposed to an alternating magnetic fields. Tiopronin coated iron oxide nanoparticles were a far superior heater, being over four times more effective than the best commercially available product. Due to its strong response, experiments into the antimicrobial properties of tiopronin coated iron oxide nanoparticles were undertaken, specifically on *Staphylococcus aureus*, to our knowledge this is the first time magnetic hyperthermia has been used for such an application. At concentrations of 50 mg/ml the sample was capable of complete bacterial kills following exposure to the in-house magnetic hyperthermia MACH system. Aging and oxidation over a period of a month did decrease the performance of the particles to kill bacteria using MACH heating, however they were still shown to be effective in killing *Staphylococcus aureus*.

Acknowledgements

I would like to thank my supervisor, Prof. Ivan P. Parkin, for all of his advice and guidance. He has always been so encouraging and has always had the time to talk. He really does prove that nice guys do not finish last, and I thank him for all he has done for me. I would also like to extend my gratitude to my secondary supervisor Prof. Quentin Pankhurst whose enthusiasm for the project is infectious and for the knowledge he has passed on to me. I truly hope the project goes from strength to strength.

I whole heartedly thank Dr Caroline Knapp, she has always had time to help me in the Lab. She had the patience to teach me air sensitive chemistry from scratch and has always been there to assist me. She has become a dear friend to me and I will always be grateful to her for her enduring support and friendship. Special thanks also go to Dr Kris Page, I am so glad you decided to take the Post Doc and your starting really invigorated my energy for the project at a time when it was at a low. Thanks also goes to Dr Geoff Hyett, a clever man with great humility, who has always had the time to help me and teach me something new, particularly when it comes to diffraction!

I would like to thank Dr Steve Firth for his help with TGA and Raman whenever I have needed him. I thank Jill Maxwell for elemental analysis and Linda Dekker for the antimicrobial work. I thank Salim for teaching me antimicrobial techniques with great patience. Thanks goes to Dr Ian Watts who, at the last moment, ran lots of samples on the SQUID for me. I also thank Dr Mathew Kallumdail for SQUID and for useful discussions, and Dr Khuloud Al-Jamal for TEM and some DLS measurements. I would also like to extend my thanks for Mr Dave Knapp, who has always gone above and beyond the call of duty with any technical problems I have had.

I also sincerely thank my friends, past and present, from 308, who have made everyday one that is filled with laughter. Specifically I would like to thank; Dr Naima Narband, Dr Stephen Potts, Dr Russell Binions, Dr Charlie Dunnill, Dr David Pugh, Paolo Melgari, Mathew Waugh, Tegan Thomas, Colin Crick, Sanjayan Sathasivam, Savio Moniz, Davinder Bhachu, Ralph Leech, Leanne Bloor and Charlie Hunston. I also thank all the members of the Grand Challenge project, notably; Prof. Kerry Chester, Dr Paul Southern, Dr Kim Vigor and Bettina Berndl.

I truly thank my wonderfully supportive friends, who have provided so much encouragement. An extra special mention goes to Kate, Emily, Josephine, Karen, Matt, Paul, the Dorcan girls, Ian, Marc, Steve and Ellie. Thanks also to the new friends I have made in London and have made my time here unforgettable.

Finally, and of most importance I thank Mum, Dad, Adam and Kevin. What you have done for me is beyond the scope of the words in this acknowledgment. Mum and Dad, thanks so much for giving me such amazing opportunities. Adam and Kevin, your achievements will make mine pale in comparison, and that fills me with pride.

Contents

List of Figures

List of Tables

List of Equations

List of Abbreviations

^{0}C	Degrees Centigrade
A	Ampere
AC	Alternating Current
BCS	Baardeen, Cooper and Schrieffer
CFSE	Crystal Field Stabilisation Energy
cfu	Colony Forming Unit
cm	Centimetre
DC	Direct Current
DLS	Dynamic Light Scattering
DNA	Deoxyribonucleic acid
DPG	*N,N*-bis(phosphonomethyl)glycine
EDTA	Ethylenediaminetetraacetic acid
emu	Electromagnetic Unit
FC	Field Cooling
FTIR	Fourier Transform Infrared
g	Gram
GMP	Good Manufacturing Practice
HAI	Hospital Acquired Infection
HRTEM	High Resolution Transmission Electron Microscopy
Hz	Hertz
ILP	Intrinsic Loss Power
IR	Infrared
K	Kelvin
kg	Kilogram
L	Litre
LSW	Liftshitz, Slyozov and Wagner
m	Metre
MACH	Magnetic Alternating Current Hyperthermia
MDT	Magnetic Drug Targeting
mg	Milligram

ml	Millilitre
mmol	Millimole
mol	Mole
MPMS	Magnetic Property Measurement System
MPS	Mononuclear Phagocyte System
MRI	Magnetic Resonance Imaging
MRSA	Methicillin Resistant *Staphylococcus aureus*
M_S	Saturation Magnetisation
nm	Nanometre
NMR	Nuclear Magnetic Resonance
Oe	Oersted
PBS	Phosphate Buffer Solution
PCS	Photon Correlation Spectroscopy
PDI	Polydispersity Index
PEG	Polyethylene glycol
PEO	Polyethylene oxide
rf	Radio Frequency
s	Second
S.aureus	*Staphylococcus aureus*
SAR	Specific Absorption Rate
SHP	Specific Heating Power
SLP	Specific Loss Power
SPION	Superparamagnetic Iron Oxide Nanoparticle
SQUID	Superconducting Quantum Interference Device
T_B	Blocking Temperature
T_C	Curie Temperature
TEM	Transmission Electron Microscopy
T_F	Spin Glass Temperature
T_{fN}	Ferrimagnetic Néel Temperature
TGA	Thermalgravimmetric Analysis
T_M	Morin Transition
TMAOH	Tetramethylammonium hydroxide
T_N	Néel Temperature

T_V	Verwey Transition
UV	Ultraviolet
W	Watt
XRD	X-Ray Diffraction
ZFC	Zero Field Cooling

Chapter 1

Introduction and General Theory

The study of nanoscience and technology is a rapidly expanding subject of interest for all areas of the scientific community with the chance for many new and exciting opportunities.[1] Iron oxide is one material that has evoked a surge in research for its many possible applications, due primarily to its magnetic properties.[2] This thesis shows how altering synthesis conditions can affect the size and thus the magnetic properties of iron oxide nanoparticles. Following this, further stabilisation, using a host of carboxylic acid or phosphonate functionalised ligands, can improve biocompatibility of iron oxide nanoparticles, and can be used in magnetic hyperthermia which has potential applications in microbial disinfection and cancer treatment.

This introductory chapter provides the reader with a background into some of the fundamental theories on which the science is based. It will cover magnetism, especially focussing on hysteresis and relaxation; and relate this to magnetic heating.

The focus compounds for this thesis are nanoparticulate iron oxides as they display specific magnetic properties that are desirable for the application of magnetic hyperthermia. Other potential biomedical applications for these materials are also discussed. The synthetic methodologies that are found in the literature, and the problems and solutions for preparing iron oxide nanoparticles for biomedical applications are also addressed.

1.1. Nanoscience

It is arguably Richard Feynman's famed after dinner lecture in 1959 entitled "There's plenty of room at the bottom" that brought to the consciousness of scientists that there was opportunity and benefits from miniaturisation and building atom by atom.[3] It was not until 1974 that the word nanotechnology was used by Taniguchi.[4] The eighties produced a surge in interest and discoveries in the field which continues today, examples including the discovery of C_{60},[5] development of Atomic Force Microscopy and the infamous IBM logo spelt out in single atoms.[6, 7]

From this the term nanoparticle made its first appearance in the 1980's.[8] Prior to this most of these materials were named small particles or colloids. It is the size range that defines the materials as nanoparticles and at this length scale the particles display unusual and exciting properties that are different from those seen at the atomic scale or in the bulk.

Nanoparticles are particles that are in the size range of 1-1000 nm although more typically 1-100 nm.[9] For a given precursor concentration the smaller the particles formed, the more particles there are and this results in a concomitant larger surface area per unit volume. It is the combination of small size and large surface area that has primarily brought about a surge in research in this field. The increase in surface area results in an increase in unsaturated bonds or free coordination sites. This leads to increased reactivity in these particles. The melting point is also shown to be

reduced. The decrease in size can also affect the electronic properties of the material, including size-dependent quantum effects.

1.2. Magnetism

Magnetic phenomena have been known for many centuries. In fact it was the mineral magnetite, which is the principal magnetic material investigated in this thesis, that was observed by the ancient Greeks to attract iron to itself.[10]

A magnetic dipole is best visualised as being a microscopic bar magnet. The magnetic dipole moment is analogous to the electric dipole moment and is a vector quantity. The magnetic moment direction is from the south to the north of the magnet.

1.2.1. Hysteresis

Hysteresis is an important phenomena exhibited by magnetic materials. This is looked at in the form of hysteresis loops which are a measure of the magnetisation (*M*) or applied field (*B*) against the magnetic field intensity (*H*). *M* and *B* are directly proportional as shown in Equation 1-1 (where μ_o is the permeability of free space, χ_m is the magnetic susceptibility) ; [11]

$$M = \mu_o^{-1}\chi_m B$$

Equation 1-1

If the magnetic field is *in vacuo* then we get *H* as shown in Equation 1-2;

$$B_o = \mu_0 H$$

Equation 1-2

Magnetisation, *M*, has the units Am^{-1} as does *H*. *M* and *B* are intrinsically linked by the Equation 1-3;[12]

$$B = \mu_0 (H + M)$$

Equation 1-3

Hysteresis curves are therefore sometimes referred to as M-H diagrams. If the applied field is ramped up from zero, the magnetic moments of the material become aligned with the field. This reaches a maximum saturation value whereby all the moments are aligned (M_o), therefore M_o can be calculated by the magnitude of the moments of all the atoms per unit volume.[13]

$$M_0 = mn$$

Equation 1-4

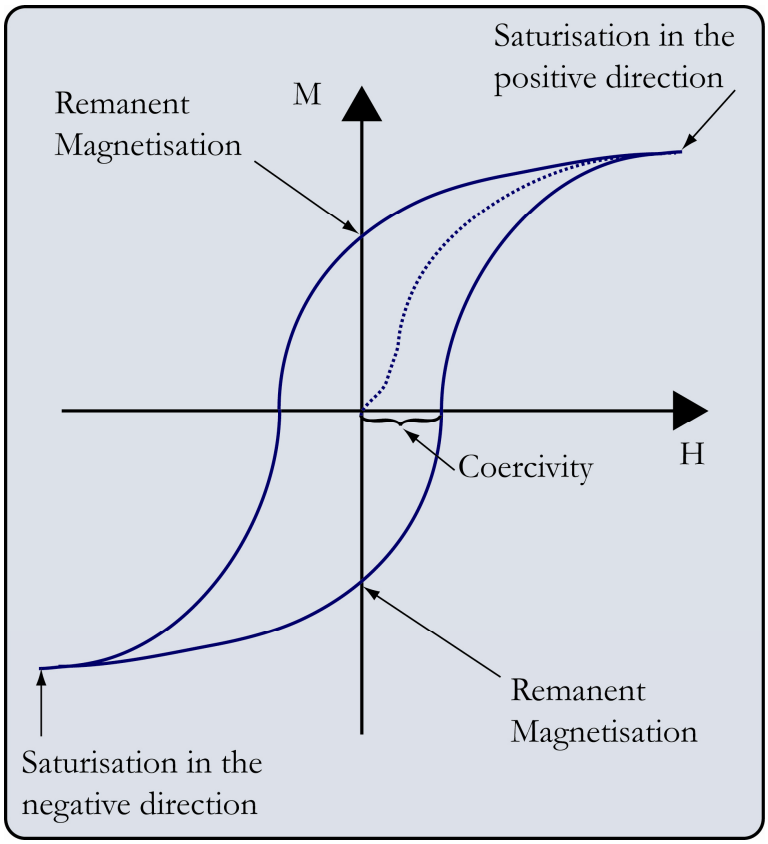

Figure 1-1 An example of a magnetic hysteresis curve/M-H diagram. Coercivity, remanent magnetisation and magnetic saturisation are highlighted.

Once at the maximum saturation value the applied field is reversed but the values of the magnetisation do not match that as before and are instead negative. The value on the y axis at which x = 0 is referred to as the remanent magnetisation. Conversely the value at x where y = 0 is the coercivity and this is essentially the strength of the applied field required to bring the magnetisation of the sample to zero *after* it has been fully saturised in one direction. It is the value of the coercivity that defines whether a material is a hard or soft magnet. Hysteresis means 'to lag' and this is exactly what is seen in a hysteresis loop.[13] There is a time lag for the moment to realign with the field causing a loop to be formed, as opposed to the original path being followed, as shown by the dotted line in Figure 1-1.

The remanent magnetisation and coercivity are also directly dependent on grain size, and multi-domain particles tend to be soft with low coercivities and remanence. This is because only low fields are required to translate the domain walls. However in hard magnets which tend to be single domain particles, you must reverse the magnetisation giving rise to high coercivities and remanence, thus giving a bigger hysteresis loop.[14]

1.2.2. Relaxation

When a magnetic moment is placed into a magnetic field there is a period of time for which it relaxes into its equilibrium or steady state condition. This is termed magnetic relaxation. There are two different types of relaxation, Néel and Brownian.

Néel relaxation is the time taken for a magnetic vector to 'flip' between its energy minima due to thermal fluctuations in a zero field. This can be calculated using the Néel-Arrhenius equation (Equation 1-5):

$$\tau_N = \tau_0 \, e^{(KV/k_BT)}$$

Equation 1-5

Where τ_0 is the attempt time which is around 10^{-9} - 10^{-10} s, K is the anisotropy, V is the particle volume, k_B is the Boltzmann constant and T is temperature.[15]

Following this in the late 1950's and early 1960's W.F. Brown developed Néel's theory to take into account Brownian motion, this was named Brownian relaxation.[16] Essentially instead of flipping directly from one direction to its opposing, as in Néel relaxation, it models the relaxation on the vector essentially fluctuating around the energy minima and then jumping and fluctuating around the other energy minima.[17] Brownian relaxation time τ_B, is defined as (Equation 1-6):

$$\tau_B = \frac{3V_{hyd}\,\eta}{k_BT} = \frac{\pi D^3_{hyd}\,\eta}{2k_BT}$$

Equation 1-6

Where η is the dynamic viscosity of the solvent, V_{hyd} and D_{hyd} are the hydrodynamic particle and volume and diameter. This means that the Brownian relaxation time is determined by the rotational mobility of the particles.[18]

1.2.3. The Classifications of Magnetism

There are many types of magnetism that have been observed. Different classifications are defined in this section. It should be noted that the most commonly seen are diamagnetism, paramagentism, ferromagnetism, antiferromagnetism, ferrimagnetism and superparamagnetism. All materials have a diamagnetic component but can also be assigned to other magnetic classifications.

1.2.3.1. Diamagnetism

As detailed above, diamagnetism is seen in all materials as it arises from paired electrons, and is therefore the most observed. Despite this, commonly only materials that display only this type of phenomena are termed diamagnetic as the

magnitude of the susceptibility is small, and therefore the other types of magnetism dominate.

Diamagnetism, unlike all other types of magnetism, is independent of temperature and the field applied. It can be considered as negative magnetisation, in that the magnetisation and its susceptibility are negative, therefore essentially repulsive. This is analogous to Lenz's Law of 1834 on electromagnetism. Essentially this law states that an induced emf will make a current that opposes the current that induced it.[19]

1.2.3.2. Perfect Diamagnetism

Perfect diamagnetism (or sometimes referred to as Superdiamagnetism) is observed in superconductors and is only seen at low temperatures. When the temperature drops below the transition temperature, the magnetic susceptibility is equal to -1.[13]

The inside of the superconducting (zero electrical resistance) material has an internal field of zero when it is below its critical temperature. The Meissner Effect explains this phenomena whereby perfect diamagnetism occurs below the superconducting critical temperature; the sample surface becomes magnetised to be exactly equal and opposing to the applied field, and it is this excluding force which results in the material having no internal magnetic field.[11]

1.2.3.3. Paramagnetism

Paramagnetism occurs in materials which have unpaired electrons. These electrons are randomly orientated and essentially have their own magnetic moment due to weak coupling being overcome by thermal energy. The magnetic susceptibility of a paramagnetic material is now positive, meaning that they are attracted to magnetic fields, not repelled as in diamagnetism. When there is an external magnetic field some of the spins align with the field, depending on the moment of the material and the external field. Removal of the field enables thermal agitation to dominate which

randomises the spins so no net magnetisation is seen. Thus by cooling a paramagnetic material the spins are easier to align when an external magnetic field is applied. The magnetic susceptibility dependence (often inversely proportional) to the temperature is explained by the Langevin Theory.[20]

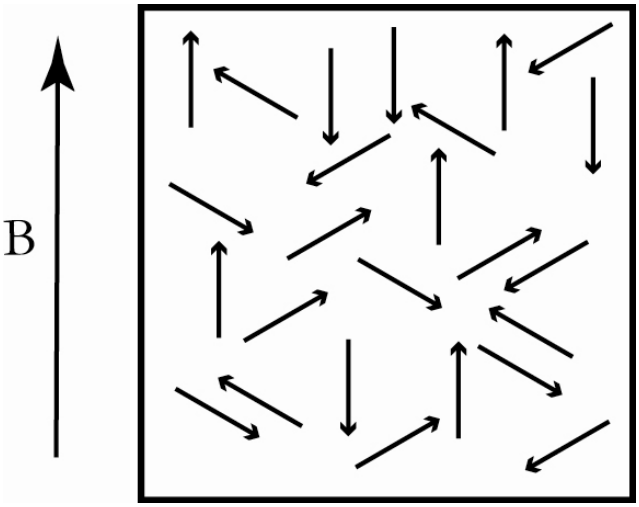

Figure 1-2 A schematic representing the random spin orientations seen in paramagentism. B indicates the direction of the applied field.

1.2.3.4. Pauli Paramagnetism

Pauli Paramagnetism is the name given to the weak, mostly temperature independent type of paramagentism which is found in most metals. Electrons that are present in the Fermi surface are paired, implying the material would be diamagnetic. However, when an external magnetic field is present there becomes an energy gap between the paired electrons in the conduction band. This applied field forces the electrons with spins parallel to the field to lower in energy and the electrons with opposing spins increase in energy. This then means that the energy levels that are spin parallel are preferred and gives rise to a small net magnetisation.[21]

1.2.3.5. Ferromagnetism

The ferromagnet has a long range order, whereby the spins in different environments are aligned in parallel below the Curie temperature (T_c). This alignment is very strong (albeit not strong enough to form a covalent bond), and produces a large net magnetic moment.

Ferromagnetic materials produce hysteresis curves, as described in 1.2.1, as M is not proportional to H. There are two types of ferromagnet; hard and soft. The hysteresis loops of hard ferromagnets are large and wide and M is still large when there is no applied field present, these materials are useful for permanent magnets, an example of a hard ferromagnet is cobalt steel. Soft ferromagnets have much smaller/narrower hysteresis loops and have a small M when there is no applied field. They vary and have a greater dependence on H.[22] An example of a soft ferromagnet is silicon steel.

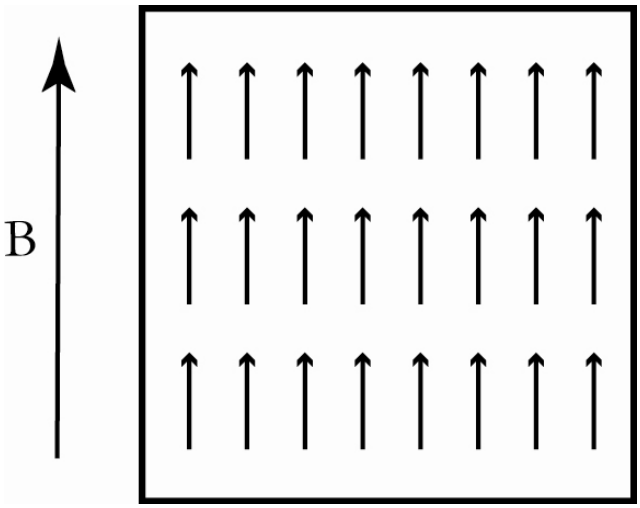

Figure 1-3 A schematic displaying the ordering of spins in a ferromagnetic material. B indicates the direction of the applied field.

However, when T_c is reached and exceeded thermal agitation of the ions becomes favoured over the long range order of the magnetic moments. It is the point where a material loses its 'magnetism' due to the randomised nature of the now unaligned moments and thus becomes paramagnetic.

1.2.3.6. Antiferromagnetism

In an antiferromagnet the spins in the different environments are antiparallel when below the Néel temperature (T_N), they are coupled using a superexchange mechanism (not to be confused with a double exchange mechanism which is seen in the coupling in Fe_3O_4 – see 1.3.7.). These spins are of equal size giving little overall net magnetisation, the magnetic susceptibility being comparable to paramagnets (see Figure 1-4).[23]

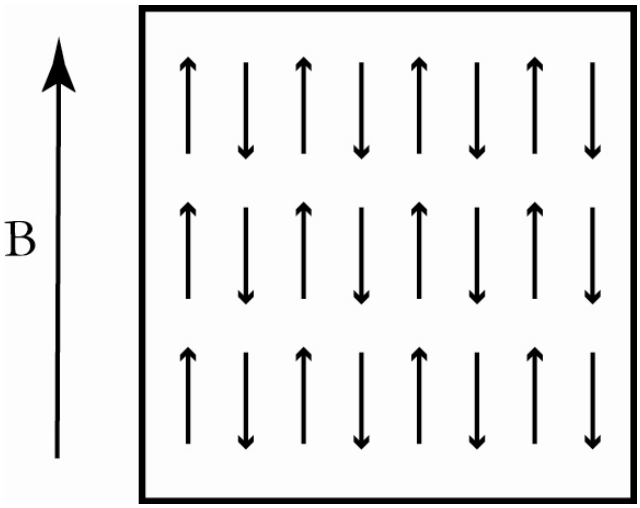

Figure 1-4 A schematic showing the ordering of spins in an antiferromagnet, the overall net magnetisation is zero as opposing spins effectively cancel each other. B indicates the direction of the applied field.

The superexchange sees the covalent bonding of metal ions with a bridging ligand which is 2^- (often oxygen). The two electrons in the ligand p-orbital go to the two neighbouring metal positive ions and give rise to the two metals having spins that are antiparallel.[24] With increasing metal-ligand orbital overlap the superexchange coupling is stronger, but with increasing metal-ligand angles the lessening in overlap makes for a weaker superexchange, and as this reaches 90^0 the superexchange mechanism can also cause ferromagnetic coupling, although this is far less common than for antiferromagnetism.[11]

Like in the case of T_c, when T_N is reached the thermal agitation disorganises the spins and the material becomes paramagnetic.

1.2.3.7. Ferrimagnetism

Ferrimagnetism has similarities to antiferromagnetism, whereby the metal ions in the two different environments are opposing, however the two environments have magnetic moments of different magnitudes. This results in a net magnetic moment being produced (Figure 1-5). Both ferrimagnetism and antiferromagnetism were discovered by Louis Néel.[25]

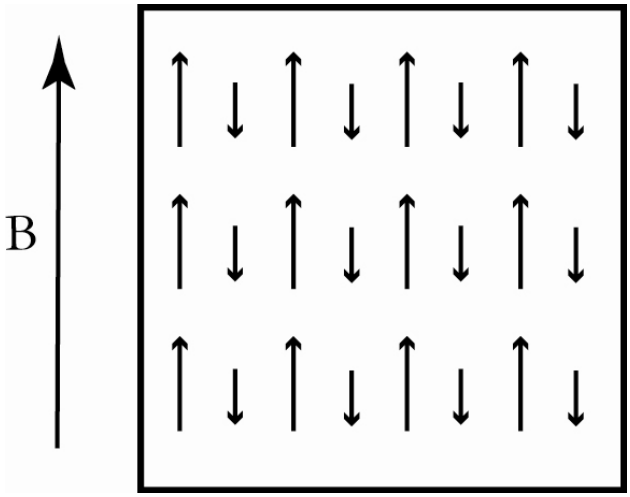

Figure 1-5 A schematic showing the spin alignments in a ferrimagnet, opposing spins are smaller in magnitude thus leaving an overall net magnetisation. B indicates the direction of the applied field.

Again, as seen in both ferro- and antiferro-magnetism once the temperature of a material is increased, the thermal energy overpowers the desire for long range order, the spins are randomised and the material becomes paramagnetic. This temperature is named the ferrimagnetic Néel temperature (T_{fN}). Ferrimagnetism, in the case of magnetite, is explained in more detail in 1.3.7.

1.2.3.8. Superparamagnetism

Superparamagnetism is exhibited in single domain particles thus making it a direct size effect. In a single domain particle there is a size at which it becomes unstable and displays superparamagnetism, conversely at larger particle sizes domain walls become prevalent and the system becomes multi-domain. This is also affected by shape anisotropy whereby equidimensional grains will have a smaller size where it becomes single domain than in anisotropic particles.

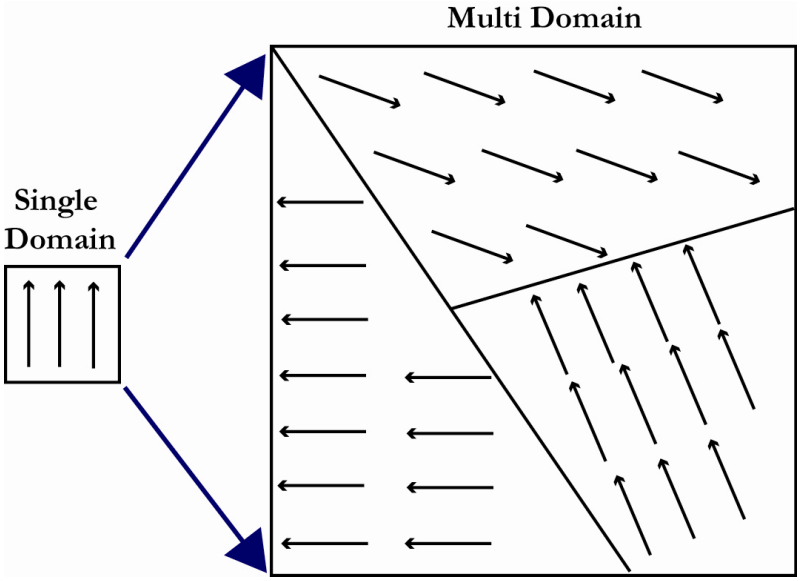

Figure 1-6 The effect of increasing particle size, by going from a small single domain particle to a larger particle results in multi domain materials with domain boundaries.

Superparamagnetic particles have magnetic anisotropy, which means that the electron spins align in a preferred orientation which leads to 'easy' magnetisation in that direction. The cause of this anisotropy can be size, shape or stress. To overcome the anisotropy there needs to be some thermal energy. The temperature at which this occurs is called the blocking temperature, T_B. The way this energy relates to the frequency of flipping is shown in Equation 1-7,

$$f = f_o \, e^{(-E_b/kT)}$$

Equation 1-7

Where f_0 is an attempt frequency, kT is the Boltzmann term. Below T_B the (blocked) particles have coercivity, remanent and saturation magnetisation, similar to that of ferromagnets below the Curie temperature. However above T_B they display very different hysteresis curves with no coercivity (see Figure 1-7).[26]

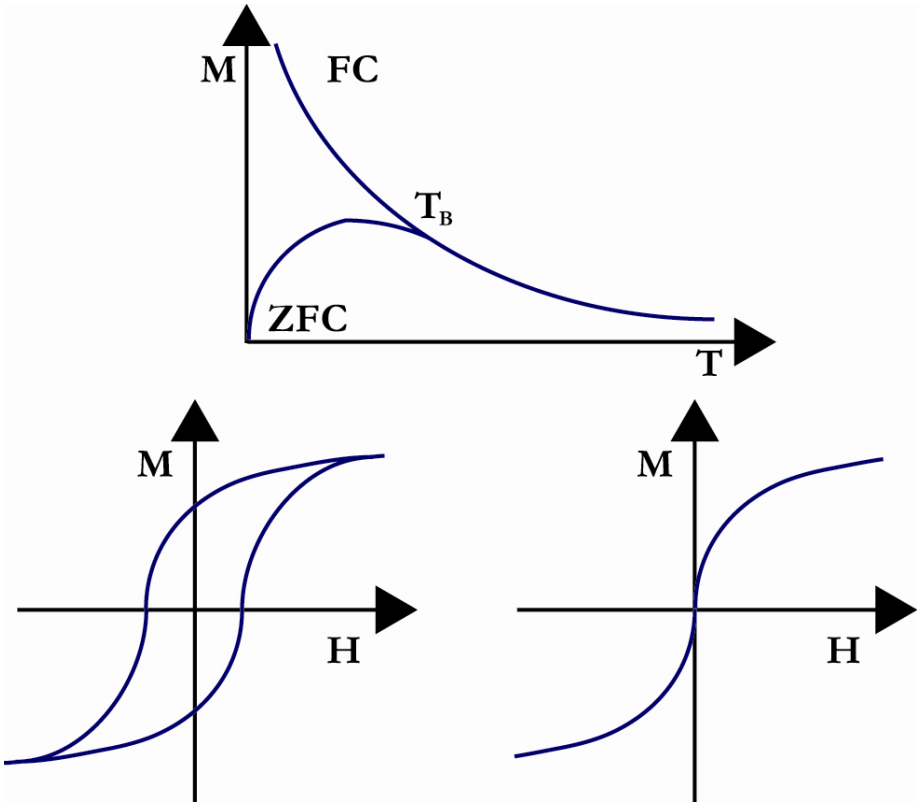

Figure 1-7 Below the blocking temperature (T_B) a superparamagnet has a broad hysteresis curve, similar to what is seen in a ferromagnet. Above the blocking temperature the hysteresis curve goes through the origin and has no coercivity.

Unless an applied field is present the superparamagnetic material will show paramagnetic characteristics, whereby little or no net magnetisation is seen. However when the field is applied the spins align along the line of easy magnetisation to provide a net magnetisation (see Figure 1-8).

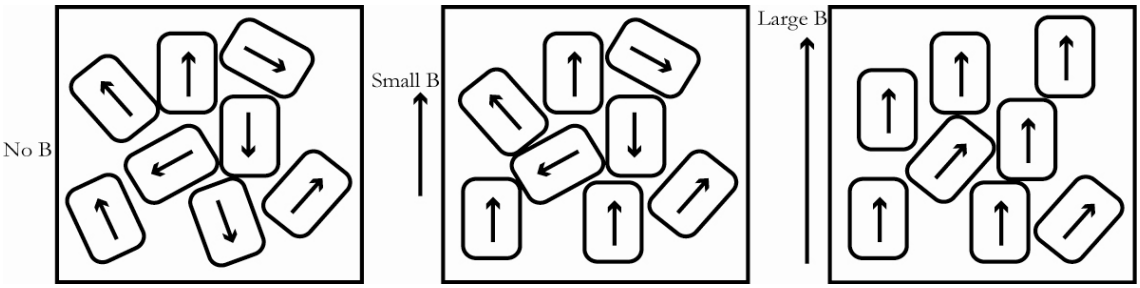

Figure 1-8 With no applied field (B) the spins in a superparamagnet are randomly orientated, as seen in a paramagnet. With increasing B, the spins align with the field.

1.2.3.9. Speromagnetism, Asperomagnetism and Sperimagnetism

Spero-, aspero- and speri-magnetism are only seen in amorphous materials. Sperimagnetism was the first of this kind that was defined by Coey in 1973, the material was initially thought to be antiferromagnetic due to it displaying similar magnetic properties, however the spins were randomly arranged but certain directions had a greater probability due to strain and were fixed with each other by antiferromagnetic coupling between neighbours. In a sperimagnet there are two separate environments that either are singly or both have randomly directed spins. An example of an sperimagnet is $DyCo_3$ where the cobalt ions display some order.[27] These can often take on a structure analogous to a ferrimagnet.[28-30] Speromagnetism sees randomly arranged magnetic moments at low temperature but the material still having no overall moment. A speromagnet is analogous to an antiferromagnet.[27, 30] Asperomagnets also have randomly aligned spins but they follow an anisotropic probability distribution; whereby certain directions are more probable. The net magnetic moment is a small amount of the collinear saturation value. An asperomagnet is analogous to a ferromagnet. [30-32]

1.2.3.10. Helimagnetism

Helimagnetism is only observed at very low temperatures. The magnetic moment spins on corresponding neighbours are angled around the axis at an angle of Φ.

These moments over a range then create a helical arrangement as seen in Figure 1-9. However, if $\Phi = 0^0$ or 180^0 then the structure is ferromagnetic or antiferromagnetic respectively.[33]

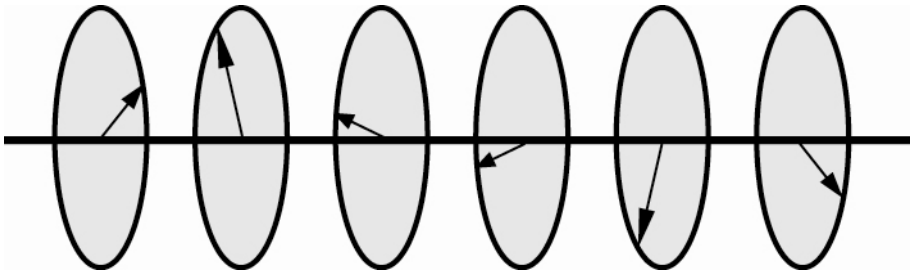

Figure 1-9 In a helimagnet, seen at low temperatures, the spins are able to align in a helical arrangement.

1.2.3.11. Spin Glass

Spin glasses below the transition temperature T_F are frozen magnetically frustrated materials which have long range disorder. Due to this there is more than one ground state which the spin glass can exist at. Like in the other cases, above T_F the thermal energy overrides the magnetic intercommunication.[34]

1.3. Iron Oxide

The iron ions present in iron oxides are known to give rise to many of the magnetic properties, as described above. This section looks at iron and the iron oxides and explains the structures that give rise to the magnetism.

1.3.1. Iron

Iron is a highly abundant element on Earth, existing rarely in its elemental state due to it being readily oxidised into forms such as oxides, chlorides and sulphates. It has a great many uses and humans have made use of these throughout history. It is commonly alloyed with other metals to increase its strength, such as in steel.

Importantly, iron is also an essential element for life as it is both an electron donor and receptor. It is an essential component of haemoglobin and myoglobin.[35] Most of this iron is bound in cells to proteins. Unbound iron can be toxic upon reaction with hydrogen peroxide, this reaction is named the Fenton Reaction or the Haber-Weiss reaction. This produces hydroxyl free radicals as shown in equations 1-8 and 1-9. [36]

$$Fe^{2+} + H_2O_2 \rightarrow Fe^{3+} + \cdot OH + OH^-$$

Equation 1-8

$$Fe^{3+} + H_2O_2 \rightarrow Fe^{2+} + \cdot OOH + H^+$$

Equation 1-9

Iron is a first row transition metal and has the electron configuration of $[Ar]4s^23d^6$. It can take the oxidation states of -2 up to +6, however the most commonly seen are 0, +2 and +3.

Iron occurs in many different forms, for example with carbonyls, halides, sulphides, hydroxides and cyanides. In this thesis we are concerned only with the iron oxides. The iron can be in its +2 or +3 oxidation state or as a combination of the two. The iron d-electrons, in its +2 state, experience an octahedral field and are high spin, with one pair of electrons in a low energy orbital, and the others occupying the other four orbitals. This is because the crystal field stabilisation energy (CFSE) for Fe(II) is greater for a tetrahedral arrangement, thus octahedral is favoured. Alternatively, in the +3 oxidation state there is no CFSE and either a tetrahedral or octahedral environment can be taken and the electrons are again high spin, resulting in five unpaired electrons; one in each orbital (see Figure 1-10).[37] The structures and properties of the known iron oxides are outlined below.

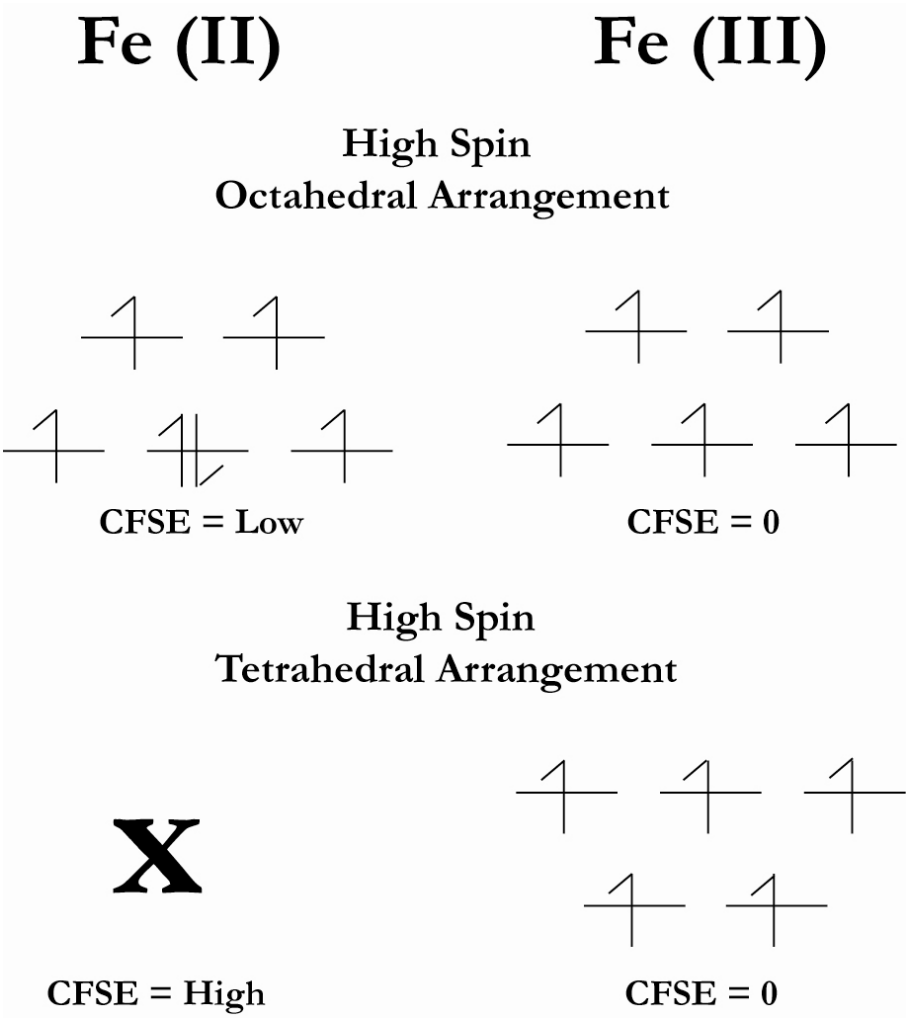

Figure 1-10 Crystal field splitting diagrams for Iron (II) and Iron (III) in iron oxide. In all cases the arrangements are high spin. However, due to the crystal field splitting energy (CFSE) Fe(III) is able to have both an octahedral and tetrahedral arrangement, whereas Fe(II) can only be octahedral.

1.3.2. FeO

FeO sees iron in its +2 state, in fact it is the only binary oxide form which contains only Fe(II). The common name is wüstite, named after its discoverer, the German metallurgist Fritz Wüst. It has a cubic structure, the common rock salt structure, with a cell dimension of between 0.4302-0.4275 nm and has the space group *Fm3m*.[37, 38] Wüstite is actually seen with a defect whereby the true stoichiometry is $Fe_{1-x}O$ ($0.05<x<0.15$), where the Fe(II) is oxidised to Fe(III), and also there are

defects whereby these Fe(III) ions also occupy interstitial tetrahedral positiions.[39] FeO displays antiferromagnetism at room temperature and T_N = 203-211 K.

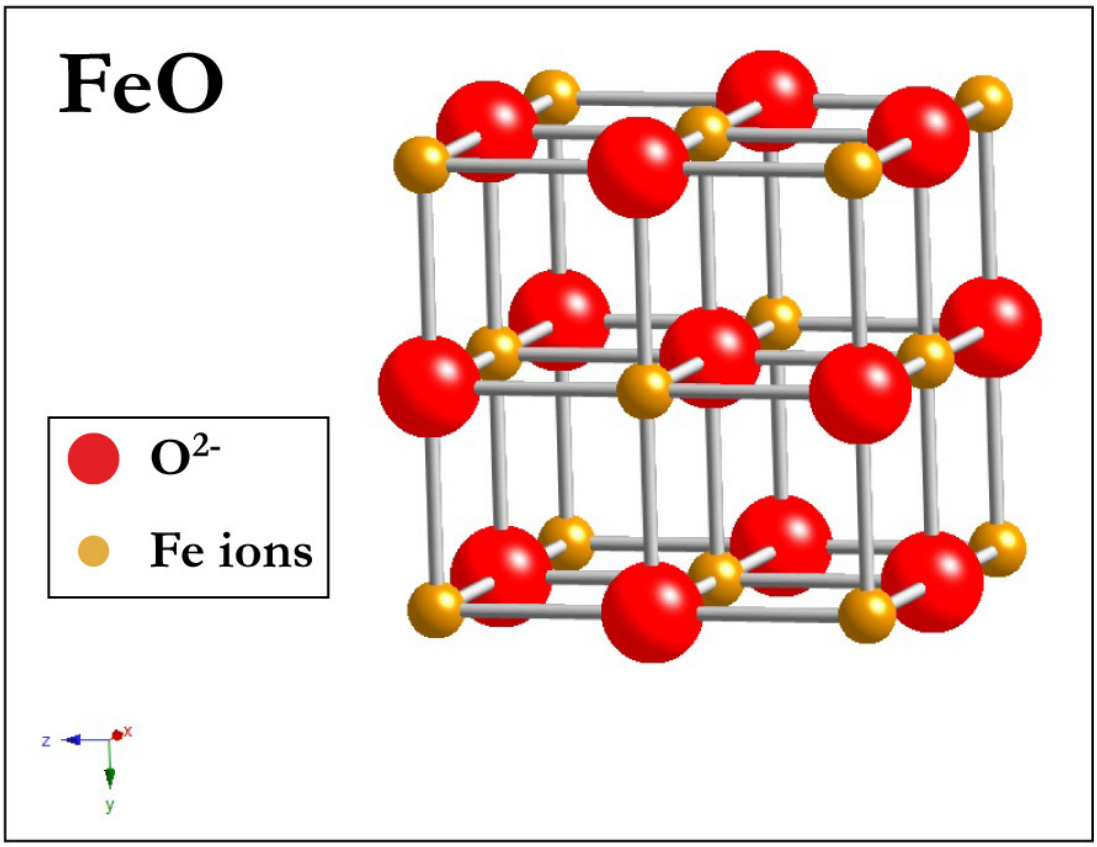

Figure 1-11 The crystal structure of FeO (wüstite).

1.3.3. α-Fe_2O_3

Hematite is the common name for α-Fe_2O_3 and the iron is +3. It is due to its blood red colour that it got its name; the Greek word for blood being haima. It assumes a hexagonal (rhombohedral) structure (see Figure 1-12). Hematite has the unit cell dimensions of a=0.5034 nm and c=1.3752 nm and the space group is *R3c*.[37]

At room temperature, hematite is weakly ferromagnetic and below the Morin transition (T_M) it is antiferromagnetic. T_M is 260 K and the T_C is 956 K. Below the Morin transition the Fe(III) spins are aligned along the c-axis (the trigonal plane) in both directions and therefore antiferromagnetic. Upon reaching and exceeding the

Morin transition spin flopping occurs resulting in the alignment moving 90^0 and canting results in the spins no longer being perfectly opposite and thus weak ferromagnetism is seen.[40]

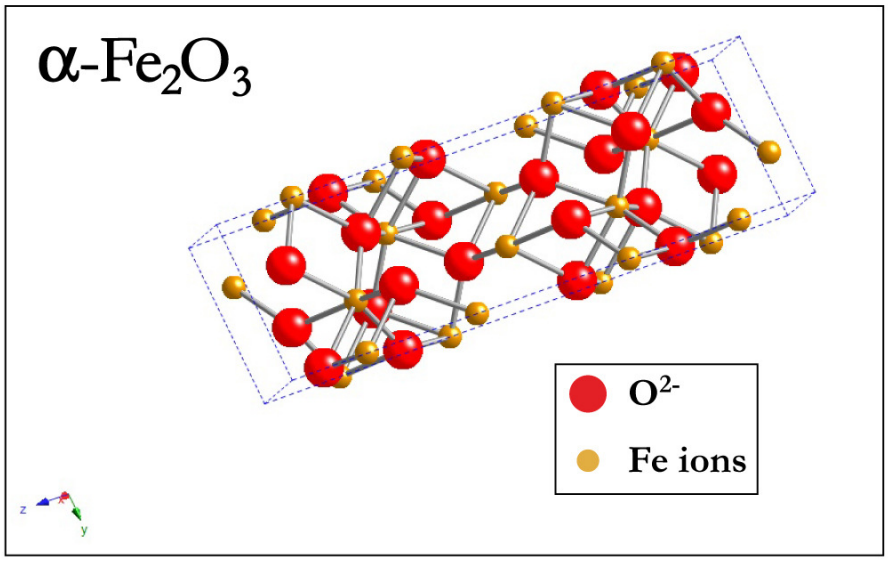

Figure 1-12 The crystal structure of α-Fe_2O_3 (hematite).

1.3.4. β-Fe_2O_3

β-Fe_2O_3 is body centred cubic, where a=0.9398 nm. The space group is *Ia3*. T_N is 110-119 K and above 770 K it changes into hematite.[41]

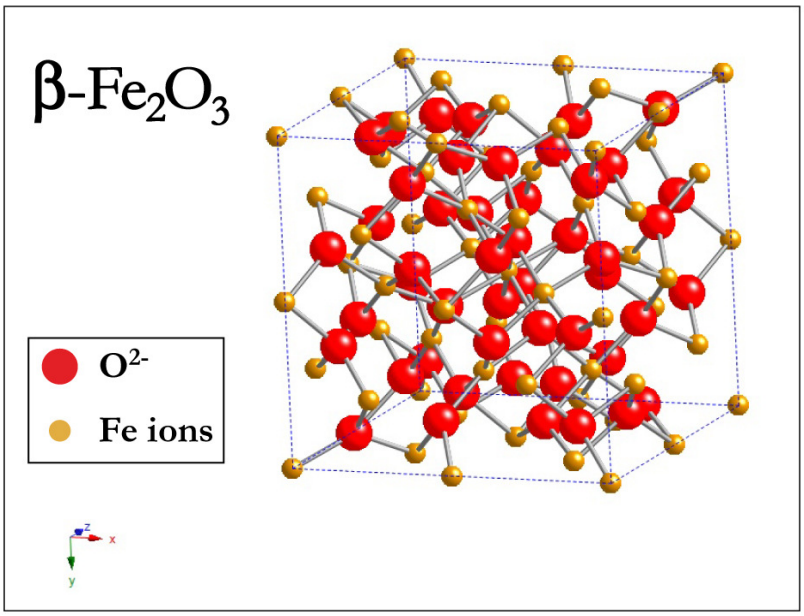

Figure 1-13 The crystal structure of β-Fe_2O_3.

1.3.5. γ-Fe_2O_3

Maghemite (γ-Fe_2O_3) is the oxidised derivative of magnetite and has a defect inverse spinel structure due to the cation vacancy; the Fe^{2+} in magnetite is replaced with ⅔ Fe^{3+} and ⅓ vacancy. The Fe (III) ions occupy both the octahedral and tetrahedral sites and due to them being in two different environments it is also ferrimagnetic. The Curie temperature for this material is not known although it is believed to be between 820 and 986 K, at 400°C it becomes hematite.[42]

Maghemite can either have a cubic structure (see Figure 1-14) with the lattice parameter *a* being smaller than that of magnetite or it can have a stretched tetragonal structure. The cubic structure space group is $P4_332$ and the unit cell dimension a=0.83474 nm. The tetragonal structure has the space group $P4_12_12$ and its unit cell dimensions are a=0.8347 nm and c=2.501 nm.[37]

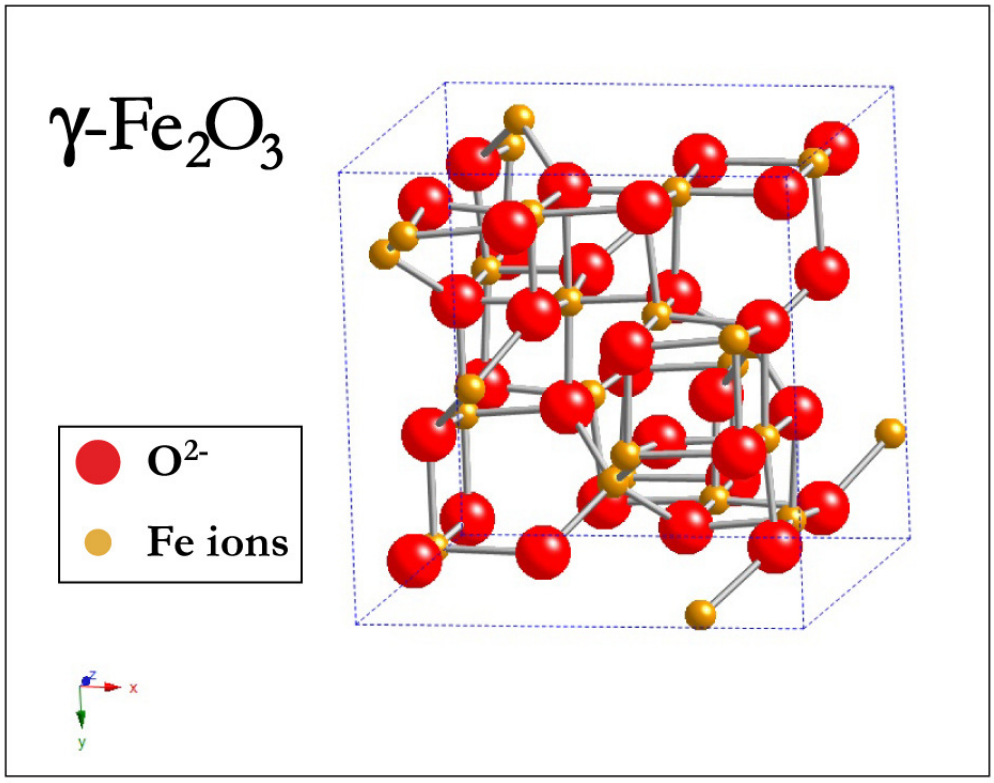

Figure 1-14 The cubic structure of γ-Fe_2O_3 (maghemite).

1.3.6. ε-Fe_2O_3

ε-Fe_2O_3 has an orthorhombic structure with the space group *Pna2₁* and unit cell dimensions of a=0.5095 nm b=0.879 nm and c=0.9437 nm (see Figure 1-15). ε-Fe_2O_3 has not been synthesised on its own, instead it is in a mixture with other iron oxide phases.[37] ε-Fe_2O_3 is antiferromagnetic and T_N is 1026 K.

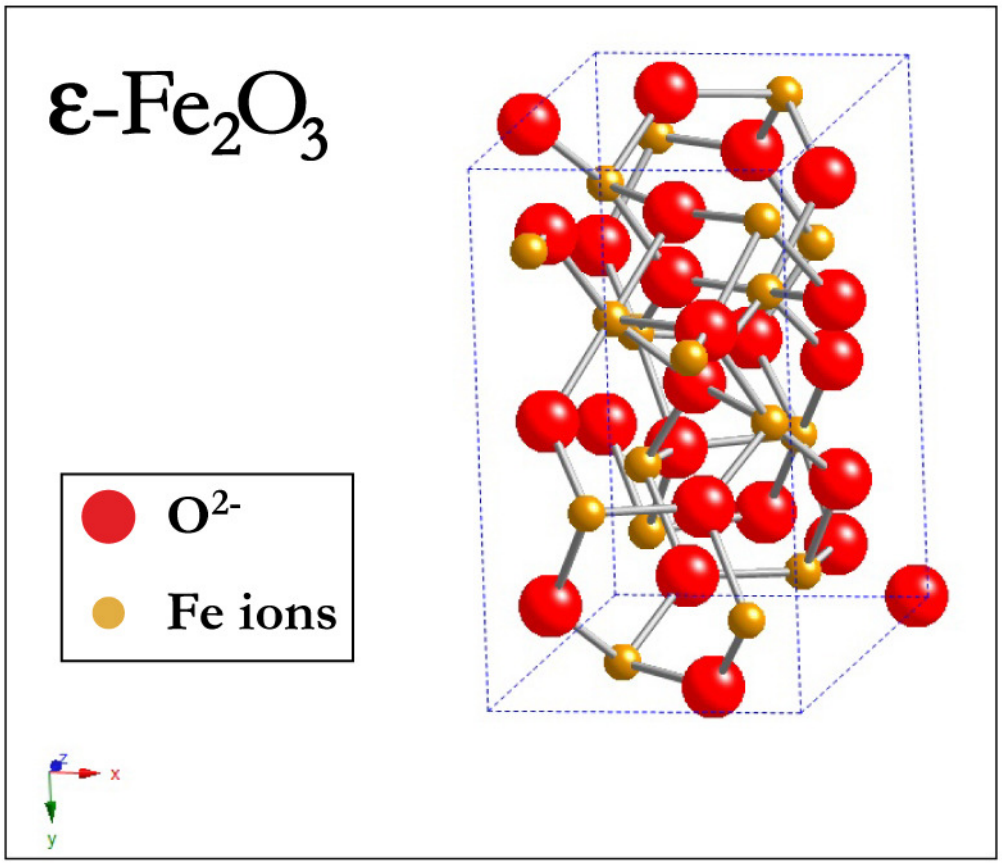

Figure 1-15 The crystal structure of ε-Fe_2O_3.

1.3.7. Fe_3O_4

Fe_3O_4 has the mineral name of magnetite, it was the first magnetic material discovered. The name of the mineral is relatively new, however it comes from the word magnet which got its name from the area in Turkey named Magnesia where magnetite and thus the magnet phenomena was first seen.[11]

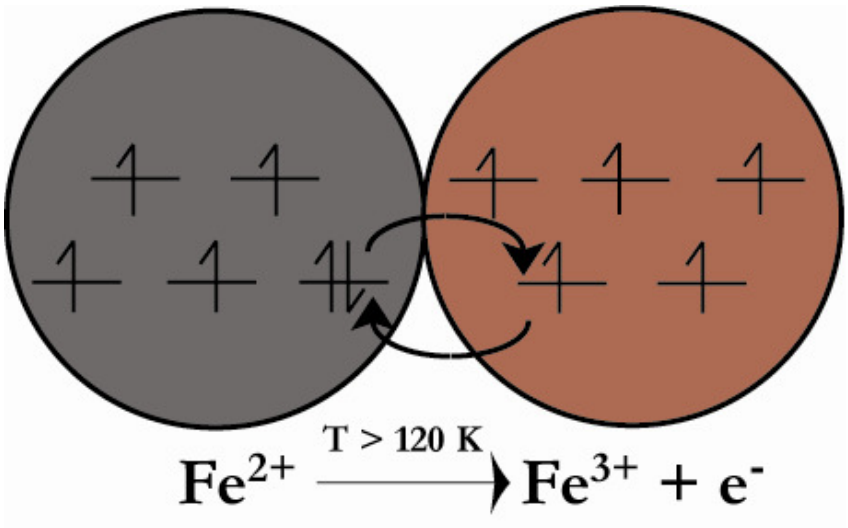

Figure 1-16 A diagram displaying that above the Verwey transition (120 K) double exchange occurs, whereby the electron in Fe^{2+} is able to hop onto the Fe^{3+} and back again.

The crystal structure of Fe_3O_4 is that of a cubic inverse spinel type above the Verwey transition temperature (T_v) of approximately 120 K, where there is a change in conductivity resulting in magnetite going from an insulator to a metal.[43] This Verwey transition has led to much disagreement about the exact mechanism effecting this change. It is believed that at 120 K a double exchange process begins from the increase in thermal energy, whereby electrons on neighbouring Fe^{2+} and Fe^{3+} that occupy the octahedral holes in the lattice are able to hop between each other as they are ferromagnetically coupled.[44] The fundamental difference between double exchange and superexchange is that the electrons do physically move between the metal ions in double exchange. This causes the distribution of the two ions to become random, and is the reason why magnetite is extremely conductive. Unfortunately this does not conclusively explain the whole picture and now there is much work being done on looking at some theories proposed by Mott and Ihle-Lorenz. Mott's theory works best for low temperature data and the Ihle-Lorenz model works better for higher temperature data, briefly the two theories are:[45]

- **Mott's Model –** The Verwey transition is analogous to the phase change of a Wigner Glass to a Wigner Crystal, whereby there is tunnelling and range hopping of small polarons.

- **Ihle-Lorenz's Model –** Superposition of polaron band and hopping conductivity.

Another area of contention is the space group of magnetite. It is commonly interpreted as being the centrosymmetric *Fd*3*m* as originally proposed by Bragg but Grimes, and others since, have argued it is the non-centrosymmetric $F\bar{4}\,3m$.[46, 47]

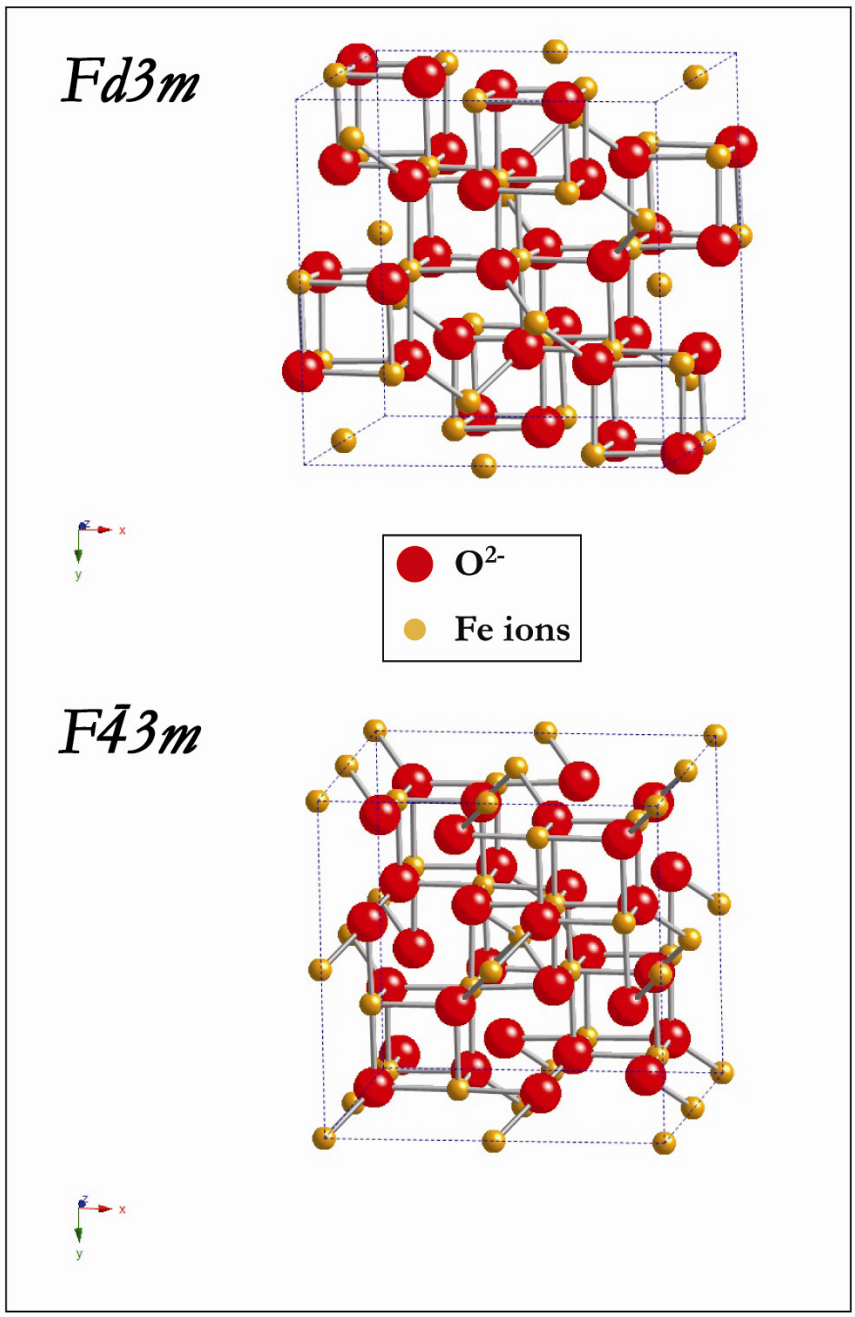

Figure 1-17 The crystal structures and space groups of Fe_3O_4 (magnetite).

In the unit cell of magnetite, there are thirty-two oxygen atoms which are cubically face centred, and the iron atoms occupy sixteen octahedral sites and eight tetrahedral sites, whereby the iron (II) sits at half of the octahedral sites and the iron (III) is on the other half and all the tetrahedral positions. This is why it is an inverse spinel as normal spinels have all the trivalent cations in the octahedral sites and the divalent are in the tetrahedral sites (e.g. $MgAl_2O_4$).[22]

Historically, magnetite was believed to be ferromagnetic. It was not until 1948 when Néel published his seminal paper *'Proprieties Magnetiques Des Ferrites – Ferrimagnetisme et Antiferromagnetisme'* that it was correctly determined as ferrimagnetic at room temperature.[25] The iron (III) atoms exist in two different environments; octahedral (sublattice B) and tetrahedral (sublattice A). Their spins are opposing and different in magnitude, leaving an overall magnetism of the material (see Figure 1-18).

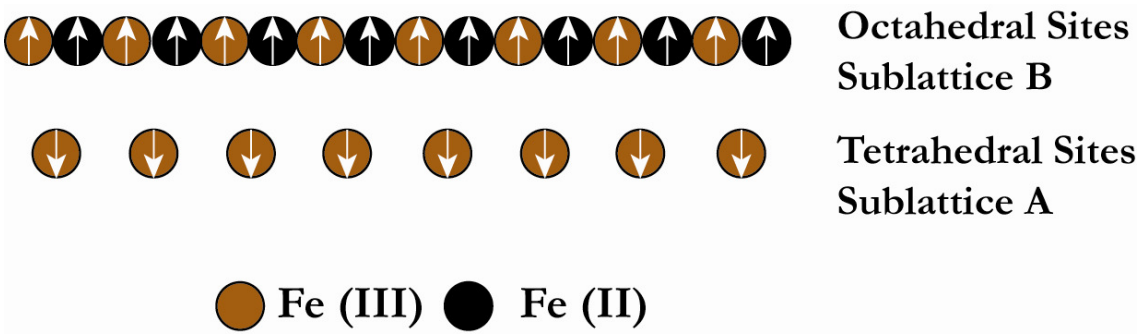

Figure 1-18 Fe(III) atoms in octahedral and tetrahedral environments are opposing and effectively negate each other, leaving an overall magnetisation occurring from the Fe(II).

At 850 K thermal agitation of the ions become favoured over the long range order of the magnetic moments. The material becomes paramagnetic due to the randomised nature of the spins (T_{fN}).

1.3.8. Synthesis of Nanosized Magnetite and Maghemite

The formation of the two desired iron oxide forms; magnetite or maghemite, may be done in similar ways. A key aspect is to use iron in the correct oxidation states and at the correct ratio. However, it is also important to note the effect oxidation will have on the particles. Magnetite is not thermodynamically stable under atmospheric oxygen pressure; this is most prevalent in the case of small particles which oxidise far quicker than large aggregates of magnetite which degrade over geological time.[48] Therefore to form Fe_3O_4 over γ-Fe_2O_3 an inert atmosphere must be created for the reaction and to increase the shelf life it should also be stored in an oxygen deficient environment. The iron oxides can be synthesised from both a top down (e.g. Ball milling)[49] or a bottom up approach to make them nanosized (1-100 nm). Here we look in depth at the bottom up synthetic methods.

Interestingly, magnetite is synthesised by some birds and fish to assist in navigation. An example of such is the homing pigeon which has these in the free nerve endings of its beak essentially acting as a compass.[50] Magnetotactic bacteria are also being investigated as mass cultivation could be used in the production of stable magnetite nanocrystals. They use the magnetic nanoparticles to align themselves with the Earths magnetic field, hence the term magnetotactic, and were first discovered by Richard Blakemore in 1975.[51] The bacteria contain magnetosomes which are narrowly size distributed inorganic nanoparticles (iron oxides or iron sulphides) which are stabilised by a biocompatible organic membrane (a protein and lipid bilayer).[52] By harvesting the magnetosomes from the magnetotactic bacteria, these surfaces can then be functionalised for more specific requirements.

1.3.8.1. Solution Based Synthesis of Iron Oxide Nanoparticles

A key synthesis for iron oxide nanoparticles is a solution based method, particularly that of co-precipitation. This involves the mixing of solutions of iron(III) and iron(II) in a 2:1 ratio and upon addition of a basic surfactant such as ammonium hydroxide, iron oxide nanoparticles precipitate forming a colloidal suspension. This method has been used for some time and developed since the early 20th century.[53] In this type of synthesis there are some key stages, namely saturation, nucleation and growth. Saturation is an important part of the process. For the particles to precipitate out they must reach the critical point at which the solution is at saturation. As the reactants precipitate out of the solution as small clusters, these clusters then go on to act as seeds for which further particle growth may occur. In ambient conditions monodispersity can be achieved. This type of model was first proposed by LaMer and Dinegar and the reaction scheme model is shown in Figure 1-19.[54]

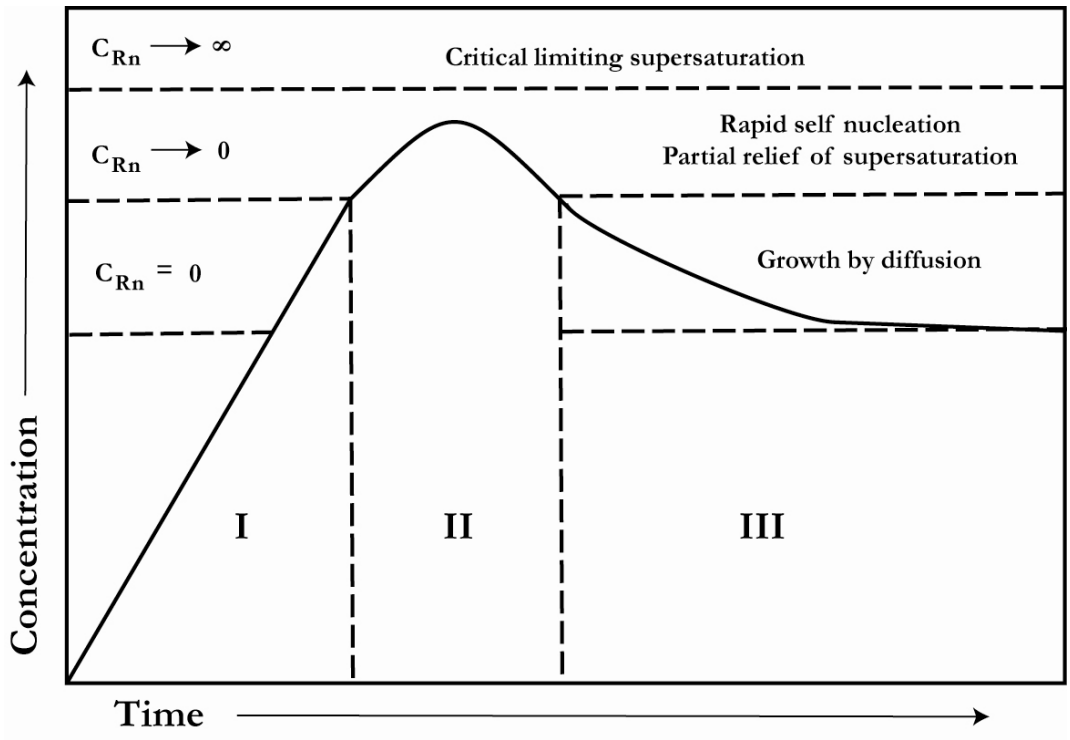

Figure 1-19 A replication of the LaMer and Dinegar diagram for how monodisperse particles are formed. I is the prenucleation, II is nucleation and III is the growth stage.[54]

Ostwald ripening, named after Wilhelm Ostwald who first discussed this effect, is key to understanding the growth process of the nanoparticles.[55] When crystallites form in solution a growth period occurs, during this time the larger particles begin to pull material from the smaller ones thus increasing the size of the already larger particles. The reason for this is a thermodynamic one; to decrease the surface energy. It is more favourable to have atoms in the bulk than on the surface. [55, 56]

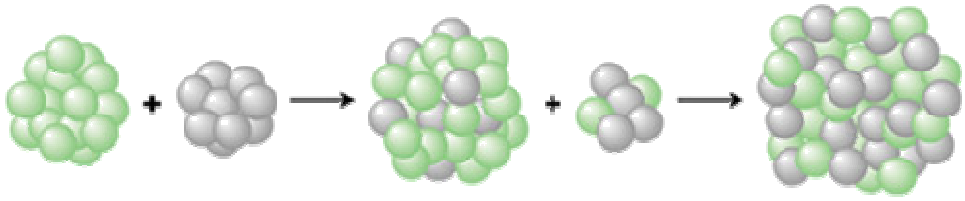

Figure 1-20 Ostwald Ripening: to decrease the surface energy growth occurs by larger particles pulling materials from smaller ones:[57]

However as is commonly known by many researchers in this field the formation of monodisperse nanoparticles is a rather difficult task, and achieving repeatable results is difficult to achieve. This could be because there are so many different paths the formation can take thus making it highly chaotic and difficult to control.

1.3.8.2. Hydrothermal Synthesis

Hydrothermal synthesis has been shown to produce iron oxide nanoparticles that have a narrow size distribution. The synthesis harnesses the dehydration and hydrolysing power of supercritical water to make metal oxides from their salts.[58] This also is a relatively "green method" that does not require the use of organic solvents. By altering the reaction conditions, for example precursor concentration and solvent ratios, there is an opportunity to tune and select the average size of the nanoparticles.[59] The hydrothermal synthesis has also been developed by researchers using continuous flow techniques, thus allowing for large batches to be produced with relative ease, mostly strong bases are required in the synthesis but Adschiri et

al. showed that they were able to make 50 nm magnetite nanoparticles using ferric ammonium citrate. [60]

1.3.8.3. Pyrolysis Synthesis

Pyrolysis is a common synthetic method for the formation of iron oxide nanoparticles. By using high temperatures it is possible to decompose the precursors into the desired product. The potential for it to be scaled up very easily for mass production is also an important aspect, and there can also be a constant through-put for continual production.[61] The two types of pyrolysis used are that of spray, also known as aerosol decomposition, and laser.[62]

In spray pyrolysis the precursor can be delivered as either an aerosol carried *via* the gas[63, 64] or using an atomiser.[65, 66] The stoichiometry of the precursor solution is also the stoichiometry of the final product which is very useful for formation of particles from multiple precursors.[67] Recently Wang et al have made a comprehensive study of parameters to control final particle size in ultrasonic spray pyrolysis. Their results concluded that the final particle size increased with gas flow rate and spray volume. Conversely by the addition of alcohol or increasing the precursor temperature and/or concentration the particle size decreased.[68]

In laser pyrolysis, with the assistance of a continuous wave carbon dioxide laser, it is possible to increase the uniformity of the particles by way of varying the laser intensity, the pressure in the reactor, oxidation condition and the precursor temperature.[69, 70] The particles are also free of impurities.[71]

1.3.8.4. Reverse Micelle Synthesis

A micelle uses molecules that have a hydrophilic headgroup and a hydrophobic tail to form self-assembled aggregates, an example, and commonly used in micelle and reverse micelle formation is the phospholipid. In a water based solution the

phospholipid tails point towards the centre of the micelle, with the hydrophilic headgroups on the surface, these are oil-in-water micelles. A reverse micelle is a water-in-oil micelle. The solution is non polar, this causes a reverse of the micelle, whereby the hydrophobic tails are on the surface and the hydrophilic headgroups on the inside (see Figure 1-21). [72]

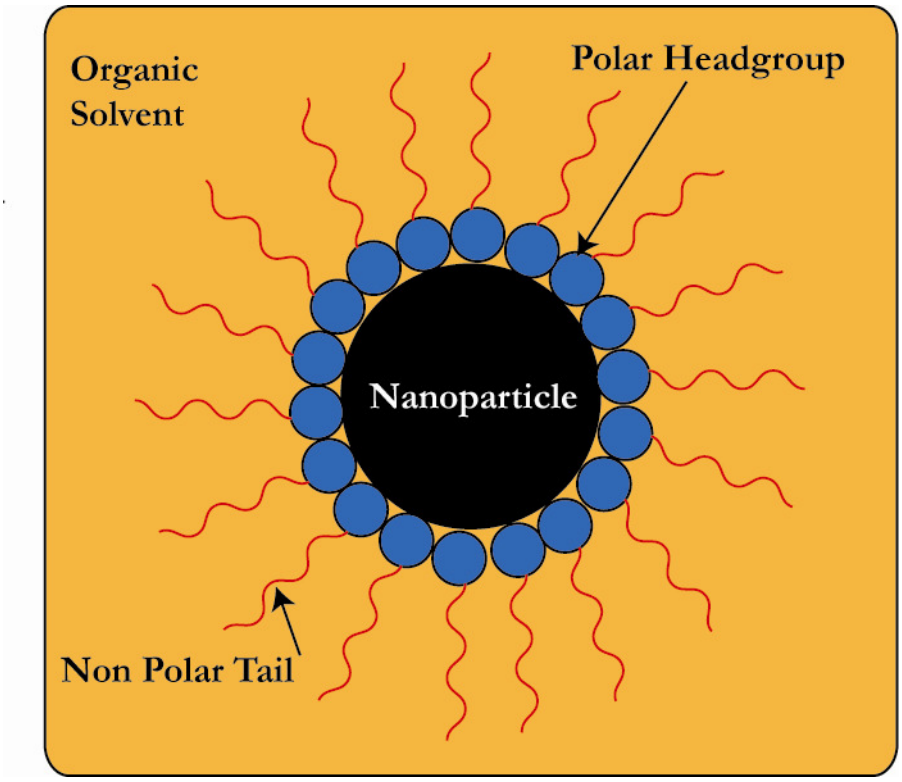

Figure 1-21 A reverse micelle (water in oil micelle) that encapsulates a nanoparticle within the aqueous core, this is protected by the hydrophilic (polar) headgroups and the hydrophobic (non polar) tails point out into the organic solvent.

This has led to development of the growth of nanoparticles inside the core of the reverse micelle. A solution containing dissolved iron salts added into a non polar solution containing the phospholipids, causes the phospholipids to collapse around the iron salts thus encapsulating them. By then adding a reducing agent such as sodium hydroxide it is possible to grow the nanoparticle from the iron salts. The benefit of this method is that there is increased size control and uniformity.[73] Researchers have then shown success in coating these particles with elemental gold to give increased stability in water.[74] However it is problematic to purify the samples

and also to phase transfer the magnetic nanoparticles from the non-polar solvent into a polar solvent such as water.

1.3.8.5. Matrix Synthesis

Another primary method in the synthesis of iron oxide nanoparticles is that of formation and growth within a matrix. This method allows increased control of the shape and size of the product potentially increasing monodispersity. Another positive of this approach is the avoidance of synthesis of 'non-magnetic' iron oxides which often happens in solution based methods. However there are then issues in getting the particles out of the matrix and into a dispersion in solution. This tends towards a multi-step method to coat the particles for stabilisation, or complex *in situ* methods are developed. The matrices used for the particles are often glassy and use traditional solid-state synthesis methods such as 'shake and bake' whereby the products are ground in a pestle and mortar to create a fine and even distribution. This is then placed into a crucible and placed in an oven at high temperatures for many days. The glassy matrix is then dissolved away leaving the desired product. Müller et al have shown promising results using a borate glass method.[75]

1.3.9. Properties of Nanosized Magnetite and Maghemite

Nanosized materials have reduced dimensionality and show more extensive magnetic properties. This is because in the bulk, outershell electrons are more likely to be paired in bonding, but when the size is reduced narrower bandwidths are observed resulting in larger density of states at the Fermi energy. This means magnetic behaviour is more likely to be seen, as explained in the Stoner criterion. [10]

Superparamagnetism is a property seen in nanosized materials. Dunlop studied single domain/superparamagnetic/multi-domain boundaries, particularly that of

magnetite and he used a combination of experimental and theoretical methods to calculate the particle size range for superparamagnetism to occur, this being 29-36 nm at room temperature.[76] The size in which single domain begins is denoted d_0 and the diameter at which superparamagnetism occurs d_s. d_o is found to be around 57 nm ± 5 nm in magnetite.[77] The preferred crystallographic orientation which gives easy magnetisation in magnetite is the [111].[37]

1.4. Biomedical Applications

The use of iron oxide in medicine is not new. Magnetite, although then known as Lodestone, was recorded by Hippocrates to be prescribed to control bleeding and haemorrhage and treat arthritis and gout as early as 460 BC. In the 10th Century AD Avicenna used the powder of iron oxide for an antidote to the swallowing of poisonous rust.[78] Iron oxide nanoparticles have use in both *in vivo* (inside the body) and *in vitro* (outside the body) applications, and these are discussed in more detail in the following sections.

Due to the special properties possessed by nanosized iron oxide and their potential for biocompatibility there is a growth in research in the biomedical applications of this material. For this to be successful the iron oxide nanoparticles require surface modification for stabilisation in the body and/or for functionalisation to make intelligent particles.

1.4.1. Coatings and Stabilisation

The Brownian motion of nanoparticles in a ferrofluid mean that they collide with each other and sometimes upon collision these will aggregate causing them to lose their stability in the colloidal suspension and hence precipitate out of the solution. The two forces involved in the aggregation are Van der Waals and magnetic dipole-dipole interactions.[79] There are two key ways that this aggregation may be reduced or completely stopped and these are:

- **Electrostatic Stabilisation:** Creation of an electrical double layer around the particles.
- **Steric Stabilisation:** Grafting of polymers to the particle surface.

It is also known that the solubility (hydration energy vs. lattice energy) of Fe (III) is extremely small and Fe (II) is not much greater, this means that the solubility of the ions at mid-pH (6-8) is difficult.[37]

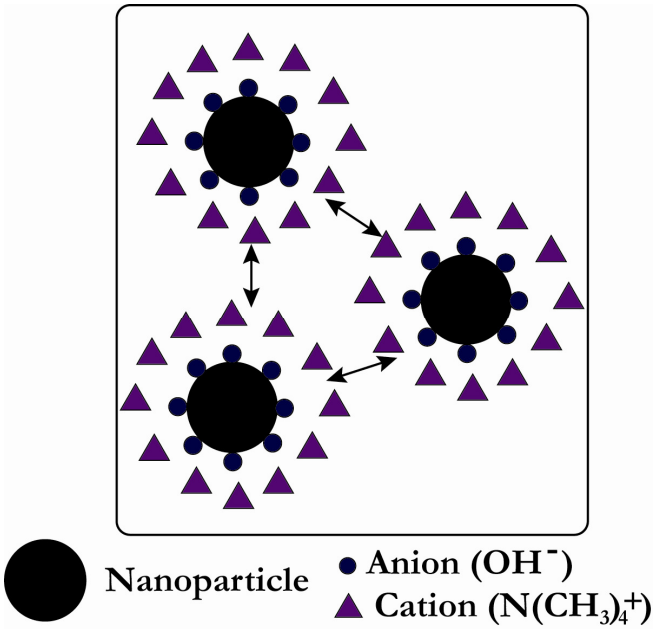

Figure 1-22 The iron oxide nanoparticle is charged stabilised in solution, whereby the hydroxyl anion is on the surface and is then counterbalanced by the $N(CH_3)_4^+$ cation. The cationic atmosphere then aids repulsion between the particles to prevent Ostwald ripening and agglomeration.

To prevent the agglomeration of the iron oxide formed by the co-precipitation method tetramethylammonium hydroxide (TMAOH) is often added. It is thought that the hydroxide anion is attached to the surface of the nanoparticle and the $[N(CH_3)_4]^+$ cation remains associated to the particle for charge balance (see Figure 1-22). This cationic atmosphere ensures repulsion between other particulate environments.[80] The problem with this is that it creates a pH which is not desirable for biological applications. At pH 7 this ionic atmosphere is decreased and causes

the particles to coagulate making them no longer nanoparticulate. This is an important area of research and much work is now involved in looking at coatings to stabilise the iron oxides at neutral pH.[73]

The coatings used to stabilise the particles for use in biomedical applications must also be useful for increasing the circulation lifetime inside the body. This is done by increasing resistance to opsonisation, which is the adhesion of plasma proteins and glycoproteins. Opsonized particles are then easily identified by Kupffer cells in the liver which then remove them from the body. The proteins bind quicker and easier to hydrophobic particles. [81]

Many coatings have been made using organic molecules such as carboxylates, siloxanes, sulphates, phosphonates and phosphates.[82, 83] The aim is to find a coating that is hydrophilic to encourage a stable colloidal suspension in a biocompatible medium such as water or phosphate buffer solution (PBS). In the case of carboxylic acids it is believed that the acid reacts with the iron around the surface of the nanoparticle and is chemisorbed onto the surface. A variety of carboxylic acid coatings have been produced including oleic acid, folic acid and lauric acid.[84-86]

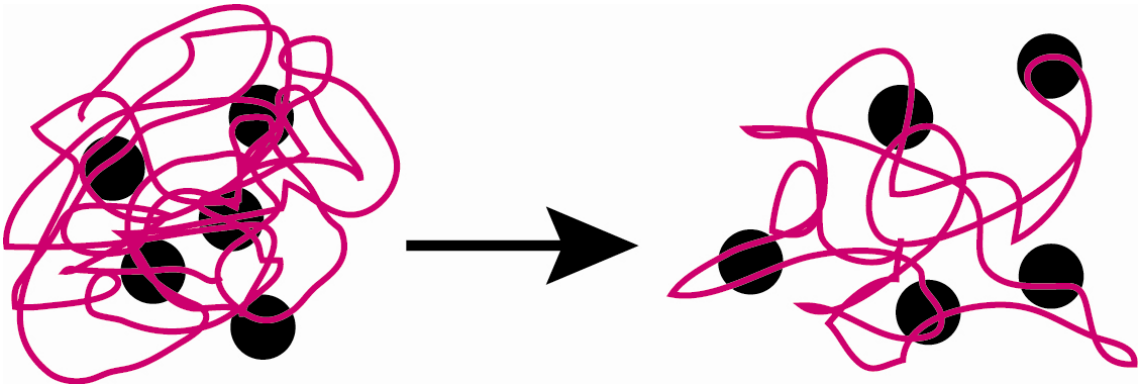

Figure 1-23 A demonstration on how the use of long polymeric chains (such as polyethylene glycol) can be used to coat nanoparticles and make them stealth by the constantly changing conformation making it difficult for the body to recognise them.

Extremely common coatings for iron oxide nanoparticles are hydrophilic polymers, particularly dextran, polyethylene glycol (PEG) and polyethylene oxide (PEO). This

invites stability in aqueous media and lends itself to being able to associate further molecules to it; for instance drugs.[87] These coatings also produce "stealth" properties as their conformation is constantly changing making it difficult for the body to identify and clear them (see Figure 1-23).

Another common coating for iron oxide nanoparticles are liposomes. Liposomes are lipid vesicles which can be formed in mono or multilayers of phospholipids. These are formed by the collapse of a lipid film by hydration (thus causing a swelling) and agitation (to encourage the breakdown of the film), leaving the hydrophilic phosphate head group at the surface and the hydrophobic fatty acid chains pointing into the liposome.[88] The pore inside the liposome allows it to act as a vesicle, this has now led to research into making magnetic liposomes (magnetoliposomes) for use in magnetic hyperthermia; by collapsing the film in the presence of an iron oxide nanoparticle solution (see Figure 1-24).[89]

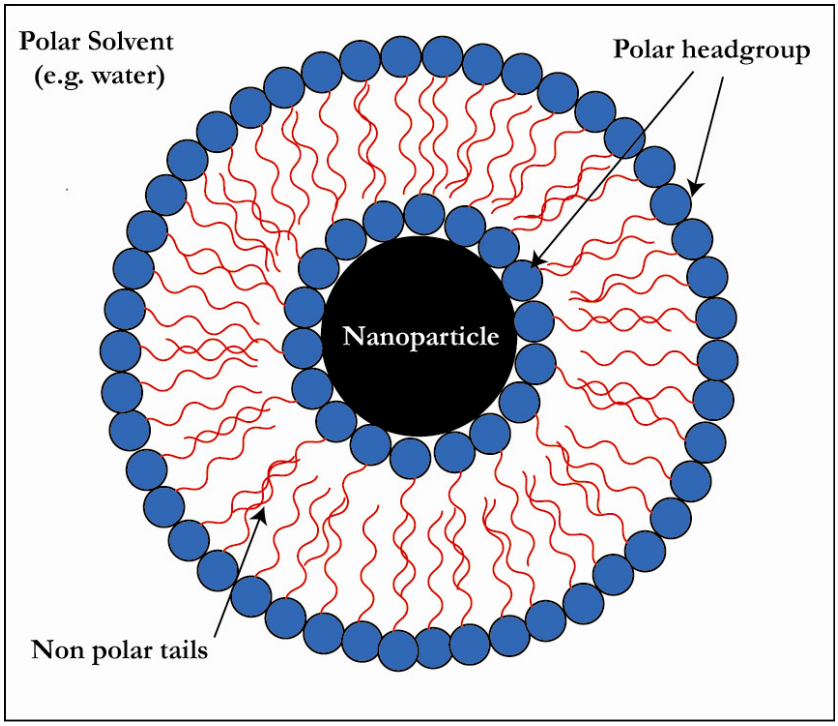

Figure 1-24 A magnetoliposome; a bilayer with the non polar tails pointing within the layers and the polar headgroups on the outside. The nanoparticle is protected inside the core.

Importantly the phospholipid shell is biocompatible and encourages stability in a pH range desirable for biomedical applications. The surface of the liposome is also functionalised, allowing the attachment of targeting molecules, and can be made to work in a stealth mode, for example by using PEG.[90] [91] Alternatively the liposome shell can be made cationic by the addition of an appropriate phospholipid, leading to faster and increased adsorption to cancer cells, due to an electrostatic interaction with their anionic membranes.[92] This area has opened up more avenues to achieving the long term aim of treating cancer using the magnetic hyperthermia phenomenon and has shown promising results in the literature.[93] [94]

1.4.2. MRI Contrast Agents

Magnetic Resonance Imaging (MRI) has been developed using the principles of nuclear magnetic resonance. It uses the magnetic properties of different elements or isotopes to build up a detailed picture of the body. This is most commonly seen using the proton which is in water. When a proton is in an applied magnetic field it will align with the field, when a transverse radio frequency pulse is applied the protons become misaligned and then to get back to the aligned steady state relaxation occurs. The three influences on the image creation and the types of relaxation are:[95, 96]

- The longitudinal relaxation time, T_1
- The transverse relaxation time, T_2
- The spin energy, ϱ

There are two types of contrast agents used in MRI, they are named T_1 and T_2 agents. T_1 agents tend to be used for the imaging of the blood and capillaries, they are generally stealth coated gadolinium particles. Stealth iron oxide nanoparticles (e.g. a polymer such as dextran or PEG) are examples of T_2 contrast agents and they are used in the imaging of the body for diagnostic purposes, e.g. cancers or organ trauma, and distribute themselves in the mononuclear phagocyte system (MPS)

which consists of organs such as the liver and spleen.[97, 98] The contrast agents are used as they improve the image by interacting with, and changing, the protons relaxation time.[99]

The iron oxide nanoparticles have to be delivered in dilute concentrations and therefore they need to possess large relaxivity values.[100]

1.4.3. Magnetic Separation

Magnetic separation is used to separate out a desired material from a mixed solution so that it can be further studied at higher concentrations. Examples that have been reported in the literature have included the identification of malaria in blood samples[101] and the detection of rare tumour cells.[102] This is achieved by functionalising the surface of a magnetic particle with an entity that has an affinity for the desired material. The binding of the magnetic particle with the material needed for further investigation allows the material to be filtered out from the mixed solution by applying an external magnetic field. There are different parameters that will effect the particles attraction to the applied field, namely the:[103]

- Hydrodynamic drag force
- Mediums velocity and viscosity
- Desired materials velocity within the medium
- Magnetophoretic mobility of the particle, largely determined by the size of the magnetic particle.

1.4.4. Drug Delivery

Drug delivery or magnetic drug targeting (MDT) can be achieved using magnetic nanoparticles by attaching the appropriate drug to the nanoparticle. After internalisation of the functionalised ferrofluid an external magnetic field can then be applied to direct the nanoparticles to the desired site (e.g. the organs). Once at the

correct location there is the possibility for the cells to take up the drugs or the entire nanoparticle-drug entity. By improving drug delivery to the specific target allows for a lower drug concentration to be used, thus decreasing negative side effects.[99]

The external magnetic force must be greater than the blood flow rate, which in the case of arteries is 10 cms^{-1} and for capillaries is 0.05 cms^{-1}, so that the particles are kept in the target location.[104]

1.4.5. Magnetic Hyperthermia

By exploitation of the magnetic properties of the nanosized iron oxide it has been shown that a phenomenon named hyperthermia can be used in the destruction of undesirable cells or bacteria.[105, 106] This is an exciting potential therapy as it could replace or reduce the need for more destructive therapies such as chemotherapy.[107, 108]

When a magnetic particle is placed into an AC magnetic field the magnetic moments align in accordance to the field (B) as shown by the hysteresis, Figure 1-1 in 1.2.1, due to the coupling of the energy supplied from the field with the magnetism of the SPION. The energy received from the AC magnetic field is that which is within the boundaries of the hysteresis loop and whilst subjected to this field the material resistance causes it to give out thermal energy - inductive heating. Depending on the size of the particle this can be because of hysteresis or relaxation, because the particles are not in a perfect system they have energy losses, heat, because of friction with the surroundings. It is this heat loss which is harnessed for use in biomedical applications.

As the particle size of an iron oxide nanoparticle decreases, it becomes superparamagnetic and reaches the critical size where hysteresis losses become unimportant and instead relaxation losses dominate. These losses from relaxation

are greater and provide much greater power than hysteric losses from larger ferro- or ferri- magnetic particles.[109]

Cancer, and the conditions in which magnetic hyperthermia can be used to denature cancer cells is discussed in more detail in the following section.

1.4.5.1. The Biology of, and Treatments for Cancer

The area which is causing great excitement is the long term aim that iron oxide nanoparticles could be made cell specific and thus be used to target and denature cancer cells. In the UK in 2004, 284,560 people were diagnosed with cancer and this has steadily increased over the last six years.[110] With worrying figures such as one in three people getting cancer, and one in four men and one in five women dying from the disease, cancer research is a priority not just on a national, but international level.[111]

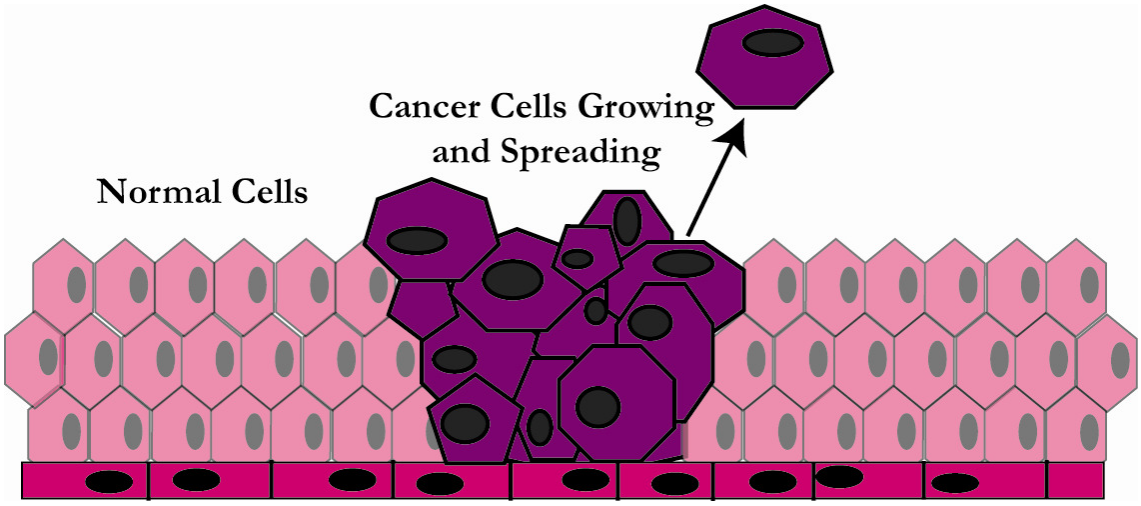

Figure 1-25 The random and uncontrolled growth of cancer cells and how they are spread.

The Penguin Reference Dictionary of Biology describes cancer as being "cells which have escaped normal controls regulating growth and division, producing clones of dividing daughter cells which invade adjacent tissues and may interfere with their activities".[35] In over 90% of cases the mutated DNA has been caused by external

factors, these include; diet, smoking, over exposure to UV rays and viruses. In the other cases the mutated DNA would have been inherited, this is often seen in breast and colon cancers.[112]

The two main pathways for the development of cancer by affecting the cell cycle are the products of either photo-oncogenes or tumour suppressor genes. Photo-oncogenes code for proteins which are responsible for cell growth and division, however if the photo-oncogene is amplified, has a point mutation, or has movement of the DNA, it can become cancer causing by way of overstimulating the cell cycle and is then named an oncogene. On the other hand tumour suppressor genes which limit cell division can also undergo mutation, resulting in the lack of control of cell growth and division. In most cases, cancer is normally induced by multiple mutations and often both oncogenes and the lack or inactivity of tumour suppressor genes are involved. This also explains why the risk of getting cancer increases with age, as there are more mutations building up in the genes.[113]

Treatments of cancer have taken many different pathways, these are often invasive, lengthy and cell indiscriminate, leaving the cancer patient feeling very sick. Often combinations of treatments are used. The treatments for cancer include:[114]

- **Surgery** – the direct removal of a tumour from the body.
- **Chemotherapy** – the use of cytotoxic drugs to kill the malignant cells. Unfortunately healthy cells can also be damaged by the chemotherapy drugs making the patient feel unwell and cause hair loss. However, healthy cells can repair this damage whereas cancer cells cannot so die.
- **Radiotherapy** – the use of radiation (usually X-rays) to damage and kill cancerous cells. There is also an internal radiotherapy whereby a radioactive material is placed on or inside the body or ingested as a drink.
- **Immunotherapy** – this uses biological materials to kill and inhibit cancer growth. Examples of such include; vaccines, gene therapy, cancer growth inhibitors and monoclonal antibodies.

- **Hormonal Therapy** – controlling the production of hormones which is particularly useful in the treatment of breast and colon cancer.
- **Transplants** – particularly of the bone marrow
- **Photodynamic Therapy** – drugs that are activated by a light source which are able to kill cells.
- **Radiofrequency Ablation** – radiowaves which heat and kill cells.

It is anticipated that magnetic hyperthermia could be delivered as a treatment for cancer as when the nanoparticles are harnessed to reach a maximum heating temperature of 42-45^{o}C for a few hours it can be used alongside the delivery of chemotherapy or irradiation, and has been shown to enhance the other treatments. However at 50^{0}C or above, for a few minutes, it is possible to kill the cell completely, this is called thermoblation.[115] However, the nanoparticles are indiscriminate meaning that they can also kill healthy cells. This makes the delivery of the nanoparticles a key issue, and it can be achieved by direct injection of the material into the tumour or by adding targeting moieties to the nanoparticle which give adhesion to cancer cells specifically.

An example in the literature of targeting magnetic nanoparticles to a tumour include the study by Yanase using magnetic cationic liposomes.[116] This work showed that by coating the SPIONs in a cationic liposome shell there was 10 times the affinity for glioma cells compared to neutral liposome shells. This is because cell walls are slightly negatively charged and so the positive charge on the magnetosome promotes adhesion and internalisation.[117]

1.4.6. Iron Nanoparticle Toxicity and Iron Excretion

Studies have shown that iron oxide nanoparticles tend to gather in the liver and spleen. They then overtime get incorporated into haemoglobin. One study using a SPION named AMI-25 showed there were no acute or subactute toxicity in rats and dogs at well over 150 times the recommended dosage.[118] A key issue in the toxicity

of iron oxide nanoparticles is that there is, as yet, no standardisation of protocol. This means that the toxicity is extremely variable, and changes greatly by size, speed of dissolution, dose, method of administration and shell composition. Until there is more harmonisation this becomes very difficult to predict without extensive *in vitro* and *in vivo* trials for each methodology and resultant product.[119, 120]

There are no physiological mechanisms for iron excretion in the body. Instead the iron concentrations deplete from the natural loss of cells for example from the skin, menstruation, mucus, urine and bowel losses.[121 122]

1.5. Thesis Outline

This thesis reports the work undertaken to synthesise iron oxide superparamagnetic nanoparticles (SPIONs) that have biocompatibility for application in magnetic hyperthermia to be potentially used in cancer treatment. The iron oxides magnetite and maghemite are thought to have superior biocompatibility and this is why these materials are researched over others such as nickel or cobalt analogues. All the samples were synthesised using a co-precipitation method which saw ferric and ferrous salts being reduced by a basic surfactant to form the iron oxide.

Chapter 2 briefly explains how the in house magnetic hyperthermia machine works. Chapter 3 investigates how by varying the reaction conditions it is possible to have increased control, and tailor the size of the nanoparticles to create solutions with the desired sizes for optimum heating from magnetic hyperthermia. The heating is induced by an in house built system named MACH.

The iron oxide nanoparticles were found to be unstable at physiological conditions and are non-targeting. Therefore functionalisation of the nanoparticles with carboxylic acid and bisphosphonate ligands was investigated to enable stability in aqueous media, by chemisorption onto the nanoparticle surface (Chapters 4 and 5). Heating and magnetic data was collected from all the samples. The ligands selected

also had other functional groups on them, so that further anchoring of cell specific targeting moieties could be developed. The advanced heating of the tiopronin stabilised nanoparticle allowed for further antimicrobial testing and is the first time magnetic hyperthermia has been used for such an application (Chapter 4).

This thesis is completed by Chapter 6 which covers conclusions and suggestions for further work.

Chapter 2
Magnetic Analytical Techniques

2.1. Introduction

Magnetic analysis can be undertaken using many different strategies, examples include; Mössbauer spectroscopy, superconducting quantum interference devices (SQUID), gaussmeters, Hall effect magnetometers, Guoy balances and fluxgate magnetometers.[123] For the purposes of this investigation SQUID was used to measure the magnetism of the iron oxide nanoparticle materials, due to availability and as it is commonly used in the literature in the measurements of magnetic SPIONs.

The overall goal of this work was to produce magnetic nanoparticles that are biomedically appropriate, and produce fast and efficient heating to its surroundings through magnetic hyperthermia. This is done through an induction heater. The induction heater used in these experiments is novel compared to those used in other work, and so this is described in further detail, along with the definition and

explanation of the parameters used to measure the speed and efficiency of heating from the materials.

2.2. SQUID

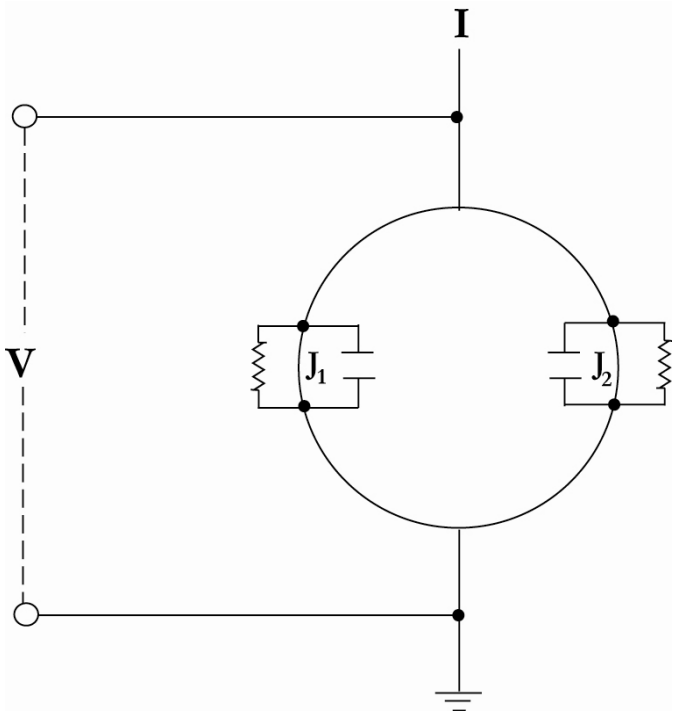

Figure 2-1 A circuit diagram of a dc SQUID superconducting coil, with two Josephson junctions. Adapted from Figure 2 in Jenks et al.[124]

There are two types of SQUID available; the first invented was the direct current (dc), and this was followed by the radio frequency (rf) which was invented by Silver and Zimmerman in 1967.[125] The SQUID works on the phenomena of the Josephson junction, defined by Brian Josephson in 1962, which was shortly derived after the microscopic theory for superconductivity was given in the BCS theory (Bardeen, Cooper and Schrieffer) which described the fundamental particle the Cooper pair (an electron pair with a mass of *2m* and charge of *2e*).[126] A Josephson junction is two semiconductors that when separated by a thin insulator can have a current flow (the electron pairs) through the tunnelling barrier.[125, 127] A dc SQUID operates with two Josephson junctions (see Figure 2-1) and a rf SQUID operates

with one Josephson junction; thus making the dc more sensitive but the rf more economical.[128] The current generated is dependent on the magnetic flux, and therefore the SQUID can be used in magnetic measurement.[12] It is also known to be very sensitive.[72, 124]

The SQUID usually operates at very low temperatures (liquid helium cooled), however there are now, so-called, high temperature SQUIDs emerging that can operate at temperatures around 77 K using conducting ceramics.[128]

Zero field cooling (ZFC) and field cooling (FC) curves are obtained from a measure of magnetisation against temperature in a SQUID (as seen in 1.2.3.8.). The information sought from these curves is about energy barriers that exist in a material (1.3.7.).[129]

The SQUID is also able to measure hysteresis curves by measuring the magnetisation against the applied field. By taking these measurements at different temperatures (e.g. below and above a materials T_B) it is possible to gather further information on this material; including the saturation magnetisation per unit mass, the coercivity of the material and we can also identify superparamagnetism in this way, by looking for hysteresis below T_B and no hysteresis above T_B.

In this work we are looking for evidence of superparamagnetism and a large M_s from the materials synthesised. However, it has been shown that although in ferromagnetic materials there is a direct correlation with large induced heating values (SAR – explained in 2.3.1.) and large M_s and coercivity values, in superparamagnetic materials this is not necessarily the case.[130] The ZFC/FC field curves looks to identify blocking temperatures or Verwey transitions that may be present.

2.3. MACH

Magnetic AC Hyperthermia (MACH) is the name of an in house patented machine, thought of and developed by Mr Simon Hattersley, Prof. Quentin Pankhurst, Dr. Paul Southern and Mr. Mathew Kallumadil. MACH has been developed in response to the lack of adequate induction heaters available on the market that satisfy the criteria of:

- Producing large magnetic fields
- Being tuneable in frequency
- Being practical in clinical applications

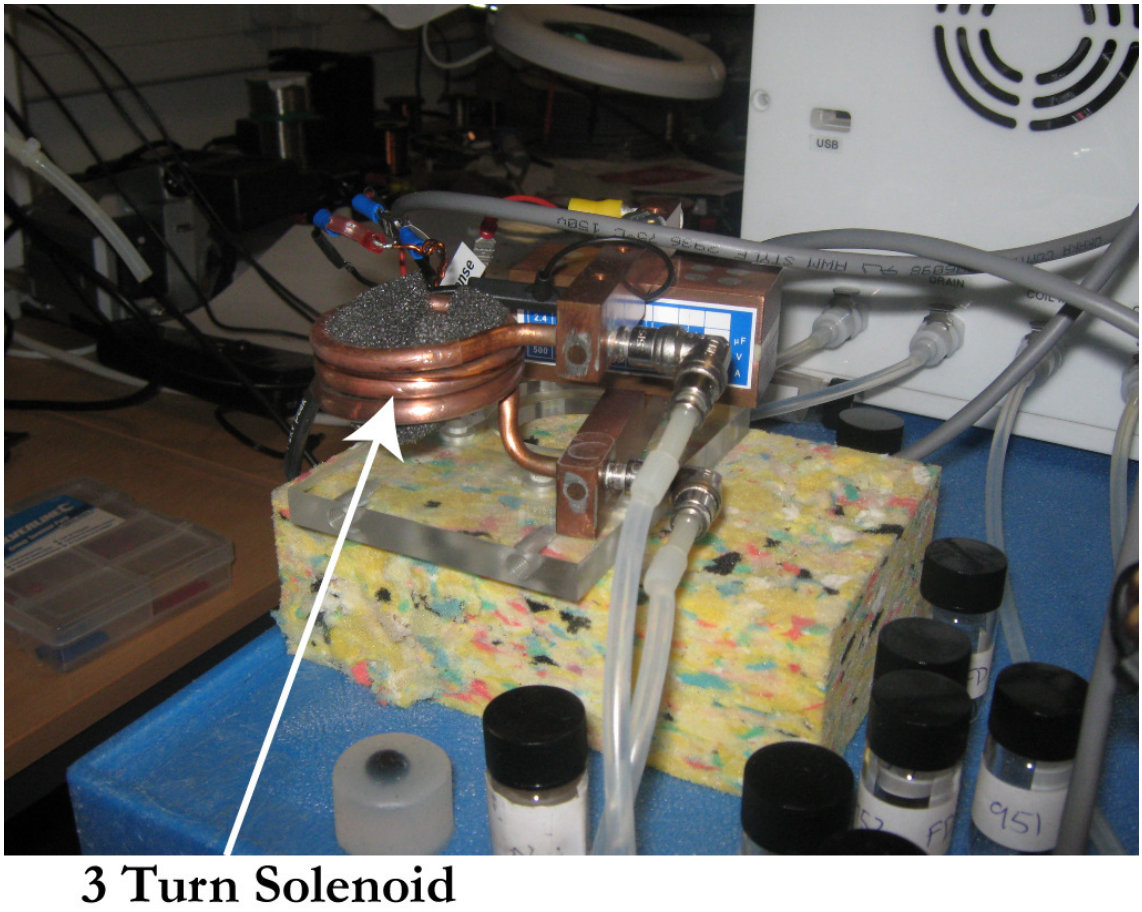

Figure 2-2 Front view of the 3 turn solenoid (coil) used by the magnetic AC hyperthermia (MACH) system to induce heating from a sample.

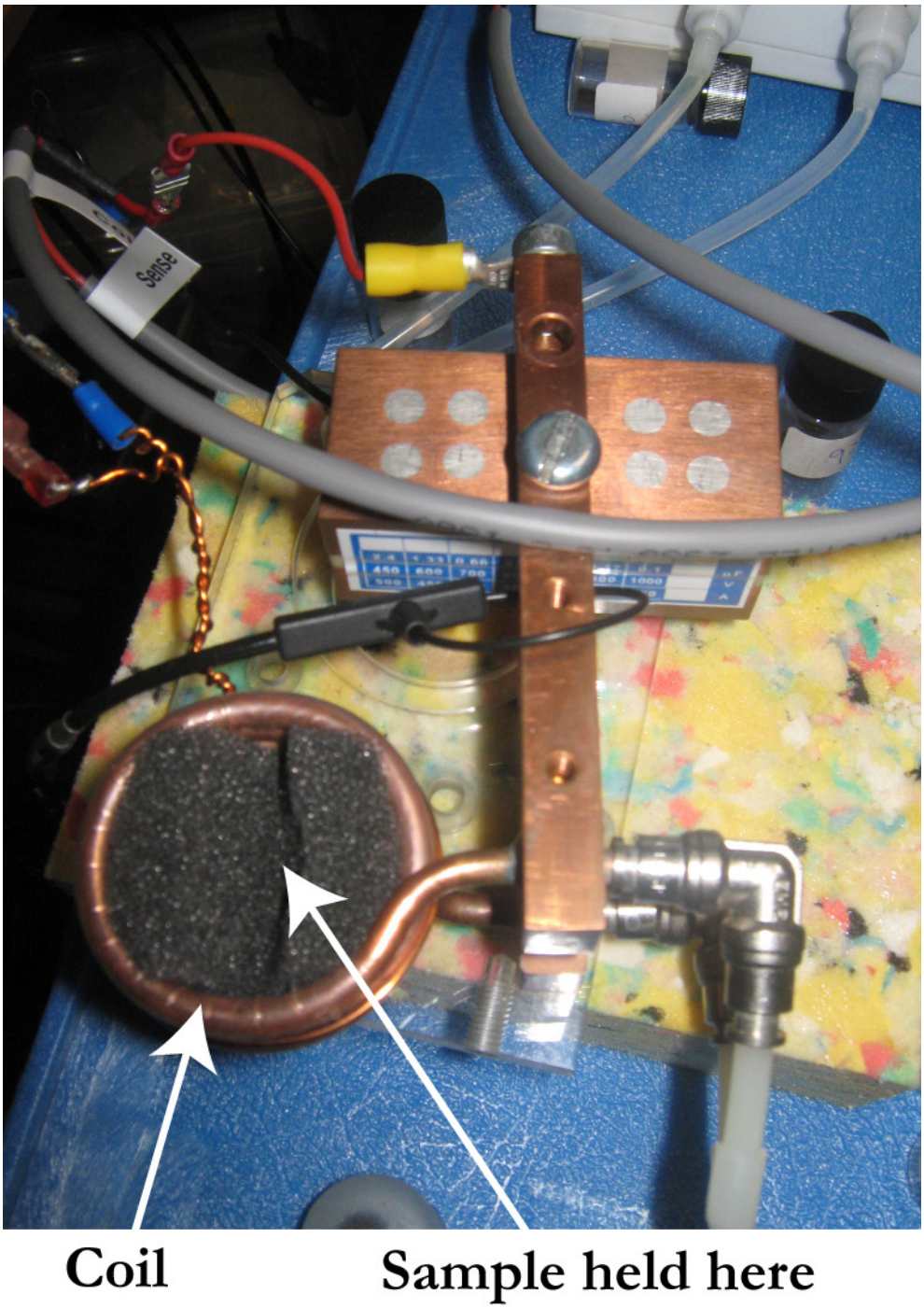

Figure 2-3 A plan view of the coil used in the magnetic AC hyperthermia (MACH) system to induce heating from a sample. The image also shows where the sample tube (a 2 ml eppendorf) is placed.

The inventors have been able to produce a variety of coil appendages that allow the MACH to deliver the inductive heating in a variety of ways, highlighting the versatility of the machine, which is essential if taking this further to clinic and allows

for self-tuning. Figures 2-2 and 2-3 show such a coil. The sample is placed in an Eppendorf (2 ml volume) inside the coil. Upon application of the frequency a temperature probe records the temperature increase of the solution over time.

In this work the magnetic AC hyperthermia (MACH) system was powered by 150 Volts at ca. 0.8 Amps. This encompasses a 2 cm water-cooled coil with 6 windings and provided a field of around 12 kA/m at a frequency of 1.05 MHz. The sample was placed in the centre of the coil in an eppendorf tube. Full coil details are provided in the table below (Table 2-1).

Outer Tube (mm)	5.0
Inner Tube (mm)	3.0
Tube thickness (mm)	1.0
Insulation thickness (mm)	0.25
Coil inner (mm)	20
Pitch (mm)	5.5

Table 2-1 Table giving the dimensions of the 6 turn solenoid used in these magnetic hyperthermia experiments.

The MACH is very much still in development and is currently on its fifth generation. What it is patented for is the use of the control circuit, the electronic breadboard, which generates high magnetic fields in a LC tank, where L is the inductor, the coil, and C is the capacitor. In this work the MACH was operated at a fixed frequency of 1 MHz, however this frequency can be tuned over a range of frequencies using different LC .

2.3.1. SAR and ILP

Commonly, Specific Absorption Rate (SAR) is referred to in the literature when measuring heating properties of magnetic nanoparticles.[131] It is also sometimes

called the specific loss power (SLP) or specific heating power (SHP). How SAR is measured can be seen in Equation 2-1;

$$SAR = \frac{\Delta T}{\Delta t} \cdot \frac{C}{m_{Fe}}$$

Equation 2-1

$\Delta T/\Delta t$ is the initial heat rise, C is the heat capacity of the fluid per unit mass, and m_{Fe} is the iron mass in the fluid per unit mass. This gives SAR the units W/g.[132] The fundamental problem with this parameter is that SAR is extrinsic and varies depending on both H (field strength) and f (frequency). Therefore measurements are only comparable if made on the same machine that has the same H and f.[133]

This major limitation for comparability led members of this research group (Prof. Quentin Pankhurst, Dr. Paul Southern and Mr Mathew Kallumadil) to formulating a new parameter. This is named the Intrinsic Loss Power (ILP). This parameter is not completely intrinsic (but certainly closer to being so than SAR) and is only true if the following assumptions are made:[133]

- The crystallite size has a polydispersity index greater than 0.1
- Frequencies of several MHz
- H is much greater than the saturation field of the nanoparticles
- Similar environmental thermodynamic losses are experienced

Therefore, following these assumptions, ILP is defined as:

$$ILP = \frac{SAR}{H^2 f}$$

Equation 2-2

In this work both SAR and ILP will be given, due to SAR still being greatly used in the literature.

2.3.2. Usable Frequencies

As well as the particle size, shape and cell affinity of the nanoparticles, it is also important that the heat induction is optimised by both the strength of the magnetic field and the frequency, however due to the biomedical application of magnetic hyperthermia, research groups have been looking into finding not just the optimum, but the safest frequency (*f*) and field strength (*H*) possible.

Atkinson et al. in 1984,[134] when magnetic hyperthermia for cancer treatment was still in its infancy, investigated the effect that inductive magnetic frequencies would have on a patient. Their model looked into thermal seeds which were needle like in shape, they found that if the needle was orientated parallel to the field there was a greater power output than if it was perpendicular. Investigations have now gone down the nanoparticle path, for reasons as explained in Chapter 1, however Atkinson et al. did endeavour to establish a usable frequency range that would provide maximum power output from the material whilst reducing the induction of eddy currents within the body tissue. Their suggestion was for the frequency to be less than 200 kHz and the overall *Hf* value should not exceed 4.85 x 10^8 $Am^{-1}s^{-1}$.[134, 135]

The first clinically approved induction heater operated at maximums of 100 kHz and 18kA/m, Hergt and Dutz have suggested that the optimum frequency would be around 500 kHz and a field strength of 10 kA/m.[136] It has also been put forward that the maximum *Hf* value is 6 x 10^6 OeHz for the human body.[130]

The *Hf* value is an important consideration in the design of an inductive heater, as detailed above, particularly in a clinical application. The design of a tuneable machine which can both find an optimum ILP from a particle, alongside being

within the biomedical and economical constraints is being investigated by other members of this research group.

Chapter 3
Coprecipitation Synthesis

3.1. Introduction

As described in Chapter 1, the coprecipitation synthesis of iron oxide nanoparticles is a solution based methodology, whereby salts in a solvent can be precipitated out by making changes to the pH of the solution. In the case of the formation of magnetite these are Fe(II) and Fe(III) salts and the pH adjustment normally made is to increase the basicity of the solution. This type of synthesis was first developed by Massart in 1987.[137] The co-precipitation methodology of iron oxide nanoparticles still requires refinement, including the ability to control many aspects, including; colloidal monodispersity, nanoparticle size tuning, cohesive particle sizing, anisotropy and effects of surfactants or coating.[138] In this chapter the development of an optimised coprecipitation method to iron oxide nanoparticles is presented. Notably the particles made from this study were later shown to be the best ever particles to date for magnetic hyperthermia.

3.1.1. Particle Growth

The stages involved in the coprecipitation technique are saturation, nucleation and growth. These stages need to be controlled so that the resulting product has repeatable and desirable properties, particularly in the case of nanoscience we wish for size control. The first work that details the growth process of monodispersed particle solutions was produced by LaMer and Dinegar and described in 1.3.8.1.[54] Turkevich, when investigating gold sols, found flaws in the LaMer mechanism. He proposed an alternative which saw 3 steps; nucleation, growth and coalescence.[139]

Liftshitz and Slyozov[56] described the kinetics of how precipitation occurs in supersaturated solutions, they covered two types of diffusion. The first was the growth of a grain which then redissolves back into the now only slightly supersaturated solution. The other method was the growth of larger particles from smaller ones; they named this coalescence, this was a follow on from that that which had been described by Ostwald in the Ostwald ripening process (see 1.3.8.1.). Liftshitz and Slyozov's work was further developed by Wagner and the full kinetic theory for the speed of growth of grains is called the LSW theory.[55]

In 1998, Watzky and Finke proposed a new mechanism, following the inadequacies with those such as LaMer's (the model seems to only hold true for closely related systems to that of sulphur sols) and Turkevich's. Their new mechanism suggests that there is slow and continuous nucleation followed by a fast and autocatalytic surface growth step.[140, 141]

Tiemann et al. define coalescence as being the collision of two particles at a correct orientation causing unity brought about through Brownian motion. They have also accumulated the various forms of coalescence defined by various groups in the literature and investigated combinations instead of just one mechanism for the formation of growth of ZnS nanoparticles.[142]

3.1.2. Particle Size and the Coprecipitation Method

Groups have shown that by altering conditions in the coprecipitation method it is possible to gain control over the nanoparticles size and edge towards monodispersity. These methods have included;

- **By varying the concentrations of the iron reactants –** increasing the concentration makes the resulting nanoparticles larger. [143]
- **The pH -** a stronger reducing agent gives rise to smaller crystals.[104]
- **Using surfactants –** different surfactant types and concentrations can improve the nanoparticle synthesis by overcoming interparticle attractive forces such as Van der Waals and magnetic.[144-146]
- **Ionic strength –** Increasing the ionic strength of the medium decreases the particle size[147]

3.1.3. Chapter Motivation

Despite the vast amounts of literature on nanoparticle formation and growth kinetics there has not been a thorough investigation on the way surfactant/reducing agent addition and temperature, in the iron salt reduction to iron oxide nanoparticles, occurs. As detailed above, it is now believed that not only particle size and shape but particle cluster sizes are of importance in the type of hyperthermic response to an inductive magnetic field.

This chapter looks to fill such a gap in the literature by investigating these two key areas:

- The salt solution temperature upon surfactant/reducing agent addition
- Surfactant/reducing agent rate of addition to the salt solution

Our hypothesis is that by measuring particle size, cluster size and polydispersity of the nanoparticles in these two experiments, it is possible to identify trends, and therefore allow increased control and selectivity when synthesising SPIONs.

3.2. Methodology

3.2.1. Materials

All chemicals were purchased from Sigma Aldrich and were used as received with no further purification; iron (III) chloride hexahydrate (99%), iron (II) chloride tetrahydrate (≥99%) and tetramethylammonium hydroxide (25% in water w/w) (TMAOH). All water used was distilled and was 15 MΩ.

3.2.2. Synthesis

To determine the effect of temperature and rate of addition of the reducing agent on the particle size the other parameters needed to be kept consistent. All reactions were carried out in air in a sealed vessel to maintain the concentration. Steam was produced from the exothermic reaction. A 250 ml conical flask was used and all reactions were stirred magnetically with a 1.5 cm magnetic stirring bar. The $FeCl_2.4H_2O$ solution was stored under nitrogen until the reaction was due to begin, so as to minimise oxidation. A disposable 10 ml standardised syringe was used for the addition of the TMAOH.

3.2.2.1. Synthesis for Observation of Temperature Effect

In a typical reaction 1.485 g, 5 mmol, of $FeCl_3.6H_2O$ was dissolved in 5 ml of distilled water in a 250 ml conical flask. To this 1.25 ml of a stock solution of $FeCl_2.4H_2O$ (0.498 g, 2.5 mmol) was added. The flask was then sealed with a subaseal and magnetically stirred on a hot-plate stirrer. A temperature probe and

thermocouple was placed inside the reaction vessel and set to the desired temperature. Once at this temperature 10 ml of TMAOH was syringed into the reaction in one continuous addition, taking 1 minute in total. This was done by hand, not using a syringe drive. This reaction was removed from heat (if being heated – see Table 3-1) and stirred for a further 45 minutes at room temperature. The magnetic stirring bar was then removed and the solution poured into a sample vial. The conical flask was washed with 20 ml of distilled water and collected in the sample vial. The temperatures chosen for the reactions were room temperature (20^0C), 50^0C and 70^0C. See Table 3-1 for an overview of the synthesis parameter.

For TEM, zeta sizer and hydrodynamic size measurements the solutions were diluted down to 1 mg of nanoparticle per millilitre of solvent.

3.2.2.2. Synthesis for Observation of the Effect of the Rate of Addition of Reducing Agent

In a typical reaction 1.485 g, 5 mmol, of $FeCl_3.6H_2O$ was dissolved in 5 ml of distilled water in a 250 ml conical flask. To this 1.25 ml of a stock solution of $FeCl_2.4H_2O$ (0.498 g, 2.5 mmol) was added. The flask was then sealed with a subaseal and magnetically stirred on a hot-plate stirrer. A temperature probe and thermocouple was placed inside the reaction vessel and set to the desired temperature (either room temperature or 70 ^{0}C). Once at this temperature 10 ml of TMAOH was syringed into the reaction in either:

- Continuous addition over 1 minute
- In 1 ml increments, every 1 minute
- Continuous addition over 5 minutes
- Continuous addition over 10 minutes

This reaction was removed from heat (if being heated, Table 3-1) and stirred for a further 45 minutes at room temperature. The magnetic stirring bar was then

removed and the solution poured into a sample vial. The conical flask was washed with 20 ml of distilled water and collected in the sample vial. See Table 3-1 for an overview of the synthesis parameters.

For TEM, zeta and hydrodynamic size measurements the solutions were diluted down to 1 mg/ml.

Reaction Number	Temperature / ^{0}C	Reducing Agent Addition
1	20	Continuous addition over 1 minute
2	50	Continuous addition over 1 minute
3	70	Continuous addition over 1 minute
4	20	Incremental, 1 ml added every 1 minute
5	20	Continuous addition over 5 minutes
6	20	Continuous addition over 10 minutes
7	70	Incremental, 1 ml added every 1 minute
8	70	Continuous addition over 5 minutes
9	70	Continuous addition over 10 minutes

Table 3-1 The reaction temperature and the rate of addition of the reducing agent, tetramethylammonium hydroxide, in the formation of iron oxide nanoparticles made in a co precipitation method for the samples named 1-9.

3.3. Results

The particle size was observed using TEM measurements and hydrodynamic size measurements. These were carried out on a Philips EM208 transmission electron microscope at a voltage of 120 kV. The zeta measurements and hydrodynamic size measurements were obtained using a Zetasizer Nano ZS (Malvern Instruments,

Mavern, UK). The software ImageJ was used to measure the particle sizes on the TEM images. Measurements were taken in triplicate.

3.3.1. Results of Temperature Effect on Particle Size

The iron oxide nanoparticle samples **1**, **2** and **3** were synthesised at room temperature, 50^0C and 70^0C respectively. They were made by reducing a 2:1 ratio of Fe(III):Fe(II) from the metal salts using an excess of TMAOH. The reducing agent/surfactant was added continuously from a 10 ml disposable syringe over a 1 minute period. The reactions were carried out in air, but in a sealed vessel and stirred magnetically. The solutions were diluted to 1 mg of nanoparticles per ml for all measurements.

Sample	Reaction Temperature /^{0}C	Hydrodynamic Size/ nm				Polydispersity Index			
		1	2	3	Average	1	2	3	Average
1	20	63	64	64	**64**	0.22	0.22	0.20	**0.21**
2	50	104	104	104	**104**	0.21	0.21	0.21	**0.21**
3	70	111	111	112	**111**	0.22	0.22	0.18	**0.21**

Table 3-2 The hydrodynamic sizes and polydispersity indexes, in triplicate and mean average, for three iron oxide nanoparticle samples formed at different reaction temperatures in a coprecipitation method.

The hydrodynamic size measurements and their relative polydispersity were measured three times for accuracy. The results for this can be seen in Table 3-2. The average hydrodynamic size for **1**, **2** and **3** were 64, 104 and 111 nm respectively, Figure 3-1 shows this graphically for clarity. This shows that with increasing reaction temperature there is an increase in the average hydrodynamic size. The polydispersity index of all three samples was an average of 0.21 which indicates all three preparations gave low particle size dispersity (also shown in Figure 3-1). The

line of best fit for the graph indicates a possible proportional relationship between temperature and hydrodynamic particle size. The R^2 value is 0.93 and the equation for the line is;

$$y = 0.98x + 48$$

Equation 3-1

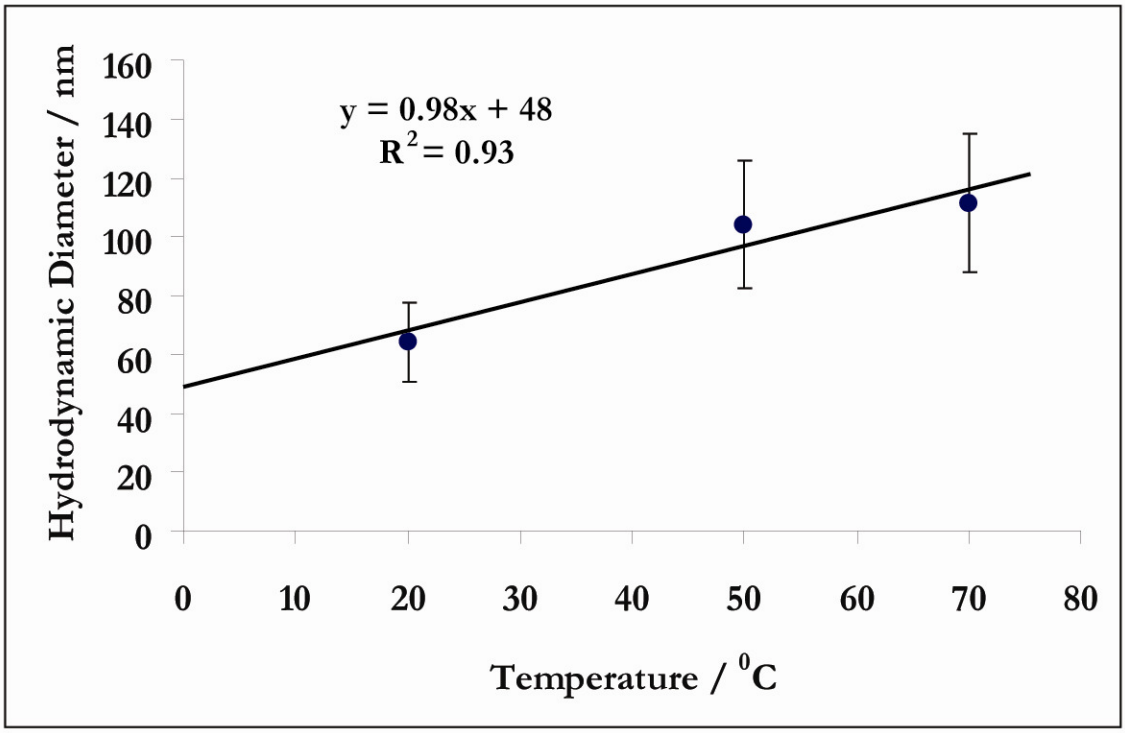

Figure 3-1 A graph displaying the mean average hydrodynamic size of iron oxide nanoparticles formed at different reaction temperatures in a coprecipitation method. The error bars indicate the polydispersity and the trend line indicates a possible proportional relationship.

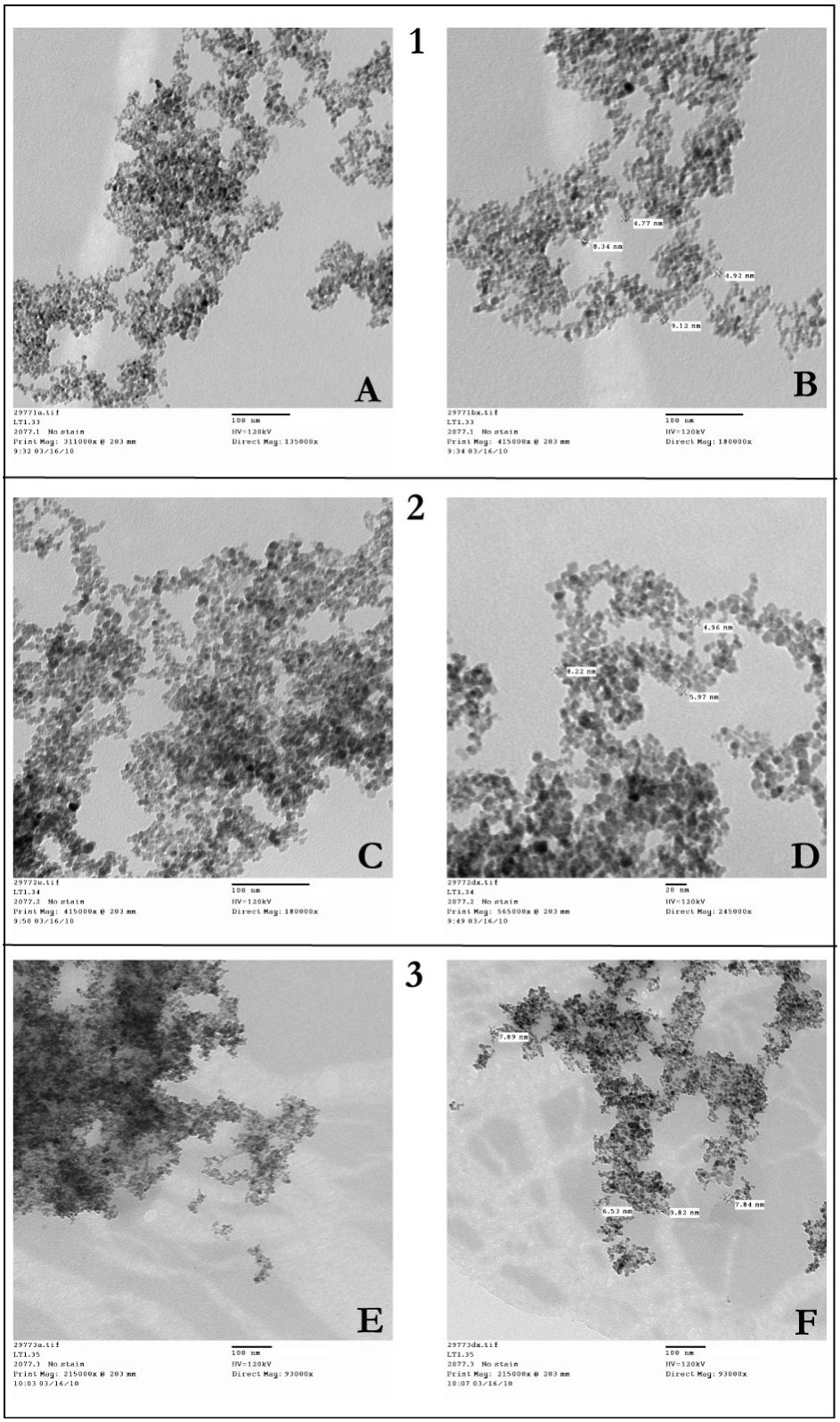

Figure 3-2 HRTEM images of iron oxide nanoparticles formed by a coprecipitation method at different reaction temperatures. A & B = 20^{0}C, C & D = 50^{0}C, E & F = 70^{0}C. All scale bars are 100 nm except for D which is 20 nm.

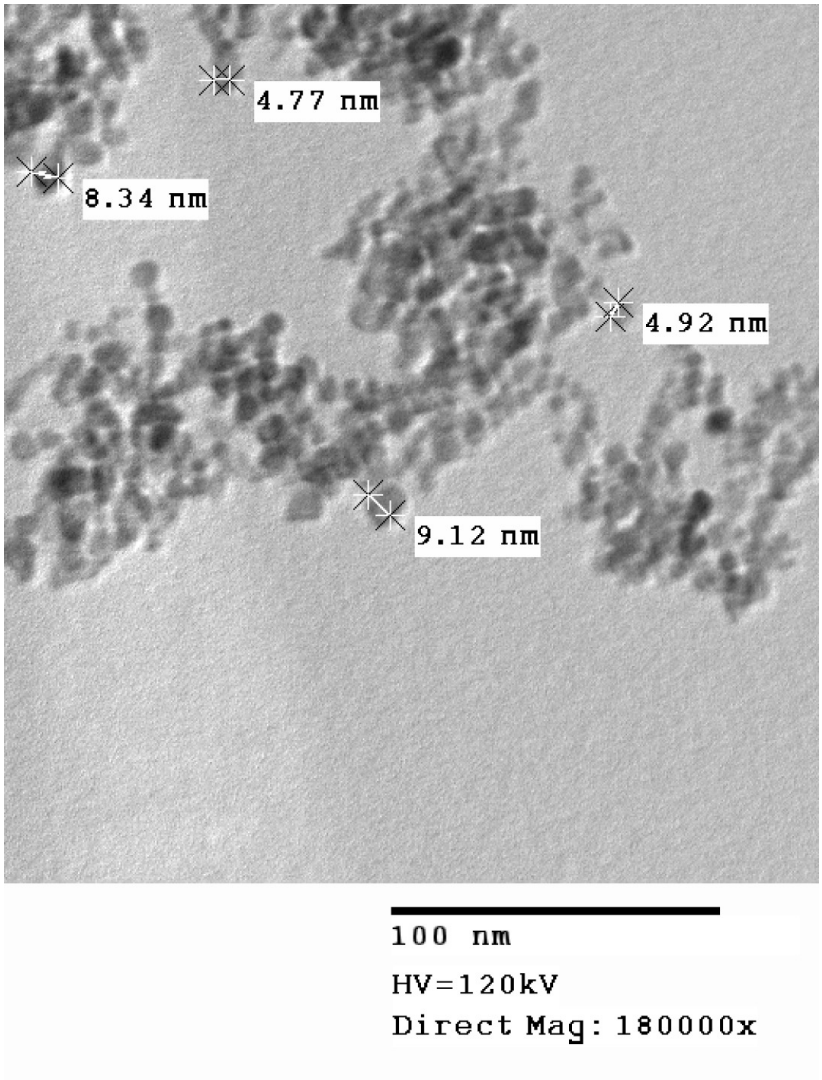

Figure 3-3 HRTEM close up image of the iron oxide nanoparticles synthesised *via* a coprecipitation method at 20^{0}C. The full image is shown in Figure 3-2, 1B.

HRTEM images were taken for samples **1**, **2** and **3**. These can be seen in Figure 3-2. For clarity on shape and size a close up image of **1** is shown in Figure 3-3.

The zeta potentials for **1**, **2** and **3** all gave charge values at -40. This would indicate the particles were all negatively charged.

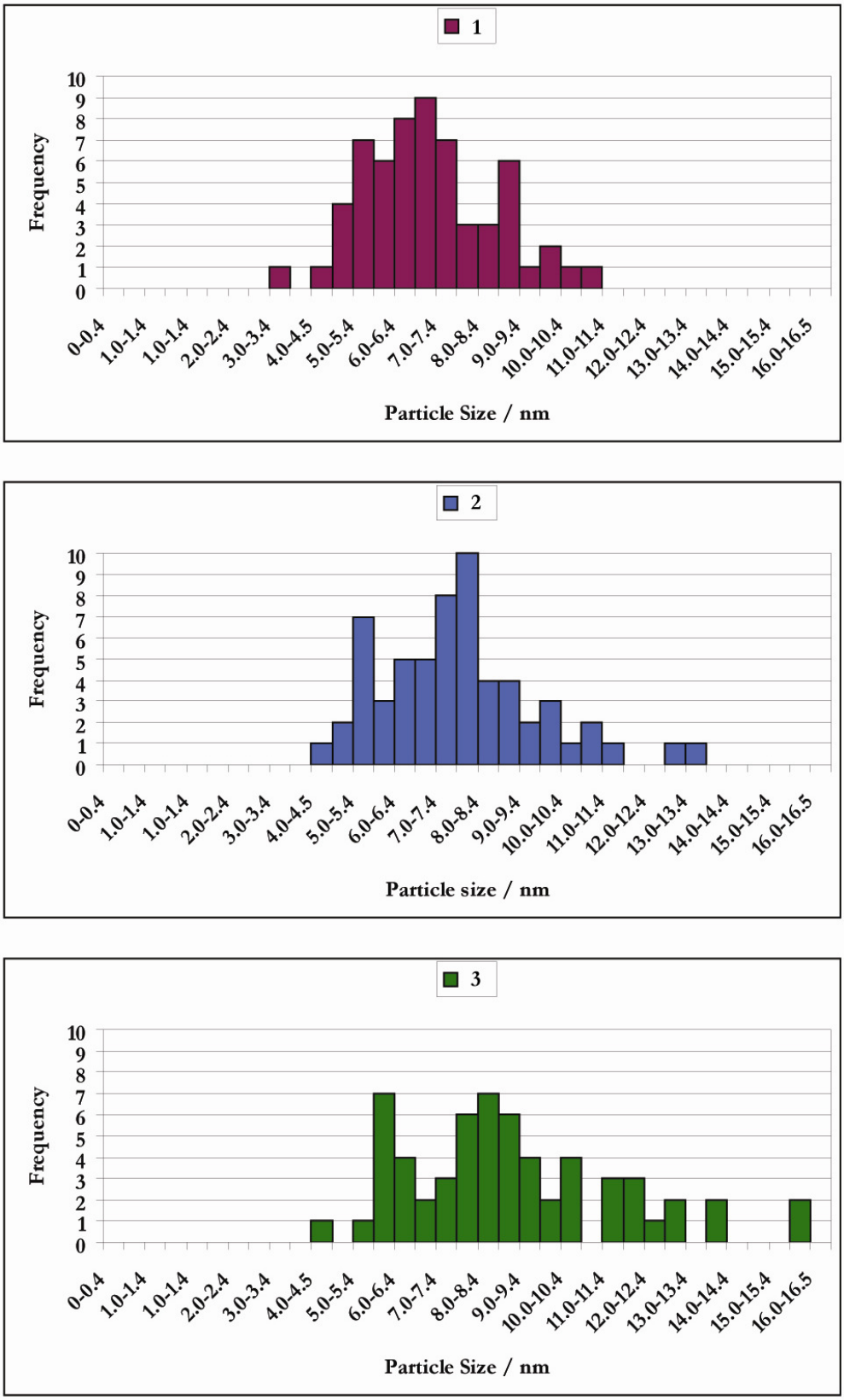

Figure 3-4 Histograms showing the spread of the 60 measurements of particle sizes of iron oxide nanoparticles synthesised *via* a coprecipitation method at 20^{0}C (1), 50^{0}C (2) and 70^{0}C (3).

Sample	Reaction Temperature / ^{0}C	Mean Particle Size Diameter / nm	Standard Deviation / nm
1	20	**6.78**	**1.55**
2	50	**7.49**	**1.92**
3	70	**8.75**	**2.55**

Table 3-3 Table displaying the mean particle size and standard deviation of iron oxide nanoparticles synthesised using a coprecipitation method at various temperatures.

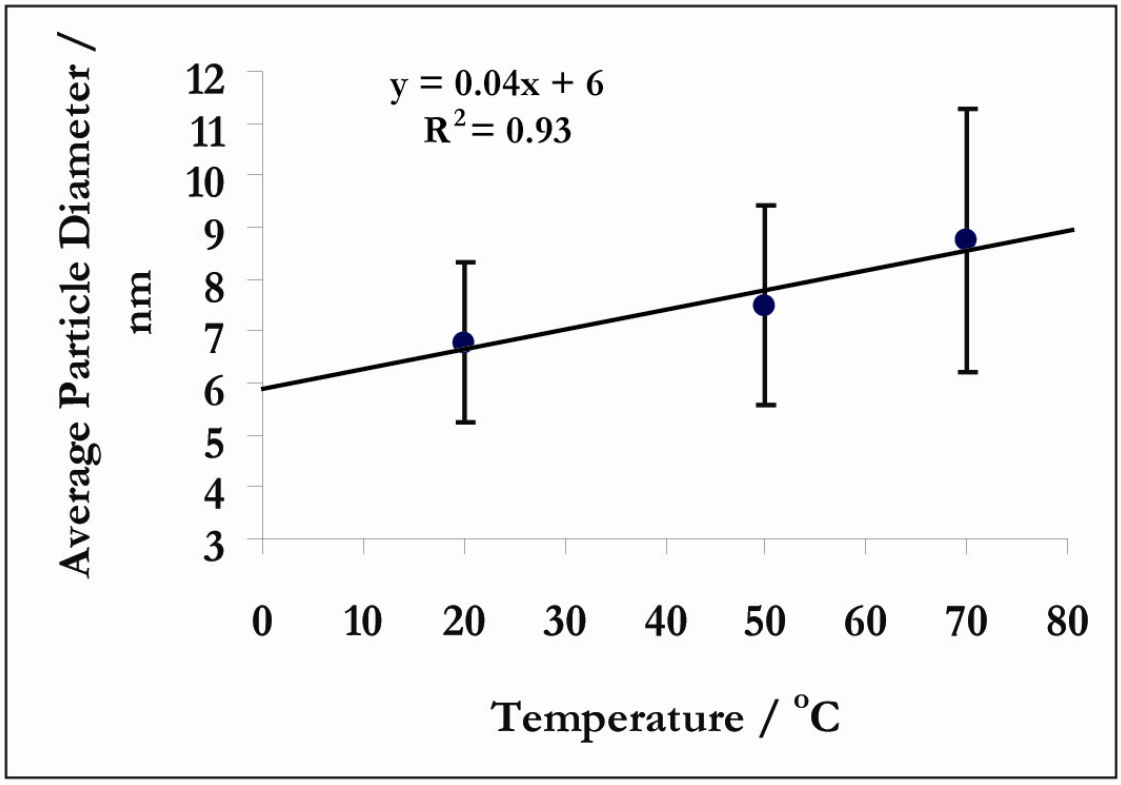

Figure 3-5 Graph showing the mean particle size and standard deviation for 60 measurements taken of iron oxide nanoparticles synthesised *via* a coprecipitation method at varying temperatures. A line of best fit is also shown with the formula and R^2 value.

Figure 3-4 displays histograms of the 60 particle measurement results for samples **1**, **2** and **3**. The mean average of these results and then the standard deviation was calculated and the results are shown in Table 3-3 and Figure 3-5. The results indicate that with increasing temperature there is a particle size increase and the standard

deviation increases indicating increased polydispersity. Figure 3-5 demonstrates this graphically and also shows a line of best fit that has the equation;

$$y = 0.04x + 6$$

Equation 3-2

With an R^2 value of 0.93. This indicates that there may be a linear dependence on particle size with increasing temperature.

3.3.2. Results for Method of Addition of Reducing Agent on Particle Size

The iron oxide nanoparticle samples **1**, **4**, **5** and **6** were synthesised at room temperature. They were made by reducing a 2:1 ratio of Fe(III):Fe(II) from the metal salts using an excess of TMAOH. The reducing agent/surfactant was added in four separate ways from a 10 ml disposable syringe continuously over a 1 minute period, in incremental doses of 1 ml every 1 minute, continuously over 5 minutes and continuously over 10 minutes respectively. The reactions were carried out in air, but in a sealed vessel and stirred magnetically.

The iron oxide nanoparticle samples **3**, **7**, **8** and **9** were synthesised at 70^0C. They were made by reducing a 2:1 ratio of Fe(III):Fe(II) from the metal salts using an excess of TMAOH. The reducing agent/surfactant was added in four separate ways from a 10 ml disposable syringe continuously over a 1 minute period, in incremental doses of 1 ml every 1 minute, continuously over 5 minutes and continuously over 10 minutes respectively. The reactions were carried out in air in a sealed vessel that was stirred magnetically.

All the samples were then diluted in water to a concentration of 1 mg of nanoparticle/ml for further measurement.

Sample	Reaction Conditions at 20^0C	Hydrodynamic Size / nm	Polydispersity Index
1	Continuously over 1 minute	**64.0**	**0.21**
4	Incremental, 1 ml added every 1 minute (total time period of 9 minutes elapsed)	**58.1**	**0.26**
5	Continuously over 5 minutes	**66.6**	**0.25**
6	Continuously over 10 minutes	**77.8**	**0.31**

Table 3-4 The hydrodynamic sizes and polydispersity indexes of iron oxide nanoparticles formed *via* a coprecipitation method at 20^0C with varying reducing agent addition rates.

Sample	Reaction Conditions at 70^0C	Hydrodynamic Size / nm	Polydispersity Index
3	Continuously over 1 minute	**111.3**	**0.21**
7	Incremental, 1 ml added every 1 minute (total time period of 9 minutes elapsed)	**298.3**	**0.43**
8	Continuously over 5 minutes	**210.7**	**0.35**
9	Continuously over 10 minutes	**266**	**0.41**

Table 3-5 The hydrodynamic sizes and polydispersity indexes of iron oxide nanoparticles formed *via* a coprecipitation method at 70^0C with varying reducing agent addition rates.

The hydrodynamic size measurements and zeta potentials were measured for all cases and TEM images were gathered for the data collected at 70^0C. Tables 3-4 and 3-5 show the hydrodynamic diameters and polydispersity indexes for the

measurements taken at room temperature (20^0C) and 70^0C respectively. In all cases the zeta potentials were negative.

Figure 3-6 shows the hydrodynamic sizes of both sets of data displayed in Tables 3-4 and 3-5.

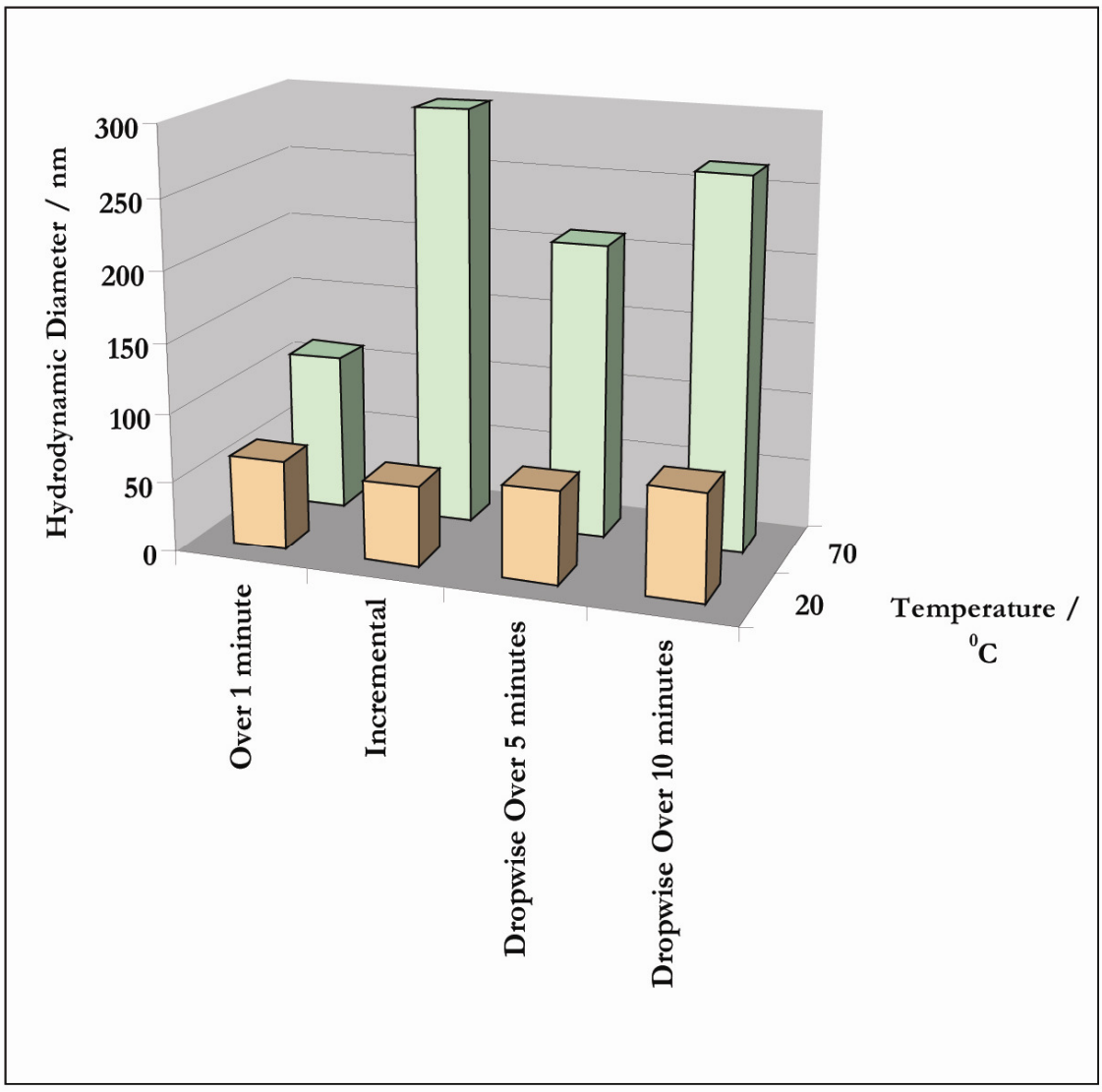

Figure 3-6 Graph displaying the effect of the rate of addition of a reducing agent at temperatures of 20^0C and 70^0C on the hydrodynamic size of iron oxide nanoparticles synthesised using a coprecipitation method.

The polydispersity indexes (PDI's) for the 8 different samples also varied dependent on the type and rate of addition of the reducing agent. The PDI increased with

addition time. Also the incremental addition increased the PDI. This can be seen in Figure 3-7.

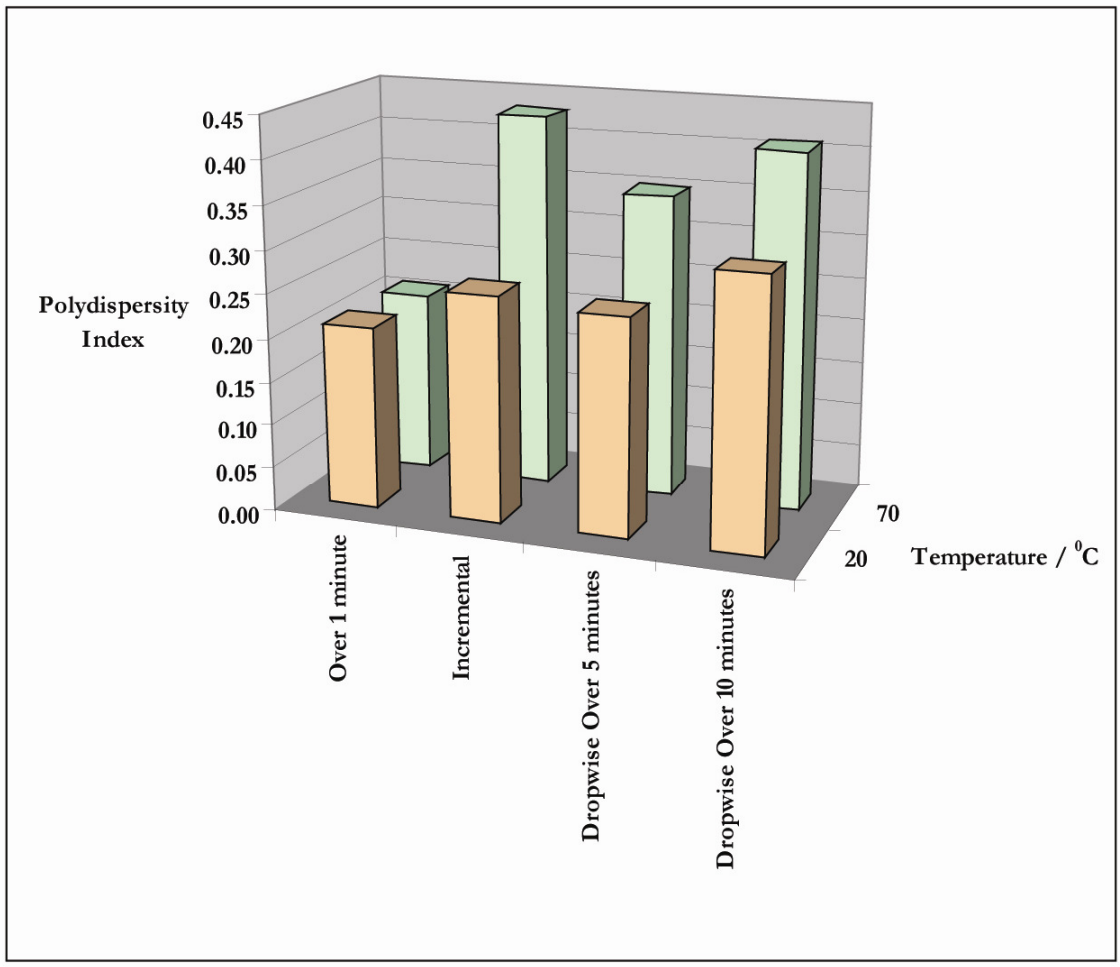

Figure 3-7 Graph displaying the effect of the rate of addition of a reducing agent at temperatures of 20^{0}C and 70^{0}C on the polydispersity index of iron oxide nanoparticles synthesised using a coprecipitation method.

A plot of the hydrodynamic diameter *versus* the rate of addition of reducing agent was run to look for an inverse relationship (Figure 3-8). The data alludes to this in the case of the 70^{0}C but less so for the 20^{0}C, this may be due to the first measurement anomaly (**1**).

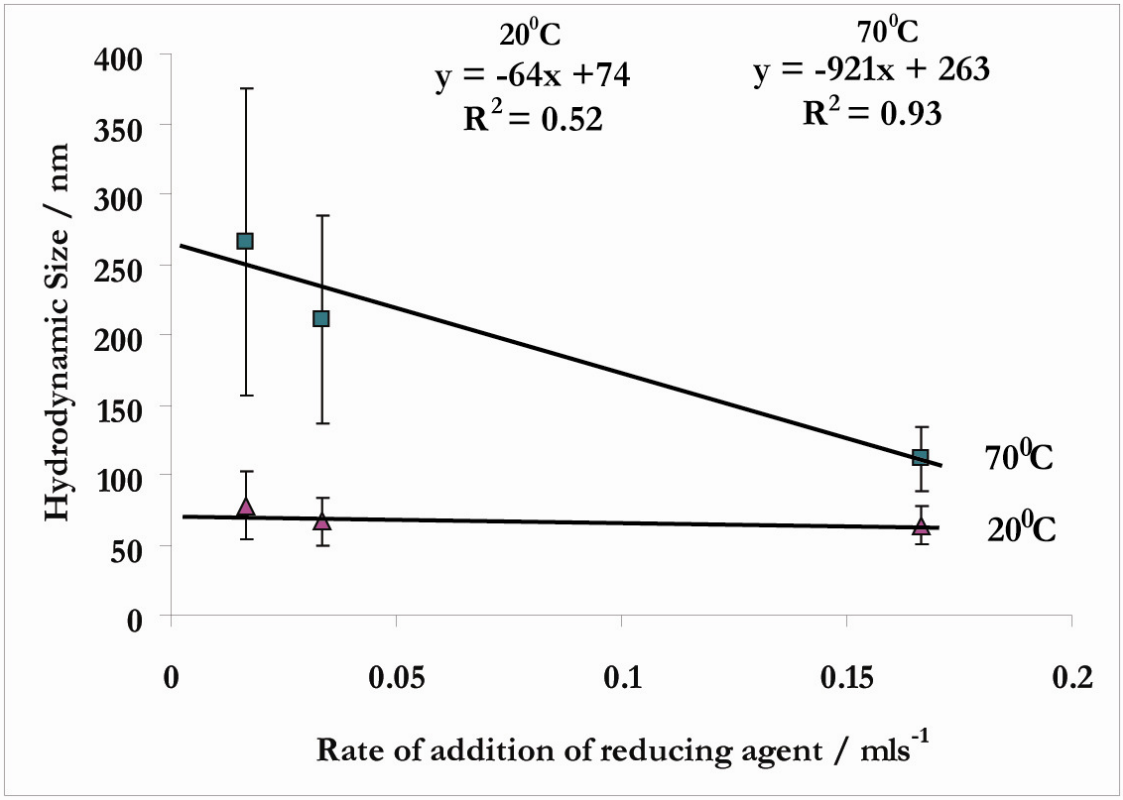

Figure 3-8 Graph displaying tentative evidence for an inversely proportional relationship between the rate of addition of the reducing agent *versus* the hydrodynamic cluster size of iron oxide nanoparticles formed *via* a coprecipitation method at 20⁰C an 70⁰C. The polydispersity range is indicated by the error bars.

TEM images were collected for the data collected at 70⁰C, to identify any effects that the rate and type of surfactant addition may have on the particle sizes. These TEM images can be seen in Figure 3-9. Figure 3-10 is a close up image of image A from Figure 3-9 so that the morphology of the particles can be viewed with greater ease.

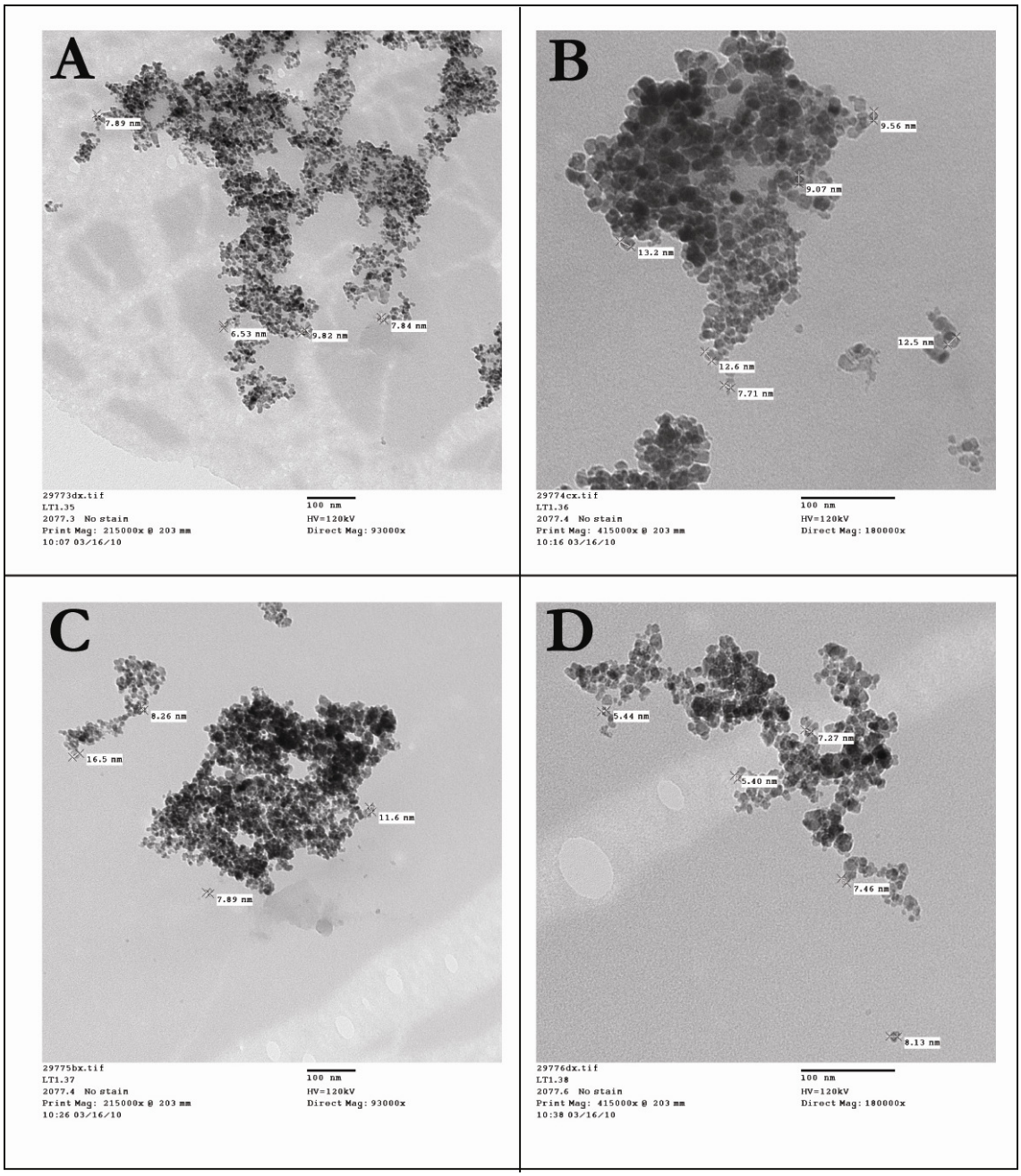

Figure 3-9 HRTEM images of iron oxide nanoparticles synthesised at 70^{0}C *via* a coprecipitation method. The rate of addition of 10 ml of reducing agent was varied by A) Added over 1 minute B) Incremental, 1 ml added every 1 minute C) Continuously over 5 minutes D) Continuously over 10 minutes. All scale bars are 100 nm.

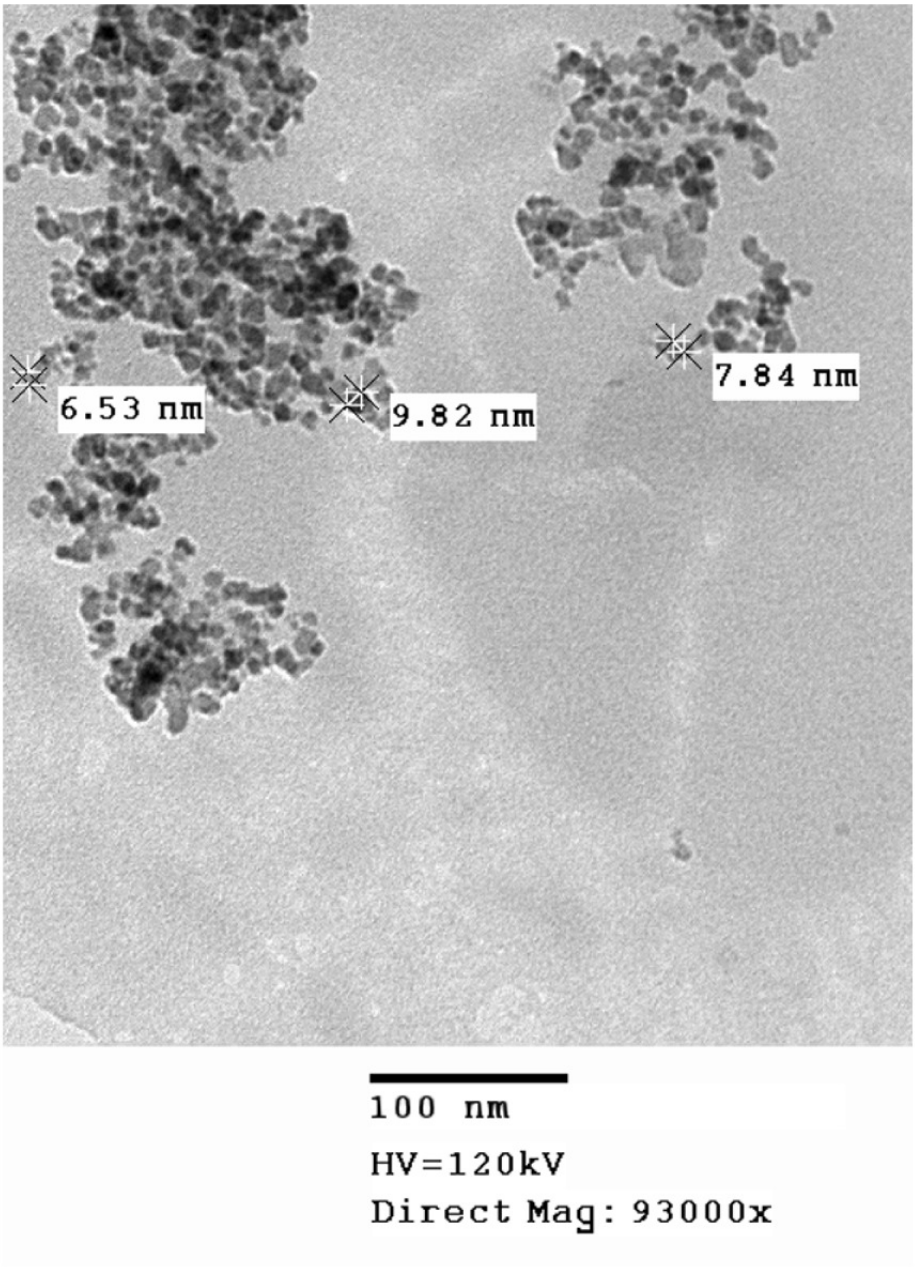

Figure 3-10 Close up of image A from Figure 3-9. HRTEM of iron oxide nanoparticles synthesised *via* a coprecipitation method at 70^{0}C and by adding 10 ml of the reducing agent over a 1 minute period.

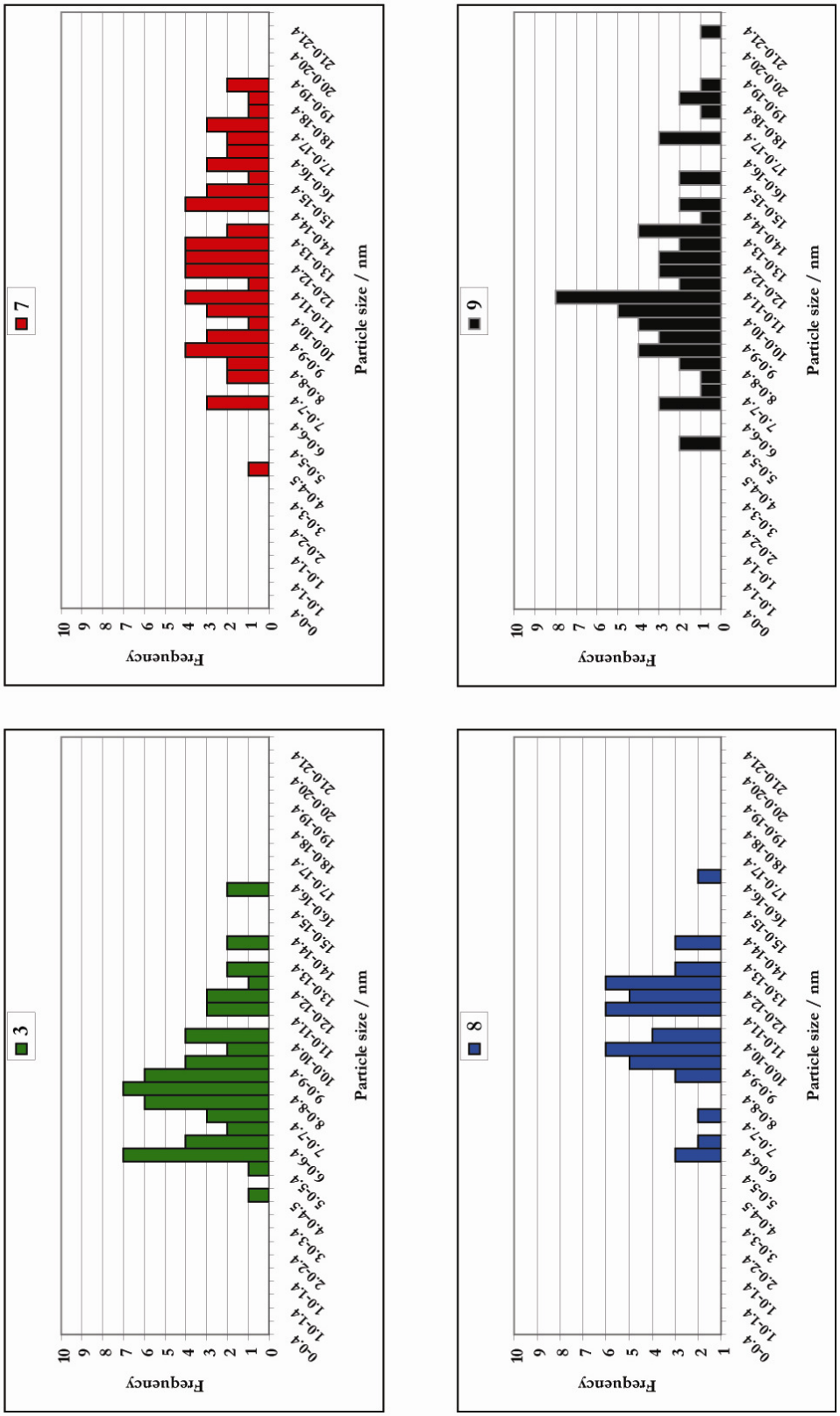

Figure 3-11 Histograms showing 60 particle size measurements per iron oxide nanoparticle sample synthesised *via* a coprecipitation method at 70^{0}C. The rate of addition of 10 ml of reducing agent was varied by 3) Added over 1 minute 7) Incremental, 1 ml added every 1 minute 8) Continuously over 5 minutes 9) Continuously over 10 minutes.

Sample	Reducing Agent Addition	Mean Particle Diameter / nm	Standard Deviation / nm
3	Over 1 minute	**8.8**	**2.6**
7	Incremental	**12.4**	**3.5**
8	Over 5 minutes	**11.0**	**3.0**
9	Over 10 minutes	**11.5**	**3.4**

Table 3-6 The mean particle sizes and standard deviations of 60 iron oxide nanoparticles formed *via* a coprecipitation method at 70^{0}C with varying reducing agent addition rates.

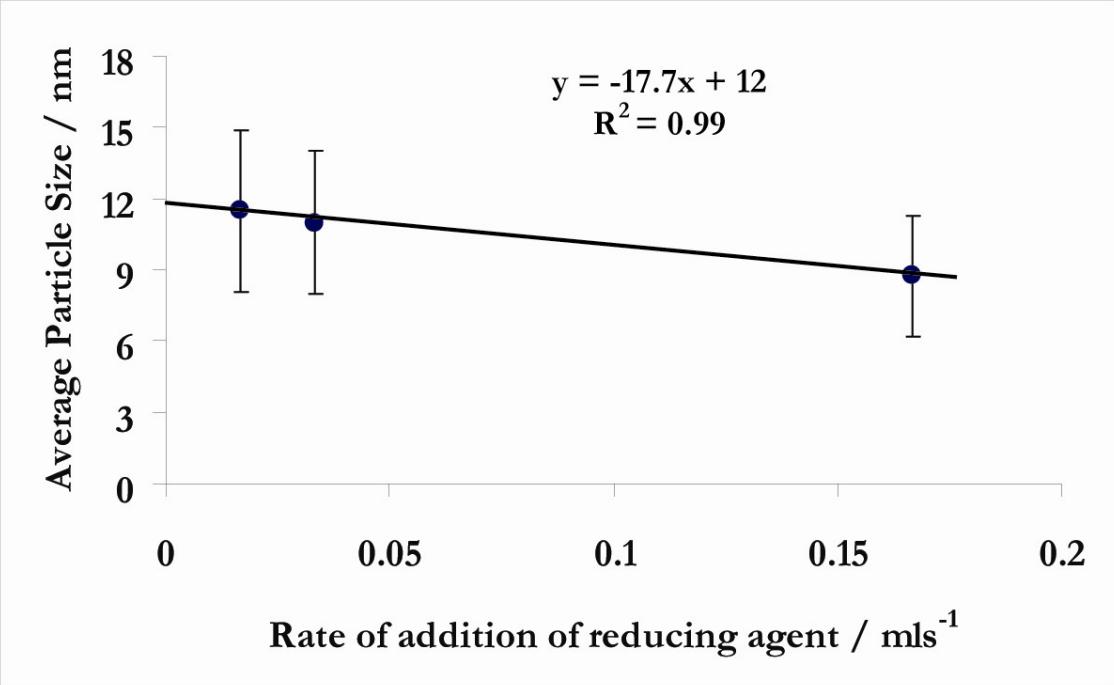

Figure 3-12 Graph showing the inversely proportional relationship between the average iron oxide nanoparticle size and the rate of addition of the reducing agent. The error bars indicate the standard deviation and each point was the average of 60 measurements made. The synthesis was a coprecipitation method at 70^{0}C.

Figure 3-11 shows the 60 particle size measurements for **3**, **7**, **8** and **9**. The mean average and standard deviation for these results are presented in Table 3-6. When converting **3**, **8** and **9** into rates of addition (ml s^{-1}) there is an inverse proportionality relationship between particle size and the rate of addition of the

reducing agent. **7** was omitted from this treatment due to the incremental pattern of addition, this was not a steady flow so the rate can not be determined.

Figure 3-12 shows the average particle size against the rate of addition of the reducing agent, and also has error bars showing the standard deviation of the 60 measurements. The graph demonstrates that the line of best fit has and R^2 value of 0.9936 and the equation is;

$$y = -17.7x + 12$$

Equation 3-3

3.4. Discussion

3.4.1. Discussion of Temperature Effect on Particle Size

The results show that increasing the temperature of the coprecipitation reaction increases both the nanoparticle crystal diameter and the hydrodynamic diameter of the particle clusters.

The average polydispersity of the clusters were all 0.21, indicating that the increase in temperature has no effect on creating a wider size distribution; however, when looking at these polydispersities graphically (Figures 3-1 and 3-5) it is obvious that the actual polydispersity range does increase with reaction temperature. In the case of particle size there did seem to be an increase due to the increase in temperature, implying there was greater polydispersity in reactions carried out at higher temperatures.

There seems tentative evidence that both particle diameter and cluster hydrodynamic diameter have a linear relationship with increased temperature (Figures 3-1 and 3-5).

A plausible explanation for this is that by increasing the reaction temperature there is more energy within the solution, this would increase mobility and cause a greater number of collisions between the particles. This thermodynamic explanation calls into question the commonly put forward effect of Ostwald ripening as the growth mechanism. Instead we postulate a different model for the growth mechanism of these particles and clusters.

As discussed in 3.1.1., there is an alternative model - coalescence. The data suggests that the rise in thermal energy increases Brownian motion and thus collisions. By more collisions occurring between the particles, there is a greater probability that they will be correctly orientated to join together. This in its very essence is coalescence, and in light of the evidence provided this seems the most probable mechanism for growth within the coprecipitation of ferrous and ferric ions. It does not, however, provide details on the nucleation occurring and further investigation would need to be carried out to provide a full model.

This coalescence model in a coprecipitation method seems to mimic the growing evidence from Penn and Banfield, that iron oxide particles grow by coalescence in orientated attachments in hydrothermal conditions in biomineralisation.[148, 149]

3.4.2. Discussion on the Method of Addition of Reducing Agent on Particle Size

In the case of hydrodynamic cluster sizes, two sets of data were sought. Both looked at how the rate and type of addition would change the size but were carried out at two different reaction temperatures; 20^0C and 70^0C. For now, the three methods of constant addition of the reactant (over 1 minute, 5 minutes and 10 minutes) will be

discussed as for these the rate of addition is known. The incremental form of addition will be discussed separately.

3.4.2.1. Continuous Addition

Firstly, in the case of nanoparticle size when the reducing agent is added quickly the average diameter decreases, as does the polydispersity. Again, there is tentative evidence that there is an indirectly proportional relationship between particle size and the rate of addition of the reducing agent (a reactant) as shown in Figure 3-12.

In the case of the hydrodynamic cluster size and for both sets of data there was an increase in size when the rate of addition of the reactant was slowed. Following the actual particle size, there was again an increase in polydispersity with the larger hydrodynamic diameter, thus with the decrease in addition rate. This seems to follow an inverse linear relationship between the cluster size and rate of addition, although it could be argued that the data sets at 20^0C are particularly weak, however, it does seem evident that the measurements taken at 20^0C over a 1 minute addition seem somewhat of an anomaly and should therefore maybe be discounted (Figure 3-8).

As seen in the temperature effect results, hydrodynamic cluster size and nanoparticle size seem to follow a similar pattern. Both are larger and less monodisperse when the rate of addition of the reducing agent is slowed. In this case it seems that a thermodynamic explanation is weak and instead a kinetic theory seems more likely. By decreasing the rate of addition of the reactant there is a longer time for nucleation and growth. This increase in time means that there is no longer a short sharp burst of nucleation followed by a growth phase, but constant nucleation and growth occurs simultaneously. After nucleation, the smaller particles then get engulfed by the larger particles in solution to reduce the surface energy, thus following an Ostwald ripening growth mechanism. This would also go somewhat to explain the increase in polydispersity; the longer between points of nucleation the

longer the time there is for growth, therefore the particles formed at the start of the addition would have a longer growth period than those formed at the end of the addition.

3.4.2.2. Incremental Addition

The incremental addition shows surprising results. For the 70^0C data set the hydrodynamic size, particle size and both polydispersity measurements are greater than those measured for the continuous addition over 10 minutes. However in the 20^0C data set the hydrodynamic size was the smallest of all the measurements and the polydispersity was between 5 and 10 minute continuous additions. Even forgoing the anomaly that is the continuous addition over 1 minute for 20^0C the hydrodynamic size was less than that of the 5 minute continuous addition.

The incremental addition was carried out by the addition of 1 ml at every 1 minute interval, accumulating in a total elapsed time period of 9 minutes (540 s). In both data sets the measurements do not fall, as expected, between the 5 and 10 minute continuous addition. Infact, the vast differences implies that incremental addition is a far less predictable method of adding a reactant to a solution and renders the experimentalist helpless in the control of the resultant particle and cluster sizes and should therefore be avoided.

Some possible explanations for the results seen are:

- **In the case of the 70^0C data set –** Every 1 minute there is a rapid and brief period of nucleation, which is then followed by a long growth period before the next point of nucleation. In this growth period there are more opportunities for bigger particles to form by both coalescence and Ostwald ripening. This also gives increased breadth in the size distribution due to the time delays between the next point of nucleation and so the gap between the first formed and the last formed particles is wider; this follows what has just

been described in 3.4.2.1 but is more pronounced because the times of nucleation are wider spread and are of greater intensity when they occur.

- **In the case of the 20^{0}C data set –** This result is harder to explain. However, this may be possibly due to thermodynamics. When there are the short sharp bursts of nucleation there is less thermal energy driving Brownian motion, less coalescence occurs, but this is the same for the continuous method of addition too. However, a larger concentration of small nuclei (more nucleation) in a burst may well limit Ostwald ripening compared to a small concentration of small nuclei (less nucleation) occurring with greater frequency. This would need much more investigation to be conclusive.

3.5. Conclusion - A New Mechanism?

This investigation hopes to have proved the need to reconsider the long standing view in much of the scientific community that nanoparticle growth occurs purely by Ostwald ripening.[73, 150] Instead, a combined mechanism is more appropriate, which models how different reaction conditions may then lead to a preferred growth pathway. In the control and desired reproducibility of nanoparticle synthesis the thorough understanding of these factors and influences are key, especially if, as in the case of SPIONs for magnetic hyperthermia, the eventual aim is for scale-up and biocompatibility. Here follows a summary of what has been concluded from these results and what needs further investigation.

3.5.1. What we have so far

The results from this chapter show that:

- Changes in particle size and polydispersity are mirrored by hydrodynamic size and polydispersity, thus cluster size and particle size are intrinsically linked, which is to be expected as bigger particles would form bigger clusters.
- Temperature of the reaction is proportional to particle size/cluster size and polydispersity.
- This can be explained by thermodynamics whereby increased thermal energy gives rise to more particle collisions and the probability of these collisions being correctly aligned for agglomeration increases.
- This implies that with increasing temperature a coalescence mechanism is favoured over an Ostwald ripening mechanism for particle growth.
- This coalescence growth method, as beginning to be believed is the growth mechanism in hydrothermal syntheses, looks to be true in a coprecipitation synthesis.
- The rate of addition of the reducing agent is indirectly proportional to particle/cluster size and polydispersity.
- This has a kinetics explanation whereby nucleation and growth are occurring simultaneously. The increases in time between points of nucleation allow longer growth periods and a greater difference in particle sizes. Therefore an Ostwald ripening mechanism is preferred with a decrease in the rate of addition of the reducing agent.
- Adding the reducing agent in a non-continuous form should not be preferred as the mechanisms at work are more complicated and the resultant product has less predictability.

3.5.2. What is missing

These results tell us information on temperature and reactant addition rate effects, however to build a full and conclusive model on the formation and growth of iron oxide nanoparticles in a coprecipitation method, these further additional factors would need incorporation;

- Reactant concentrations
- Strength of the reducing agent
- Surfactant contributions, although in this example the reducing agent is also the surfactant
- Turbulence (mixing) contributions

With this information, and by building a full model that takes into account the occurrence of preferential growth mechanisms in different conditions, an automated coprecipitation process may be possible that provides the experimentalist with the opportunity for size tunability and monodispersity of nanoparticles and nanoparticle clusters.

Chapter 4

Synthesis of Iron Oxide Nanoparticles in the Presence of Carboxylic Acid Functionalised Ligands

4.1. Introduction

The stabilisation of nanoparticulate iron oxide, as discussed in Chapter 1, is vital for biomedical applications, as iron is not stable at physiological pH and will agglomerate rendering it useless for cell targeting. Many groups of molecules have been shown to interact with the iron oxide nanoparticle surface to give this stabilisation. Such examples of this are siloxanes,[151-153] phosphonates,[154-156] phosphates[157] and long chain hydrophilic polymers such as polyethylene glycol

(PEG),[158-161] polyethylene oxide (PEO),[162] proteins,[163, 164] albumin[165] and dextran,[105] with the oxygen providing the surface interaction with the iron.[166]

Another functional group that has been used is the carboxylic acids,[167, 168] most prominently oleic,[86] lauric,[169] myristic[170] and folic acids.[85] Oleic acid, myristic acid and lauric acid are long chain fatty acids which are not soluble in water, thus to gain water solubility these groups can be substituted with more appropriate molecules or have further functionalisation creating a multi-step process, so that a transfer from organic solvents to water can be made. Folic acid has been used, as not only is it a stabilising agent but it also has some targeting properties useful for the anticancer application of magnetic hyperthermia, due to the folate receptors which are expressed by areas of new and rapid cell growth, such as that seen in cancers.[171]

4.1.1. Bacterial Infections

Hospital acquired infections (HAI's) are regularly reported in the news and a major concern for the government, sparking a huge initiative in trying to irradicate these within public buildings which administer health care. This is due to the potentially life threatening consequences of infection to a person with an already compromised immune system.[172]

One of the most commonly reported is the various drug resistant *Staphylococcus aureus* group, for example MRSA (methicillin resistant *Staphylococcus aureus*). These types of bacteria are commonly found, and many people are carriers of these bacteria without experiencing any sickness. The bacteria becomes significant when a person becomes ill and their immune system weakens, resulting in less ability to fight infection.

It is therefore of high importance to irradicate these types of harmful bacteria, particularly in places where there are sick people. This has seen advancement in a variety of areas including antimicrobial surfaces and coatings, antimicrobial cleaning

products and an increased need in finding indiscriminant treatments to replace antibiotics to which, overtime, bacteria can build up resistance.[173-177]

4.2. Chapter Motivation

The literature has a wealth of evidence showing that carboxylic acids can be used to stabilise iron oxide nanoparticles, preventing agglomeration and promoting biocompatibility. However, as described above, these are all long chain molecules, C≥12 or a similary sized molecule such as folic acid. There has been little investigation into the smaller molecules that contain a carboxylic acid. These molecules tend to be hydrophilic due to their polarity and ability to hydrogen bond, which is beneficial in both the synthesis of the nanoparticles and for use in forming a biocompatible ferrofluid.

Due to the proven reactivity of a carboxyl group with an iron oxide nanoparticle other short chain carboxylic acid functionalised ligands were chosen for further investigation. Alongside the –COOH group, for attachment chemistry for antibody fragments further functional organic groups were needed. This chapter reports the findings of the addition of four shorter chained carboxylic acid functionalised ligands in a one pot synthesis for the formation of iron oxide nanoparticles. The ligands chosen, and the reasons for this, are detailed below in 4.2.1.

This work also shows how magnetic hyperthermia can be used to kill harmful bacteria such as *Staphylococcus aureus* and could be used in treatment for diseases such as septacemia. Thermotherapy kills the bacteria and is indiscriminate, meaning that the bacteria will not be able to acquire any resistance to hyperthermia treatments. The antibacterial study in this chapter is, to our knowledge, the first ever report of using magnetic hyperthermia to kill bacteria.

4.2.1. Ligand Selection

Due to the requirements of the project to use magnetic hyperthermia in biomedical applications the carboxylic acid functionalised ligands had to satisfy certain criteria. These criteria were:

- They were water soluble so that there would be no need for a phase transfer
- Had at least one carboxylic acid group for nanoparticle conjugation
- They had at least one other functional group (carboxylic acids were acceptable) for antibody fragment attachment
- Preferably they were small molecules so that the shell would not dominate the core
- Preferably they had already proven biocompatibility

The ligands selected were aminooxoacetic acid (oxamic acid), butanedioic acid (succinic acid), N-(2-Mercaptopropionyl)glycine (tiopronin) and ethylenediaminetetraacetic acid (EDTA). See Figure 4-1.

Tiopronin is a pharmaceutical drug which goes under the trade name of Thiola. It is used in the treatment of the hereditry disease called cystinuria.[178] Cystinuria causes kidney stones due to poor cystine reabsorption.[179]

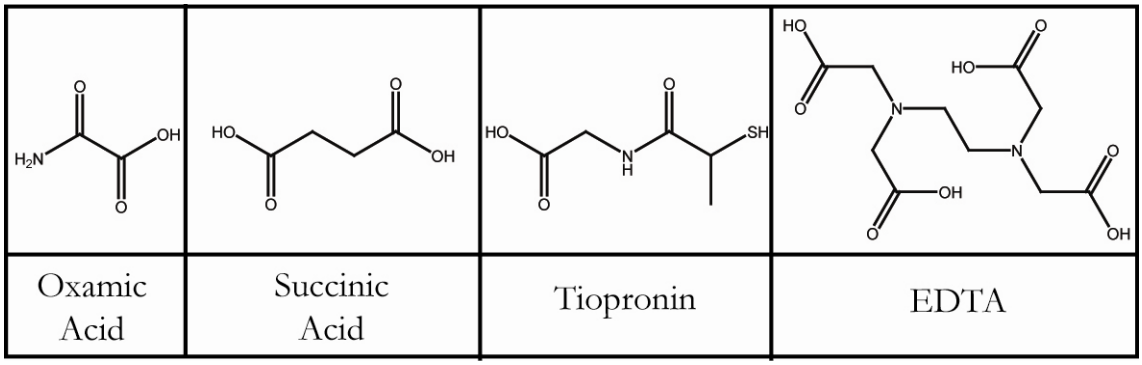

Figure 4-1 The 4 carboxylic functionalised ligands selected to coat iron oxide nanoparticles in a coprecipitation method.

EDTA is a well known strong chelating agent.[35] It chelates strongly to Fe^{3+}. EDTA is used biomedically in chelation therapy[180, 181] and to enlargen root canals in dental surgery.[182]

4.3. Synthesis

The methodology was adapted from a hydrothermal synthesis by Daou et al but using different conditions and with the addition of ligands.[183] The initial part of their synthesis was a coprecipitation method which was followed by hydrothermal treatment. 10 ml of 1M $FeCl_3.6H_2O$ was mixed with 2.5 ml of $FeCl_2.4H_2O$ at 70^0C under argon, followed by the addition of 21 ml of 25% TMAOH. Stirring continued for 20 minutes and the contents then placed in an autoclave for the hydrothermal treatment. In this work, only the coprecipitation part is done. Furthermore a new procedure was worked out for isolating the particles.

4.3.1. Materials

All chemicals were purchased from Sigma Aldrich and were used as received with no further purification; iron (III) chloride hexahydrate (99%), iron (II) chloride tetrahydrate (≥99%), tetramethylammonium hydroxide (25% in water w/w) (TMAOH), N-(2-Mercaptopropionyl)glycine (tiopronin) (≥98%), aminooxoacetic acid (oxamic Acid) (≥98%), butanedioic acid (succinic Acid) (99+%) and ethylenediaminetetraacetic acid anhydrous (EDTA) (≥99%). Resovist was received from Bayer Schering and Nanomag D100 was kindly donated by Micromod. All water used was distilled.

4.3.2. Tiopronin, Succinic Acid and Oxamic Acid

10 mmol of $FeCl_3.6H_2O$ in degassed water was placed into a round bottomed flask under constant nitrogen flow. To this was added 5 mmol of $FeCl_2.4H_2O$ in degassed water and 5 mmol of either tiopronin, oxamic acid or succinic acid. Due to the

magnetic nature of the desired product the reactants were stirred mechanically using an overhead stirrer. The flask was heated in a silicone oil bath to 70^0C. Once at temperature, 21 ml of TMAOH (25% in water w/w) was added dropwise to the vigorously stirred solution. A black precipitate formed. After addition of the TMAOH the flask was immediately removed from the heat source under constant stirring.

Once at room temperature the solution was made up to 50 ml with distilled water and then transferred to a wet 20 cm strip of dialysis tubing (cellulose membrane, M.W. 12,400, average flat width 79 mm). This was secured and fastened at both ends and a magnetic stirrer attached. The membrane was placed into a 5 L beaker with approximately 4.5 L of 15 MΩ distilled water and stirred by placing on a magnetic stirrer plate. The water was recharged daily for 4 days. Upon completion of the dialysis, the membrane was removed and its contents placed in a beaker whereby the precipitate was removed from the majority of the solvent using a strong magnet. The product was placed in a -80^0C freezer overnight, frozen and put under a high vacuum to remove the remaining solvent. This freeze drying process took between 2-3 days and left a dry, fine black powder which still displayed magnetism characteristics when in a magnetic field.

Generally, approximately 1 g of powder was recovered. 0.5 g of this was suspended in 10 ml of deionized water with the aid of sonication in an ultrasonic bath. The resultant pH of the three different solutions from the resuspended nanoparticles was 6.96, 3.95 and 6.65 for the tiopronin, oxamic acid and succinic acid stabilised iron oxide respectively (50 mg/ml and room temperature).

4.3.3. EDTA

In the case of Ethylenediaminetetraacetic acid (EDTA), the *in situ* methodology needed to be adapted. The strongly chelating chemistry of the EDTA with iron meant that an intractable mixture was formed and the iron oxide was no longer free

to form nanoparticles. The method was changed so that the EDTA was added post nanoparticle formation.

10 mmol of $FeCl_3.6H_2O$ in degassed water was placed into a round bottomed flask under constant nitrogen flow. To this was added 5 mmol of $FeCl_2.4H_2O$ in degassed water. Due to the magnetic nature of the desired product the reactants were stirred mechanically using an overhead stirrer. The flask was heated in a silicone oil bath to 70^0C. Once at temperature 21 ml of TMAOH (25% in water w/w) was added dropwise to the vigorously stirred solution. A black precipitate formed. After addition of the TMAOH the flask was immediately removed from the heat source under constant stirring. Once at room temperature an aqueous solution containing 5 mmol of EDTA was added and the solution stirred overnight. This was then made up to 50 ml with distilled water and then transferred to a wet 20 cm strip of dialysis tubing (cellulose membrane, M.W. 12,400, average flat width 79 mm). This was secured and fastened at both ends and a magnetic stirrer attached. The membrane was placed into a 5 L beaker with approximately 4.5 L of 15 MΩ distilled water and stirred by placing on a magnetic stirrer plate. The water was recharged daily for 4 days. Upon completion of dialysis, the membrane was removed and its contents placed in a beaker whereby the precipitate was removed from the majority of the solvent using a strong magnet. The product was placed in a -80^0C freezer overnight, frozen and put under a high vacuum to remove the remaining solvent. This freeze drying process took between 2-3 days and left a dry, fine black powder which still displayed magnetism characteristics when in a magnetic field. This separation technique, although time consuming, is more intensive and effective. Drying the particles was initially attempted but this left the particles with excess free reactants, which not only affected the mass of the powder, and thus makes concentration calculations inaccurate, but also meant that the particles were still at high pH values when resuspended.

The powder could be resuspended in water with the assistance of sonication in an ultrasonic water bath for approximately 30 minutes. The pH of the resultant solution at a concentration of 50 mg/ml and at room temperature was 5.38.

4.4. Antimicrobial Testing of Tiopronin Stabilised Iron Oxide

4.4.1. Hyperthermia System

The magnetic AC hyperthermia (MACH) system was powered by 150 Volts at ca. 0.8 Amps. This system has been built in-house and encompasses a 2 cm water-cooled coil with 6 windings and provided a field of around 12 kA/m at a frequency of 1.05 MHz. The sample was placed in the centre of the coil. See Chapter 2 for a picture of the apparatus set up, the image shows a 3 turn solenoid, however as described a 6 turn solenoid of 2 cm diameter was used.

.

4.4.2. Bacterial Stains

The organism used in this investigation was *Staphylococcus aureus* NCTC 6571. It was maintained as a plate culture and subcultured weekly from freezer stocks on Nutrient Agar (Oxoid Ltd, Basingstoke, UK). For experimental purposes, a single colony was inoculated into Nutrient Broth No. 2 (Oxoid) and grown aerobically for 16 h at 37ºC with shaking. Cells were harvested by centrifugation and resuspended in sterile phosphate buffered saline (PBS) to an OD_{600nm} of 0.05. In some experiments, the adjusted bacterial suspensions were further diluted 1 in 10 and 1 in 100 in PBS.

4.4.3. Magnetic Nanoparticles

The magnetic nanoparticles used were codified as $SPION_{Tiopronin}$ (iron oxide formed in the presence of tiopronin) and $SPION_{Succinic}$ (iron oxide formed in the presence of succinic acid). Dilutions were made in PBS to obtain the desired concentration. $SPION_{Oxamic}$ (iron oxide formed in the presence of oxamic acid) was not used due to the low pH that formed on dissolution.

4.4.4. Bacterial Magnetic Hyperthermia

Aliquots (200 μL) of a suspension of *S. aureus* NCTC 6571 in sterile PBS, were placed into an Eppendorf tube. To the same tube, 200 μL of magnetic nanoparticles were added. Samples were vortexed and then exposed to the hyperthermia heater for the desired amount of time. The air flow machine was set to ~37°C to maintain a constant temperature. The temperature of each tube was recorded using a Luxtron Fibre Optic Temperature measurement system (LumaSense™ Technologies, CA, USA). Control tubes contained PBS in place of magnetic nanoparticles and were exposed to the same conditions. Control tubes containing either PBS or magnetic nanoparticles and the bacterial suspension, were not exposed to the hyperthermia heater. Following exposure to the machine, 25 μL aliquots of the test and control samples were taken and added to 225 μL PBS. Serial dilutions were made, and 20 μL aliquots (in duplicate) from each dilution were plated on to Nutrient agar, and grown overnight at 37ºC to enumerate survivors. This work was carried out at the Eastman Dental Institute.

4.5. Results

4.5.1. Characterisation

Analysis of iron oxide nanoparticles formed in the presence of carboxylic acid functionalised ligands via a coprecipitation method was carried out using X-Ray

diffraction (XRD) on a Bruker DX8 using CuK_{α} radiation, 1.54 Å; Raman using a Renishaw inVia Raman Microscope with a laser wavelength of 785 nm and power of 1%; Infrared (IR) spectroscopy using a Perkin Elmer FT-IR Spectrometer Spectrum RX1; Thermogravimmetric analysis (TGA) using a Netzsh STA 449C instrument with Helium gas; Magnetometry on a quantum design magnetic property measurement system (MPMS)-5T and photon correlation spectroscopy (PCS) on a Zetasizer 3000 (Malvern, UK) was used to measure the hydrodynamic diameter of the nanoparticles in a plastic cuvette in distilled water at 25°C.

XRD was run for all samples and, in all cases, confirmed a core composition of iron oxide in both magnetite and maghemite forms (Figures 4-2, 4-10, 4-16 and 4-21). The crystallite sizes for the samples were estimated using the Scherrer equation and peak broadening was taken into account using a Gaussian fit. The comparison was made to a LaB_6 standard.

4.5.2. Tiopronin

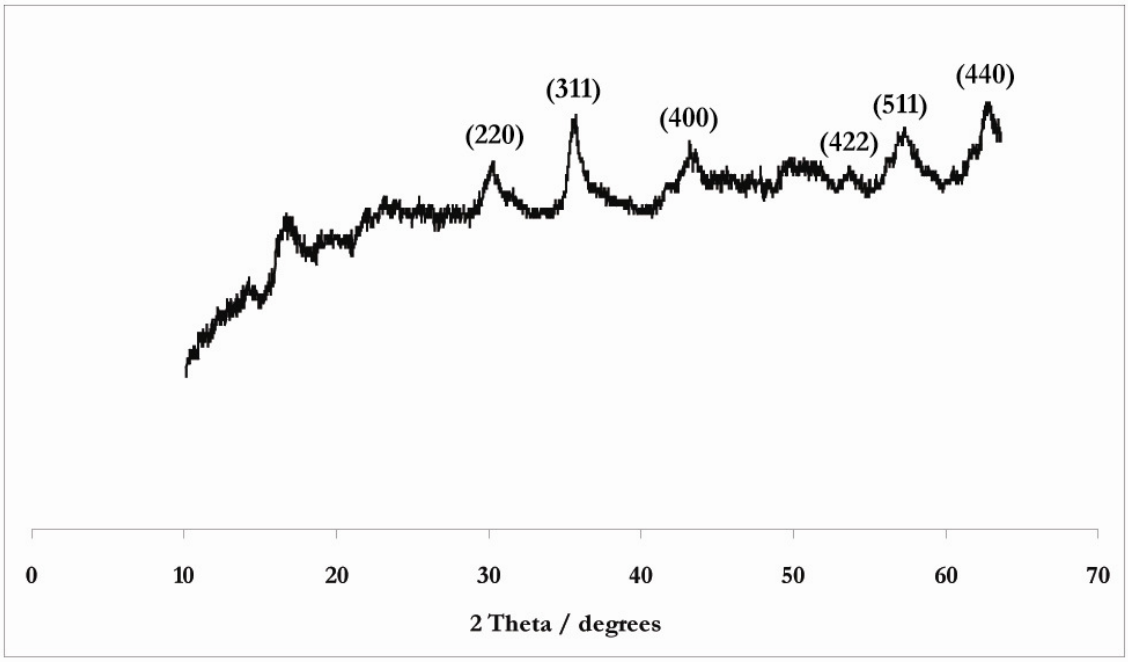

Figure 4-2 XRD pattern of iron oxide nanoparticles synthesised in the presence of tiopronin at 70°C *via* a coprecipitation method.

The tiopronin coated sample was identified as having a magnetite and maghemite composition as identified in the XRD pattern (Figure 4-2).[184, 185] This composition is also confirmed in the Raman spectra (Figure 4-3) where there are both magnetite and maghemite shifts.[186-188] The XRD peaks are broad indicating the small nanoparticulate nature of the core. The crystallite size was estimated to be 9.4 nm, using measurements of the full width half maximum of the peak at 35.69^0. The hydrodynamic size of the particles when suspended in distilled water was 135.2 nm with a polydispersity index of 0.265.

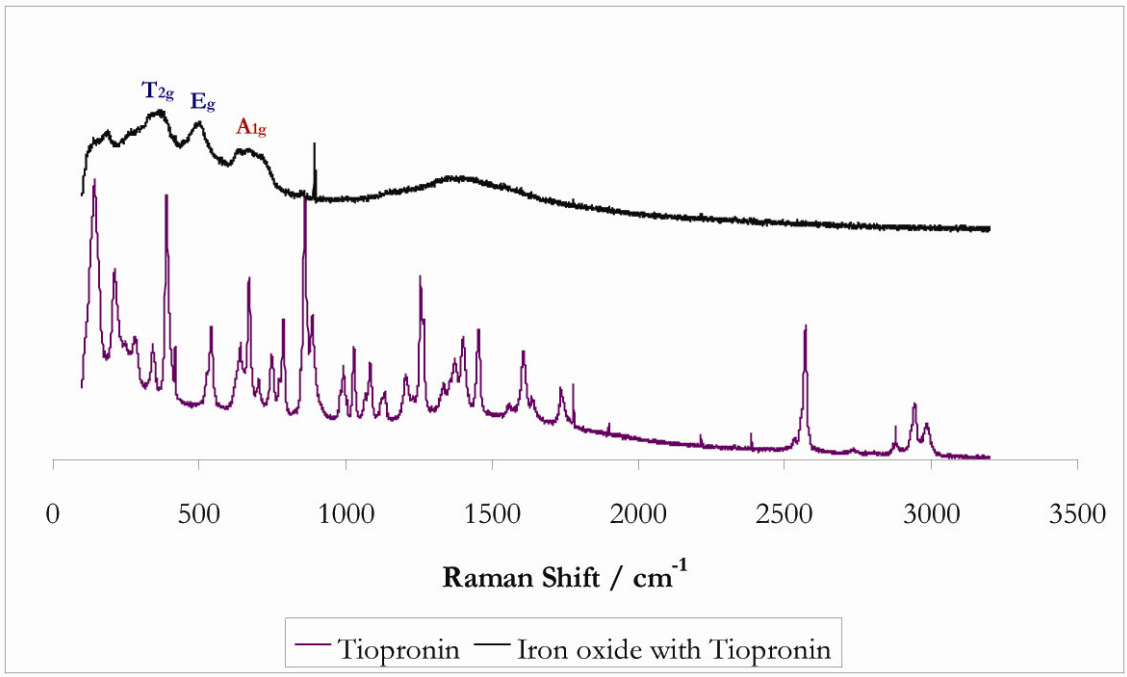

Figure 4-3 The Raman spectra of both free tiopronin and iron oxide synthesised in the presence of tiopronin *via* a coprecipitation method. Raman shifts are coloured blue for maghemite and coloured red for magnetite.

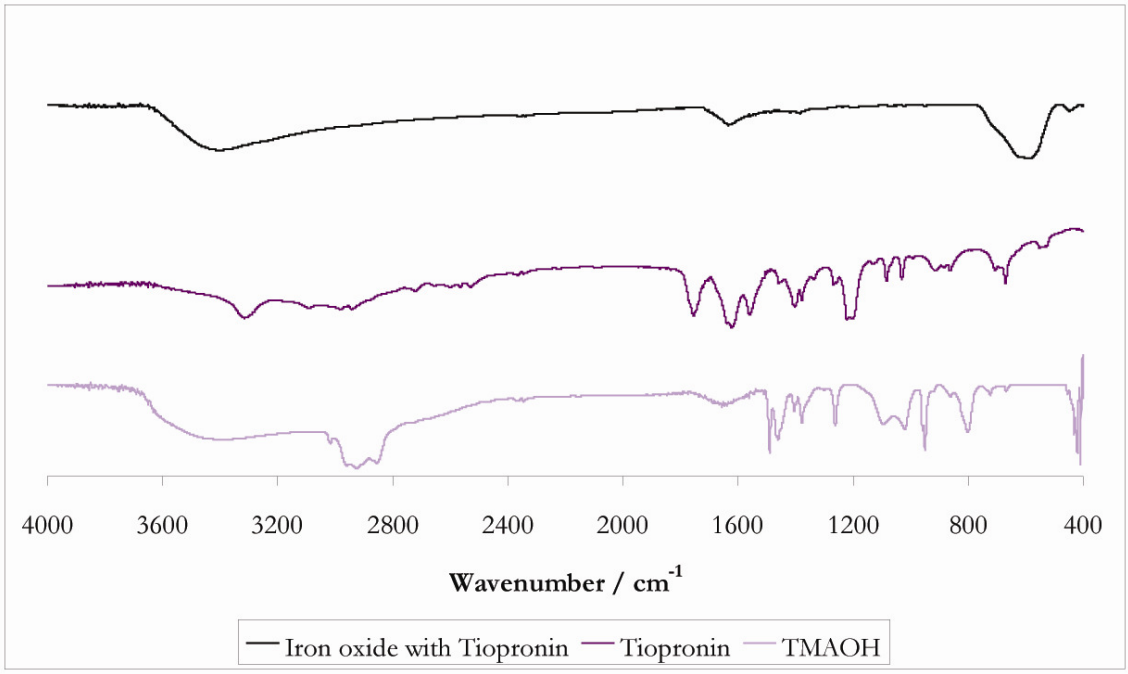

Figure 4-4 FTIR spectra of free tetramethylammonium hydroxide (TMAOH), free tiopronin and iron oxide formed in the presence of tiopronin using TMAOH as a reducing agent.

Figure 4-4 shows the FTIR spectrum for the tiopronin coated nanoparticles, free tiopronin and free tetramethylammonium hydroxide. The spectrum confirms the presence of Fe-O stretches at both the octahedral and tetrahedral sites. These can be seen in the large peaks around 580 and 620 cm^{-1}.

The elemental analysis confirmed the presence of carbon (1.54%), hydrogen (0.34%) and nitrogen (0.2%). TGA was run in an inert atmosphere to try to correlate these values and there is tentative evidence to suggest that these values correlated to the first mass loss between 0-180^{0}C (Figure 4-5). The TGA residual mass is 89% of the total, this is likely to be the remaining inorganic nanoparticle core.

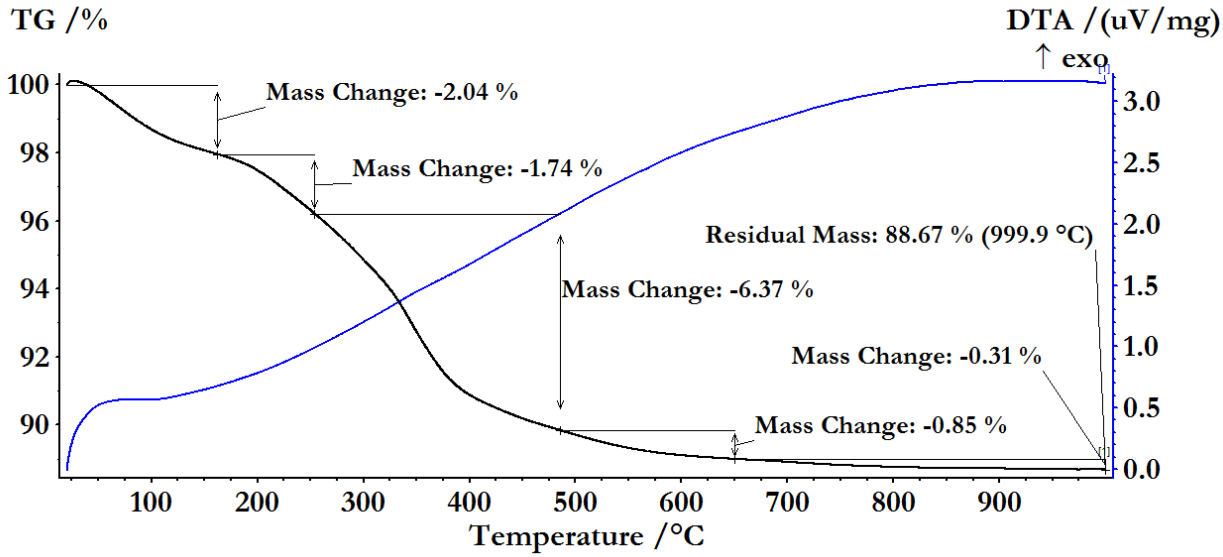

Figure 4-5 TGA of iron oxide nanoparticles formed in the presence of tiopronin *via* a coprecipitation method. The mass changes and residual mass at 1000^{0}C is indicated on the graph.

Figure 4-6 is the SQUID magnetometry data for the tiopronin coated iron oxide nanoparticles. The sample is superparamagnetic due to the zero coercivity seen at 300 K, when compared to the coercivity when the measurements are run at 10 K. The zero field cooling (ZFC) and field cooling (FC) curves are also shown in Figure 4-6. M_s is 49 emu g^{-1} at 300 K.

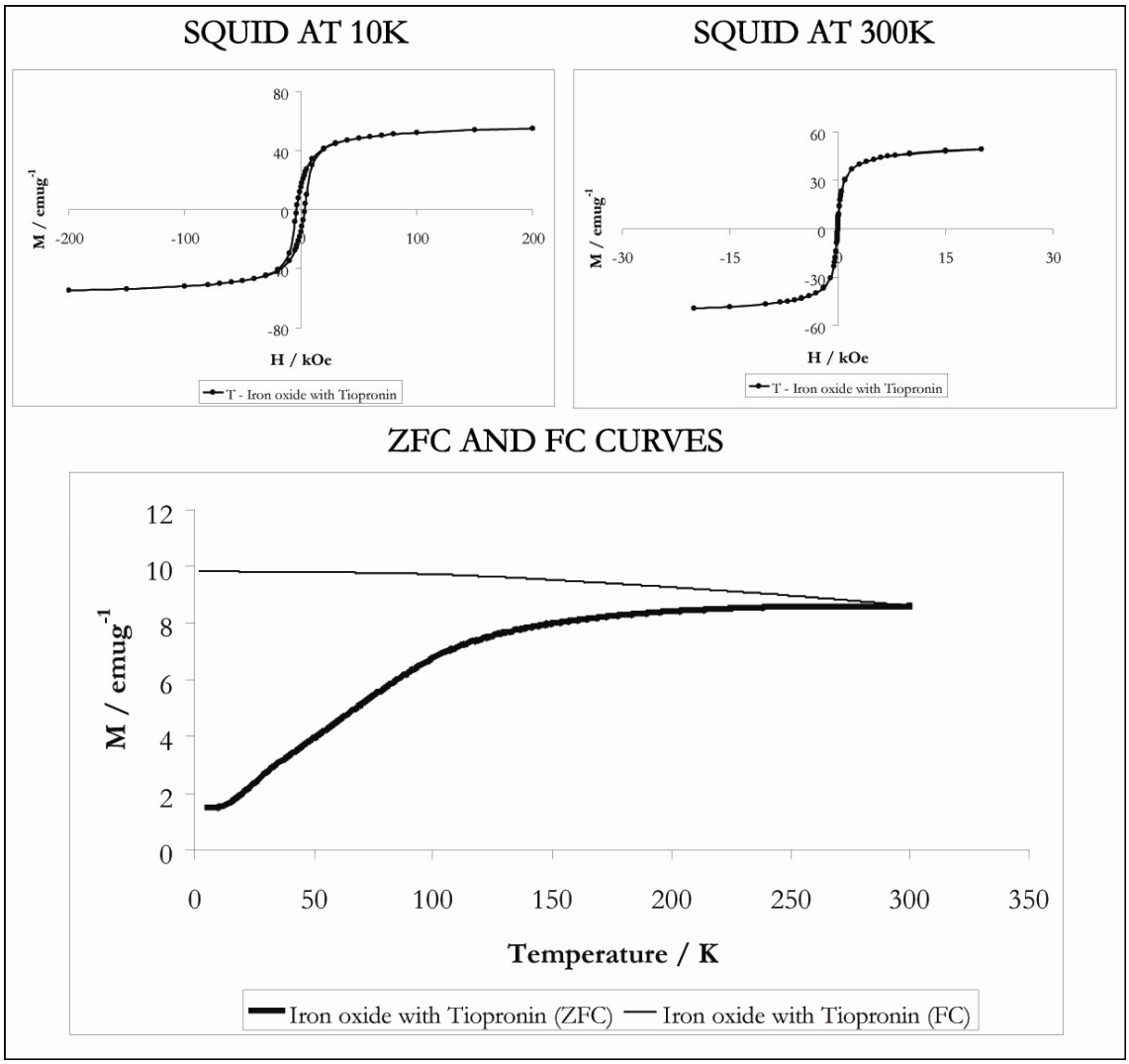

Figure 4-6 SQUID data collected for iron oxide nanoparticles synthesised using a coprecipitation method in the presence of tiopronin. The two M-H diagrams are at 10 K and 300 K. The bottom graph is the zero field and field cooled (ZFC and FC) data collected.

The $SPION_{Tiopronin}$ was at a suitable pH for biomedical applications so was subjected to heat testing in the MACH machine. This sample produced an outstanding heating curve (Figure 4-7). This was compared to the best commercially available particles for magnetic hyperthermia; Bayer Schering's Resovist and Micromod's Nanomag 100 at equivilant concentrations. Figure 4-8 shows these results by comparing both the specific absorption rate (SAR) and intrinsic loss power (ILP).

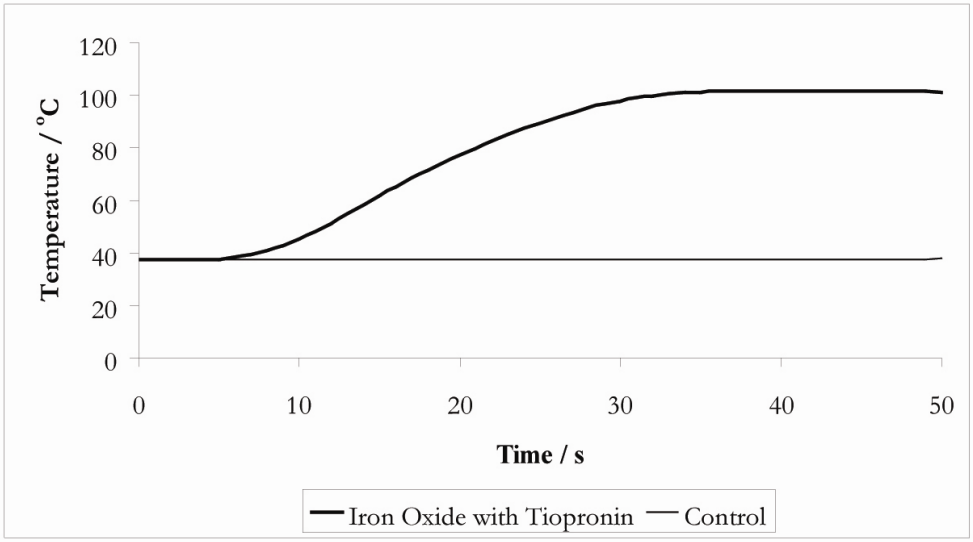

Figure 4-7 The temperature of a 50 mg/ml solution of an iron oxide nanoparticle solution synthesised in a coprecipitation method with tiopronin. Due to water boiling the maximum temperature reached is 100^{0}C.

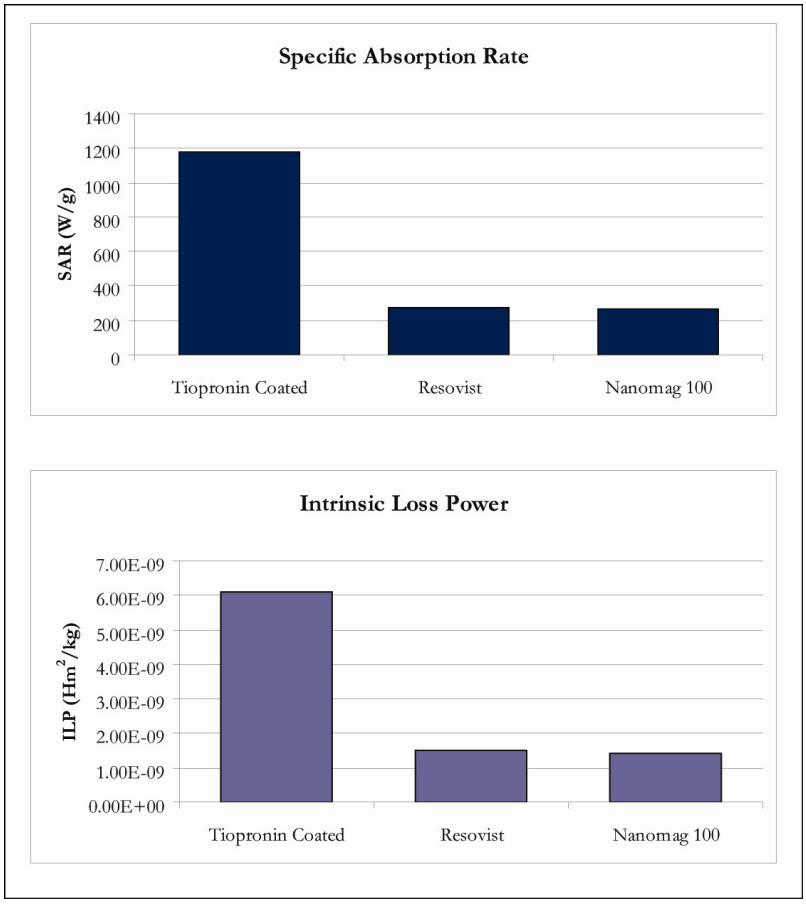

Figure 4-8 A comparison of both the specific absorption rate (SAR) and the intrinsic loss power (ILP) of iron oxide nanoparticles synthesised in a coprecipitation method in the presence of tiopronin, against commercially available iron oxide nanoparticles named Resovist and Nanomag 100.

Figure 4-9 is an illustration of the magnetic strength of the $SPION_{Tiopronin}$ ferrofluid, it is suspended in a 50 ml centrifuge tube from a rare earth magnet.

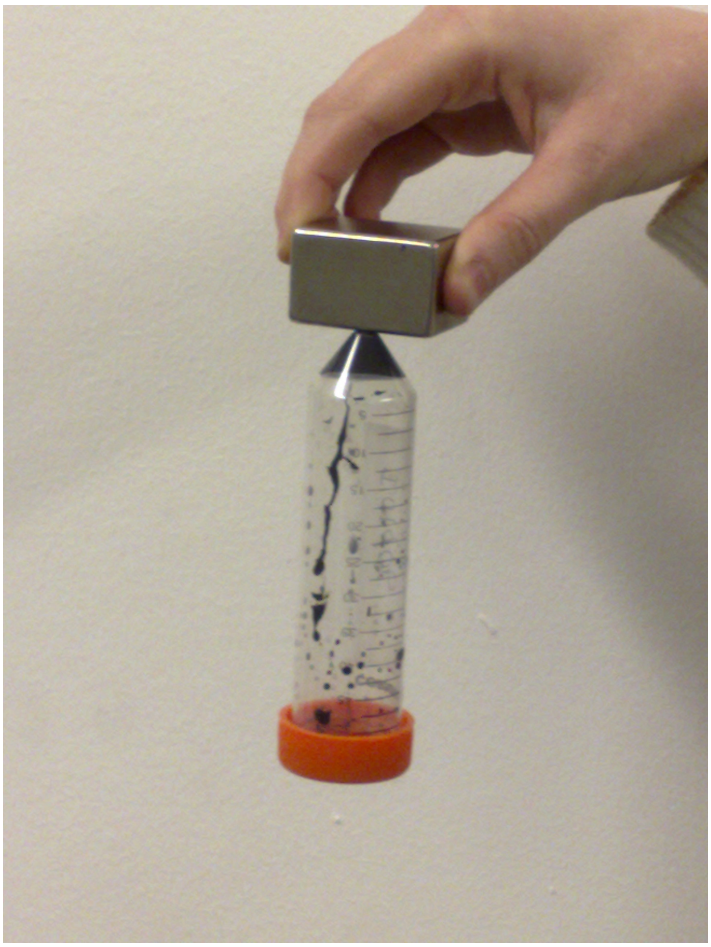

Figure 4-9 Iron oxide nanoparticle ferrofluid synthesised in the presence of Tiopronin *via* a coprecipitation synthesis at 70^{0}C, suspended in 1 50 ml centrifuge tube from a NdFeB rare earth magnet.

4.5.3. Succinic Acid

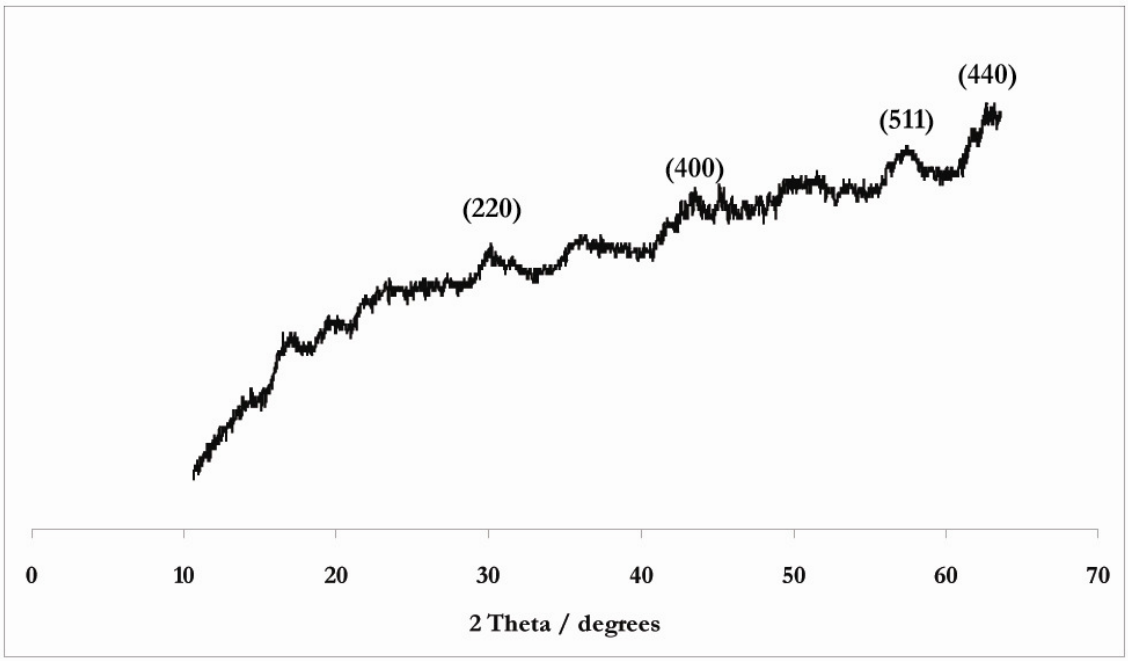

Figure 4-10 XRD pattern of iron oxide nanoparticles synthesised in the presence of succinic acid at 70^{0}C *via* a coprecipitation method.

The succinic acid coated sample was identified as having a magnetite and maghemite composition as identified in the XRD pattern (Figure 4-10).[184, 185] This composition was also confirmed in the Raman spectra where there are vibrations assignable to both magnetite and maghemite (Figure 4-11).[187, 188] The XRD peaks are broad indicating the small nanoparticulate nature of the core. The powder was coarse making the XRD difficult to focus. The crystallite size was estimated using the Scherrer equation, as per the tiopronin coated sample. The average crystallite size was calculated to be approximately 7 nm. The full width half maximum was measured using peak 35.75^0. The hydrodynamic size of the particles when suspended in distilled water was 317 nm with a polydispersity index of 0.33.

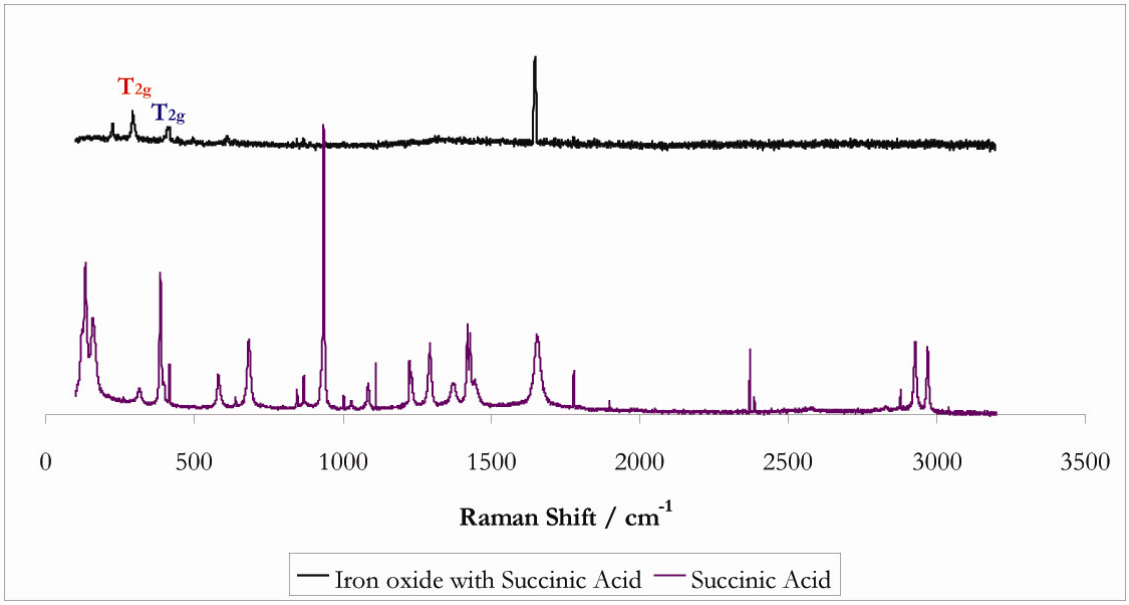

Figure 4-11 The Raman spectra of both free succinic acid and iron oxide synthesised in the presence of succinic acid *via* a coprecipitation method. Raman shifts are coloured blue for maghemite and coloured red for magnetite.

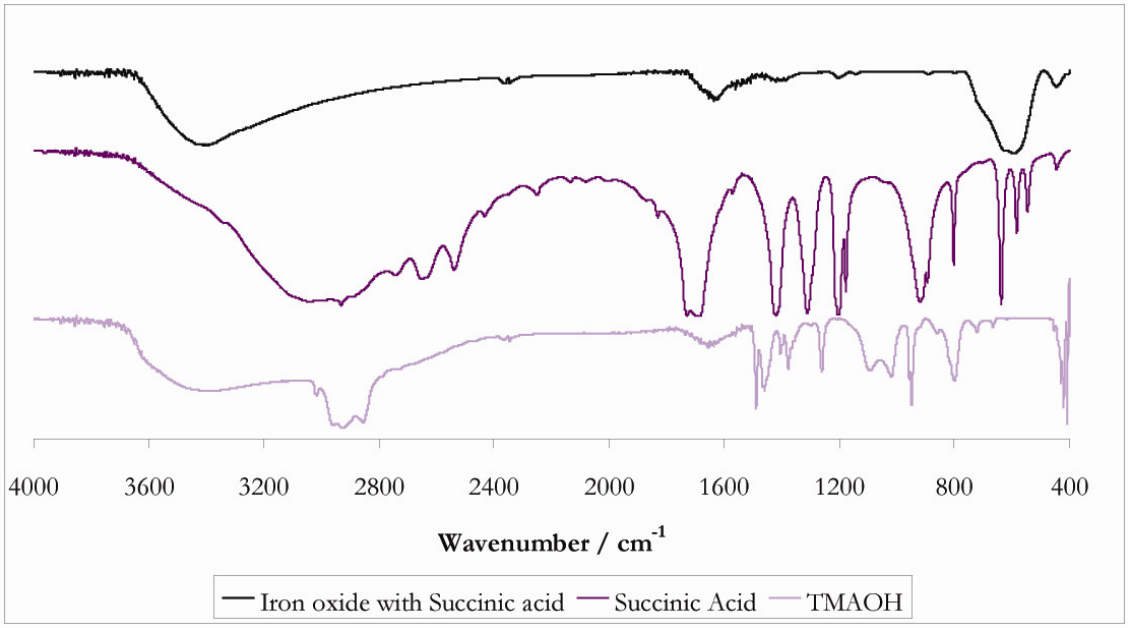

Figure 4-12 FTIR spectra of free tetramethylammonium hydroxide (TMAOH), free succinic acid and iron oxide formed in the presence of succinic acid using TMAOH as a reducing agent.

Figure 4-12 shows the FTIR spectrum for the succinic acid coated nanoparticles, free succinic acid and free Tetramethylammonium hydroxide. The spectrum confirms the presence of Fe-O stretches at both the octahedral and tetrahedral sites. These can be seen in the large peaks around 580 and 620 cm^{-1}.

The elemental analysis identified carbon (0.66%), hydrogen (0.52%) and nitrogen (0.62%). TGA was run to try to correlate these values but there was no clear match (Figure 4-13). The final mass loss around 450^{0}C is likely to be the phase transition from maghemite to hematite. This phase transition is irreversible. The data indicates that 90% of the mass is the inorganic component.

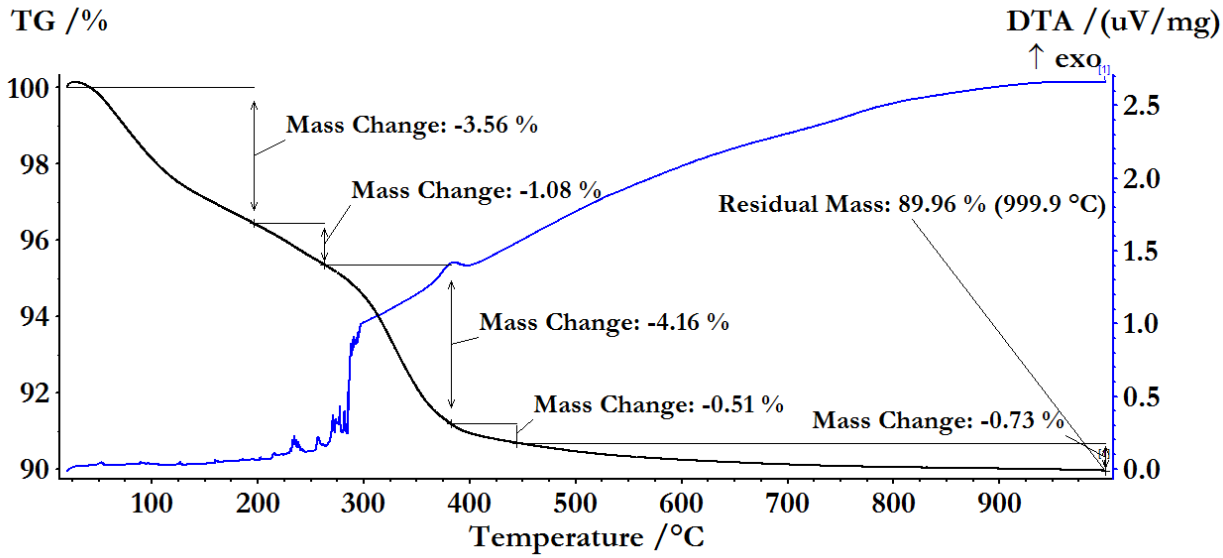

Figure 4-13 TGA of iron oxide nanoparticles formed in the presence of succinic acid *via* a coprecipitation method. The mass changes and residual mass at 1000^{0}C is indicated on the graph.

Figure 4-14 is the SQUID magnetometry data for the succinic acid coated iron oxide nanoparticles. The sample is superparamagnetic; this is known because below the blocking temperature there is coercivity, as seen in the 10 K data, and above the blocking temperature there is zero and the plot at 300 K looks paramagnetic. The zero field cooling (ZFC) and field cooling (FC) curves are shown in Figure 4-14. M_s for $SPION_{Succinic}$ at 300 K is 49 emu g^{-1}.

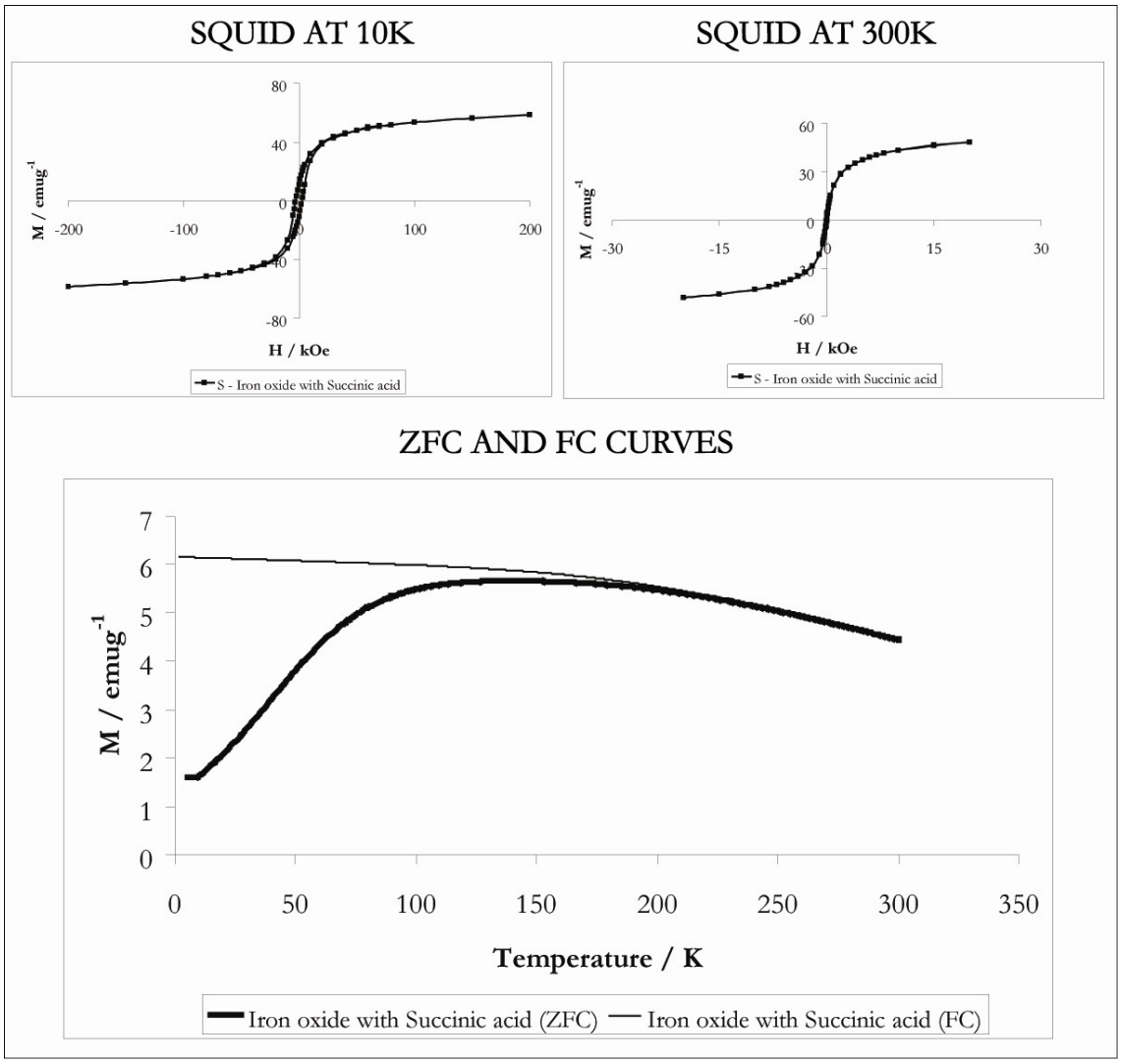

Figure 4-14 SQUID data collected for iron oxide nanoparticles synthesised using a coprecipitation method in the presence of succinic acid. The two M-H diagrams are at 10 K and 300 K. The bottom graph is the zero field and field cooled (ZFC and FC) data collected.

The $SPION_{Succinic}$ sample was at a suitable pH for biomedical applications so was subjected to heat testing in the MACH machine (Figure 4-15). The sample did not respond well to the field and was far less efficient than the tiopronin coated sample. Due to this, no further cell or bacterial tests were carried out on this sample.

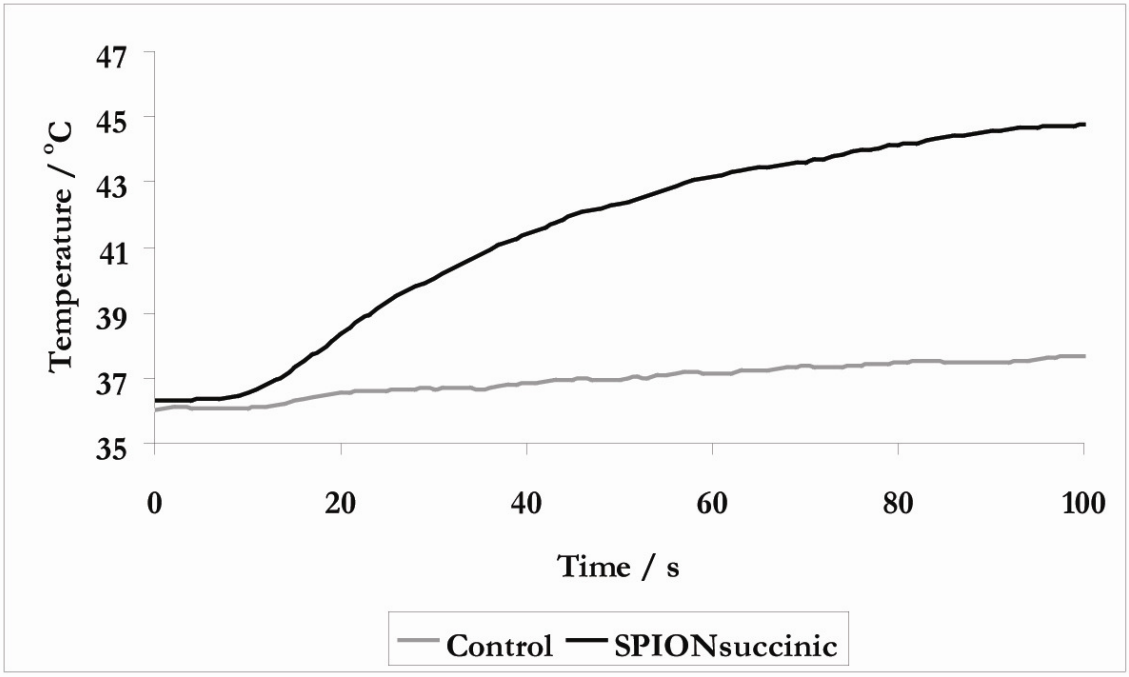

Figure 4-15 The heating response from the iron oxide nanoparticles synthesised by a coprecipitation method with the presence of succinic acid ($SPION_{succinic}$) when placed in an inductive magnetic field (MACH).

4.5.4. Oxamic Acid

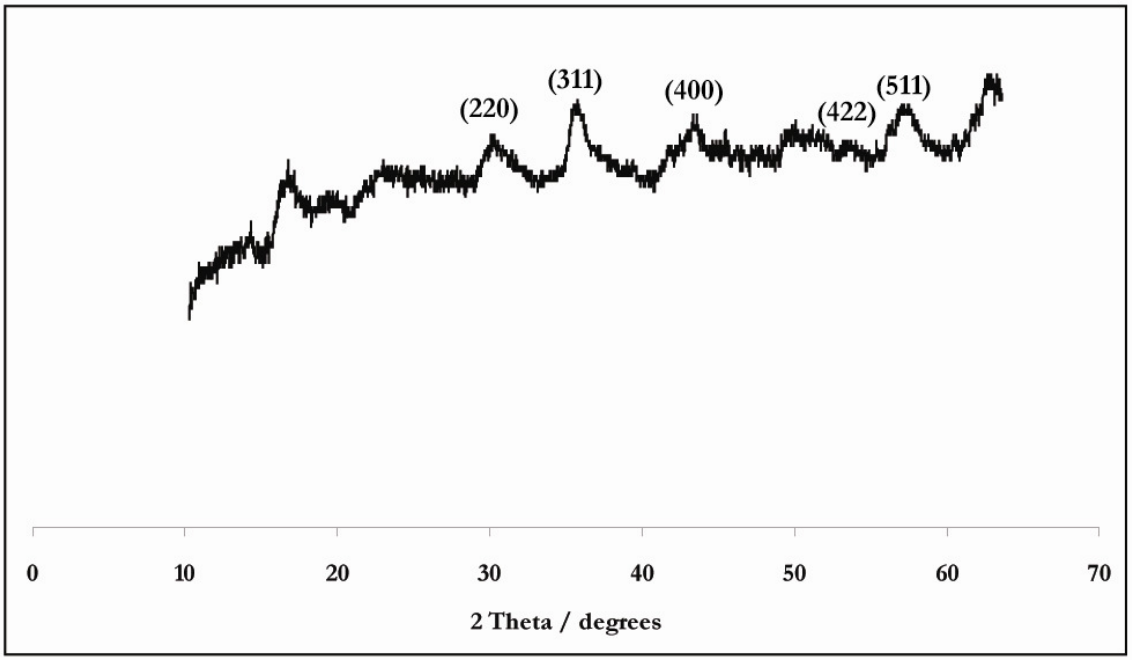

Figure 4-16 XRD pattern of iron oxide nanoparticles synthesised in the presence of oxamic acid at 700C via a coprecipitation method.

The XRD and Raman spectra of $SPION_{Oxamic}$ shows there are assignable vibrations to both magnetite and maghemite (Figures 4-16 and 4-17).[184, 185, 187, 188] The crystallite size was estimated to be 7.9 nm based on the full width half maximum measurement of peak 35.75^0. The hydrodynamic size of the particles when suspended in distilled water was 870 nm with a polydispersity index of 0.40.

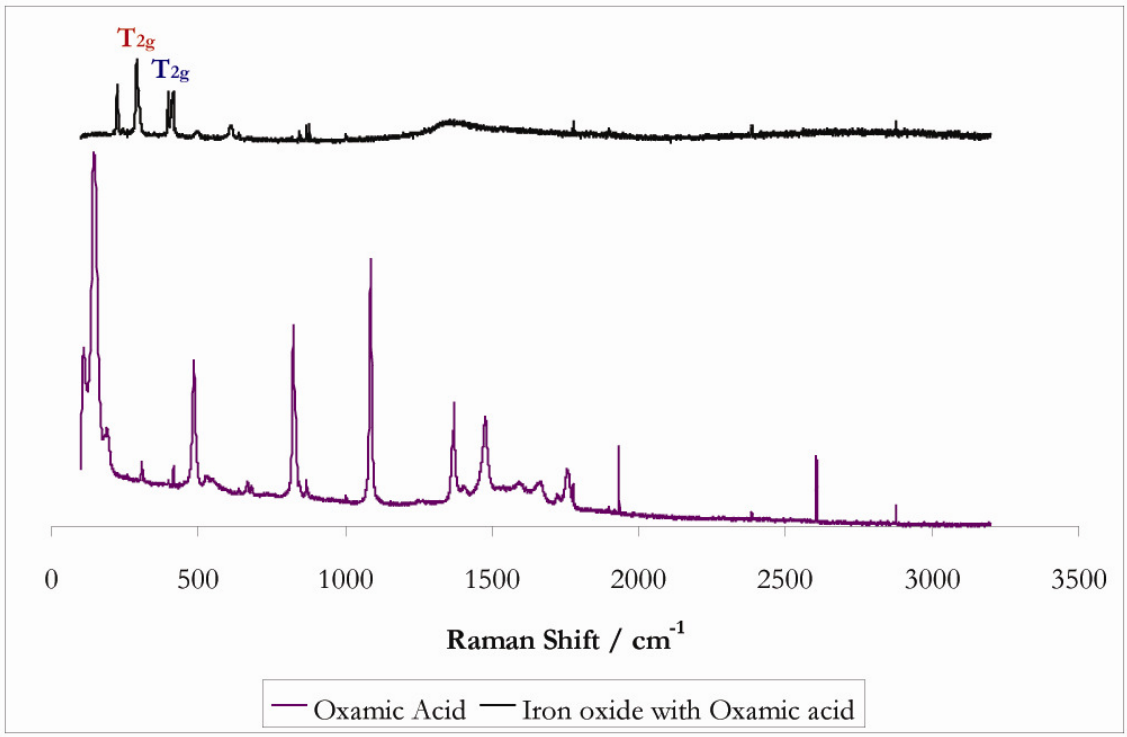

Figure 4-17 The Raman spectra of both free oxamic acid and iron oxide synthesised in the presence of oxamic acid *via* a coprecipitation method. Raman shifts are coloured blue for maghemite and coloured red for magnetite.

Figure 4-18 shows the FTIR spectrum for the $SPION_{Oxamic}$, free oxamic acid and free Tetramethylammonium hydroxide. The spectrum confirms the presence of Fe-O stretches at both the octahedral and tetrahedral sites; around 580 and 620 cm^{-1}.

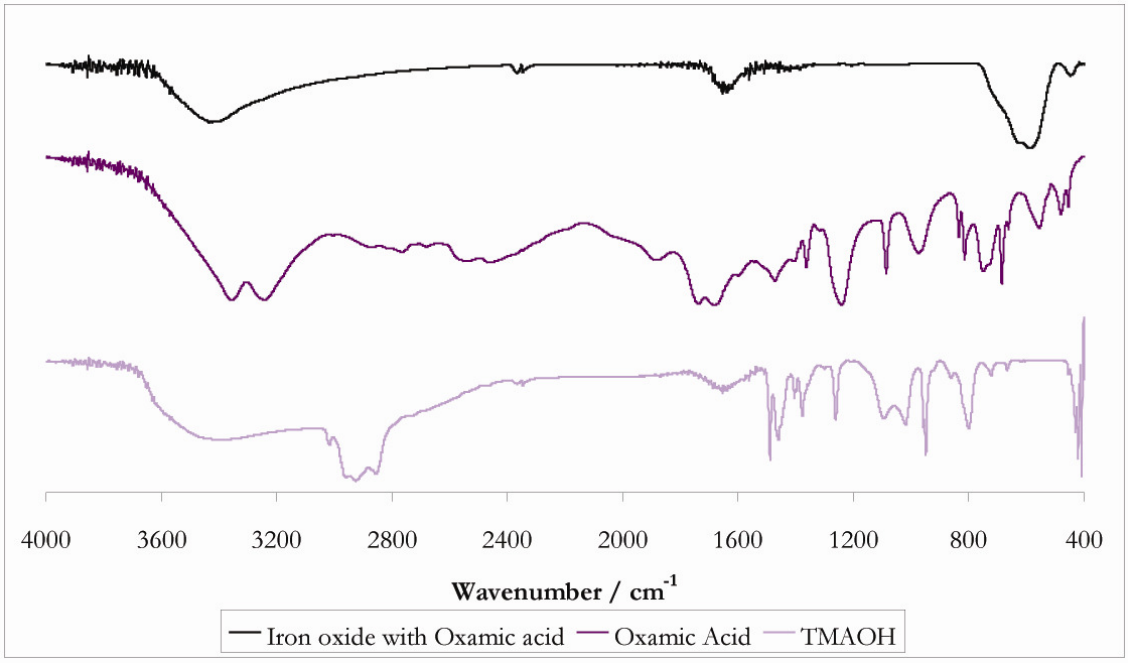

Figure 4-18 FTIR spectra of free tetramethylammonium hydroxide (TMAOH), free oxamic acid and iron oxide formed in the presence of oxamic acid using TMAOH as a reducing agent.

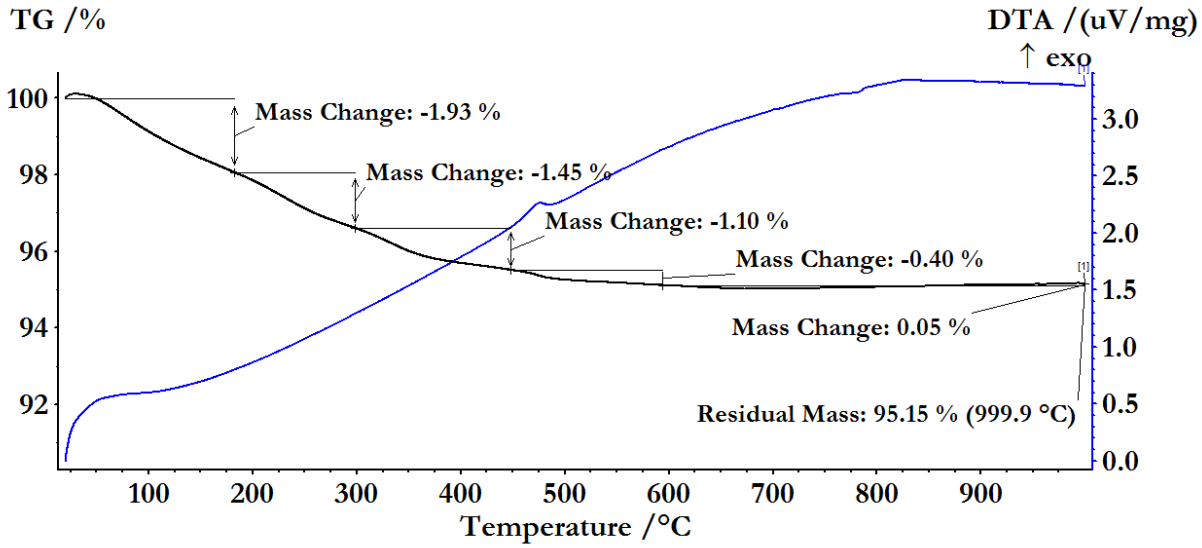

Figure 4-19 TGA of iron oxide nanoparticles formed in the presence of oxamic acid *via* a coprecipitation method. The mass changes and residual mass at 1000^{0}C is indicated on the graph.

The elemental analysis identified carbon (0.38%), hydrogen (0.32%) and nitrogen (0.01%). TGA was run to try to correlate these values and there is tentative evidence to suggest that this correlates to the mass loss between 0-175^{0}C (Figure 4-19). 95% of the mass remains, most probably being the iron oxide core.

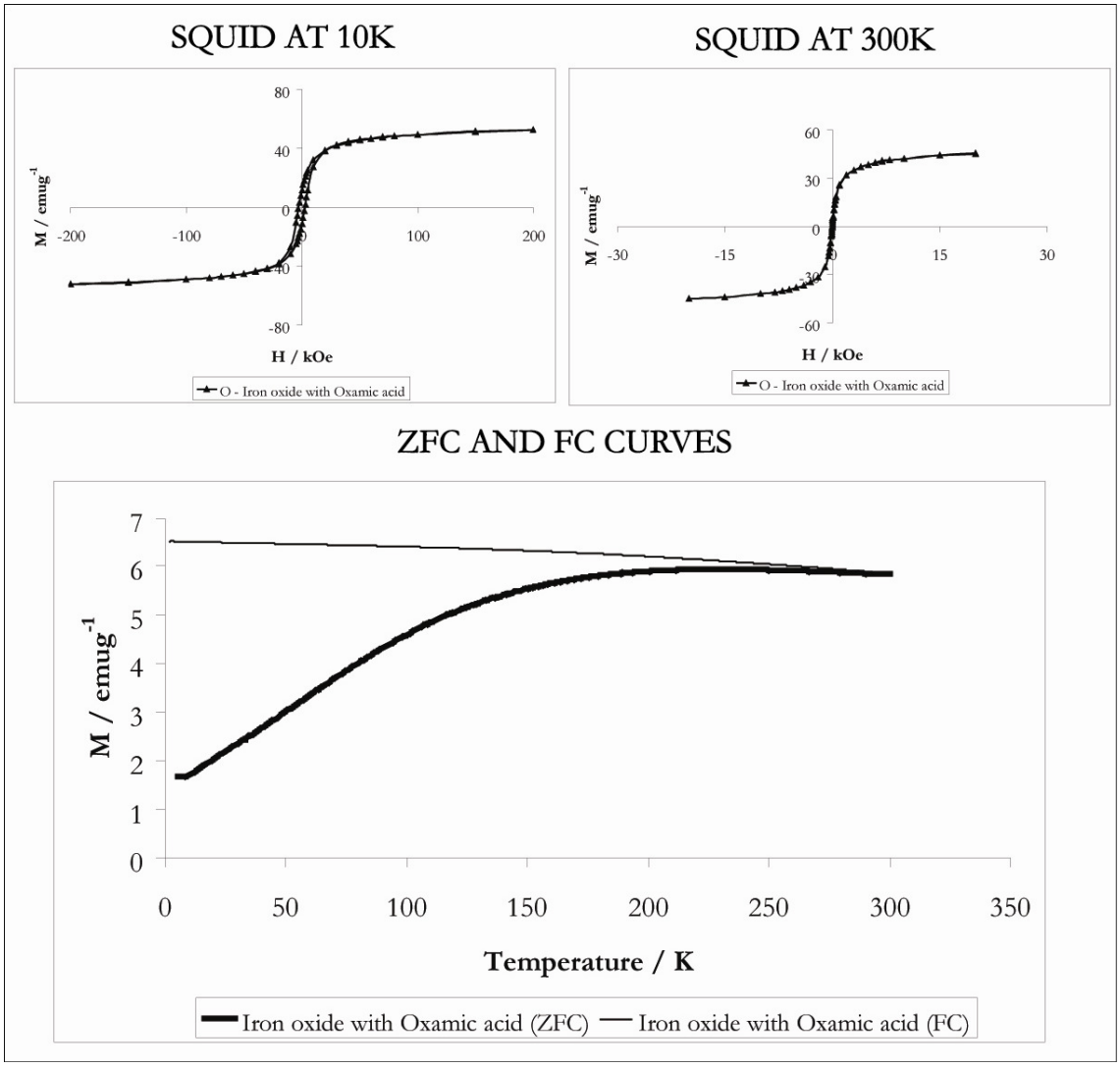

Figure 4-20 SQUID data collected for iron oxide nanoparticles synthesised using a coprecipitation method in the presence of oxamic acid. The two M-H diagrams are at 10 K and 300 K. The bottom graph is the zero field and field cooled (ZFC and FC) data collected.

Figure 4-20 is the SQUID magnetometry data for the oxamic acid coated iron oxide nanoparticles. The sample is superparamagnetic; this is known because below the blocking temperature there is coercivity, as seen in the 10 K data, and above the

blocking temperature there is zero and the plot at 300 K looks paramagnetic. The zero field cooling (ZFC) and field cooling (FC) curves are shown in Figure 4-20. M_s is 45 emu g^{-1} at 300 K.

The $SPION_{Oxamic}$ was not at a suitable pH for biomedical applications so no heating data was collected.

4.5.5. EDTA

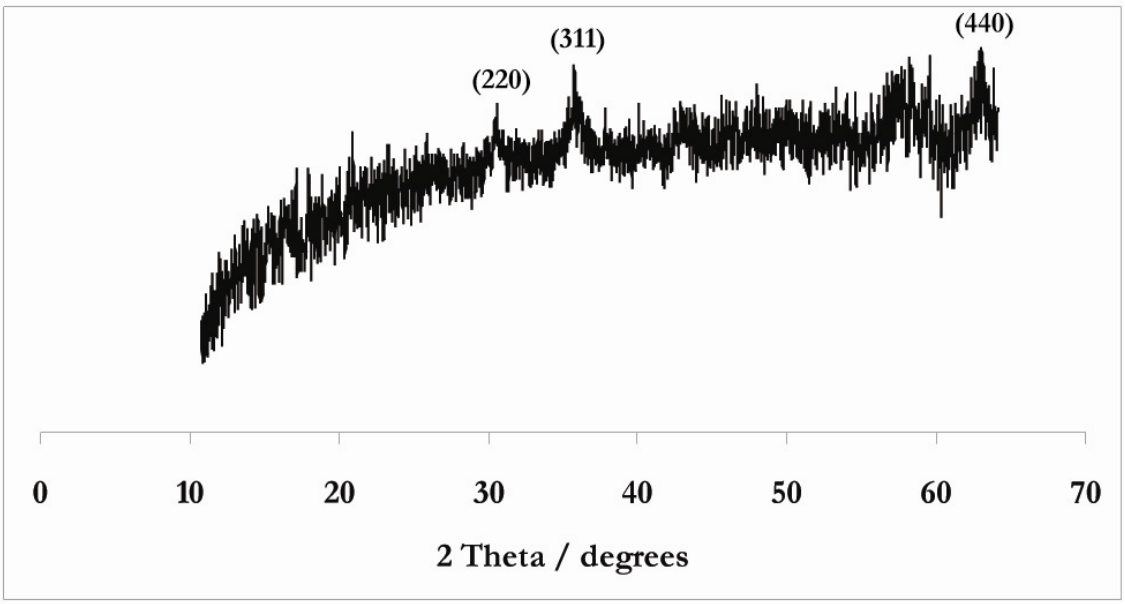

Figure 4-21 XRD pattern of iron oxide nanoparticles synthesised in the presence of EDTA at 70^{0}C *via* a coprecipitation method.

As before, using the Scherrer equation the crystallite size was estimated to be 16.4 nm for the $SPION_{EDTA}$ sample. This was measured using the full width half maximum measurements of the peak at 35.75^0 on the XRD pattern (Figure 4-21). The XRD showed the sample was a mix of magnetite and maghemite.[184, 185] The Raman peaks (Figure 4-22), again show that the nanoparticle is comprised of both magnetite and maghemite.[187, 188] The hydrodynamic size measurements for $SPION_{EDTA}$ dissolved in distilled water at room temperature was 378 nm with a PDI of 0.18.

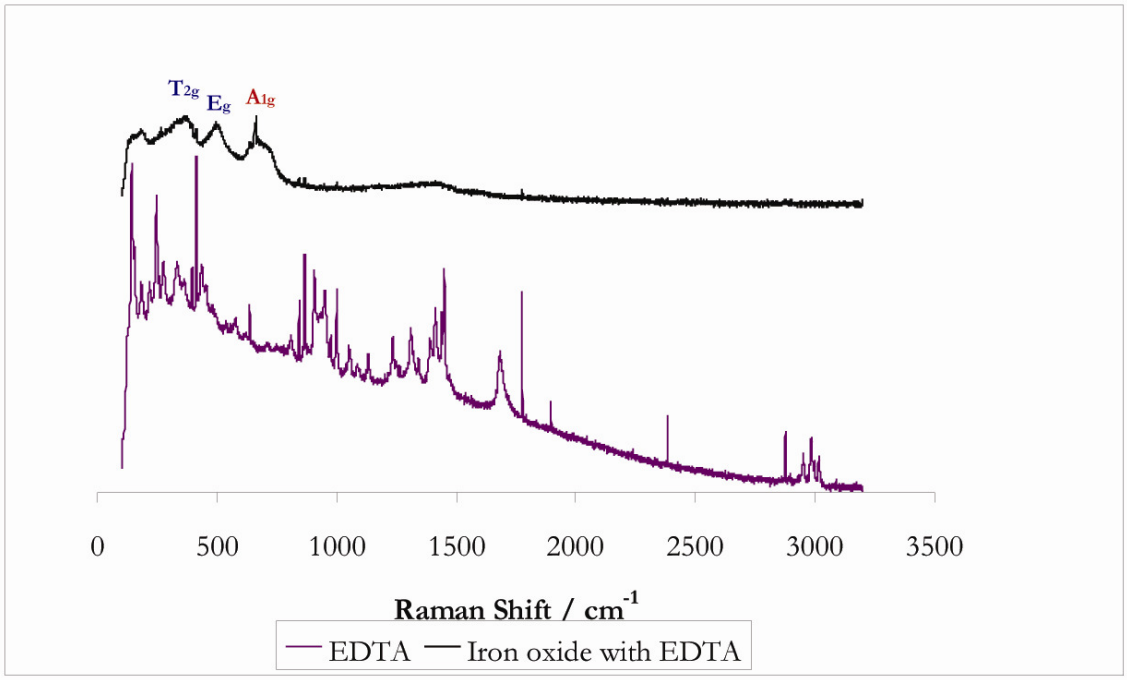

Figure 4-22 The Raman spectra of both free EDTA and iron oxide synthesised in the presence of EDTA *via* a coprecipitation method. Raman shifts are coloured blue for maghemite and coloured red for magnetite.

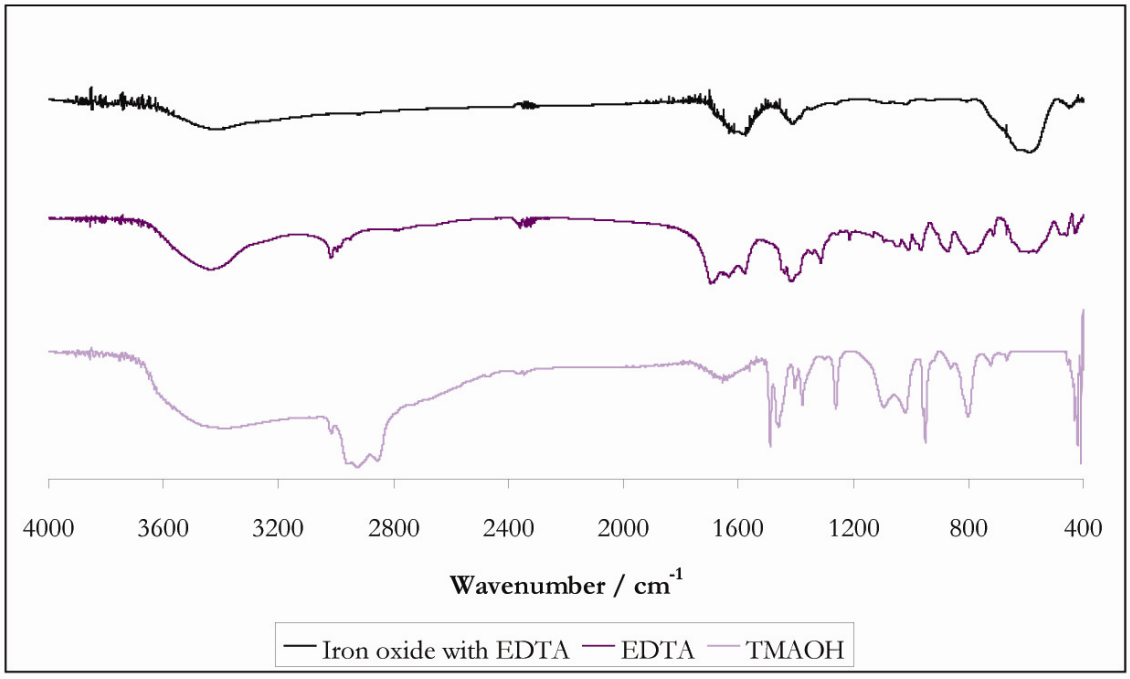

Figure 4-23 FTIR spectra of free tetramethylammonium hydroxide (TMAOH), free EDTA and iron oxide formed in the presence of EDTA using TMAOH as a reducing agent.

Figure 4-23 shows the FTIR spectrum for the EDTA coated nanoparticles, free EDTA and free Tetramethylammonium hydroxide. The spectrum confirms the presence of Fe-O stretches at both the octahedral and tetrahedral sites.

Elemental analysis of the $SPION_{EDTA}$ sample showed gave carbon (1.17%), hydrogen (0.4%) and nitrogen (0.14%). Figure 4-24 shows the TGA for the sample, the mass loss between 0-190^{0}C is similar to the results of the elemental analysis. 96% of the mass remained.

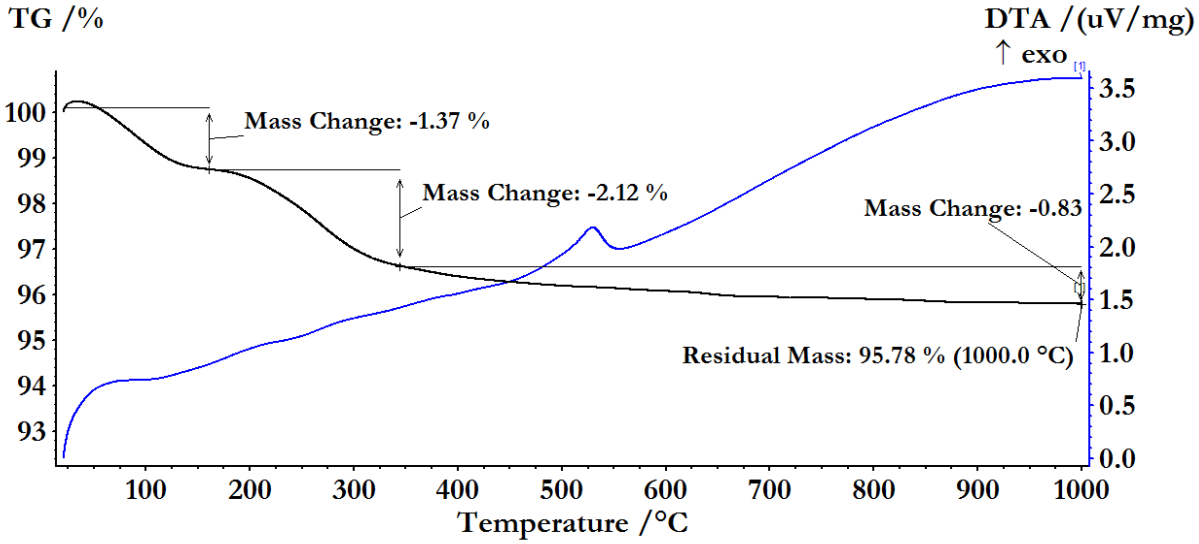

Figure 4-24 TGA of iron oxide nanoparticles formed in the presence of EDTA *via* a coprecipitation method. The mass changes and residual mass at 1000^{0}C is indicated on the graph.

Figure 4-25 is the SQUID magnetometry analysis of the $SPION_{EDTA}$ sample. The sample is superparamagnetic; this can be seen by the small coercivity at 10 K and the zero coercivity at 300 K above the blocking temperature. The zero field cooling (ZFC) and field cooling (FC) curves are also shown in Figure 4-25. M_s is 61.8 emu g^{-1} at 300 K.

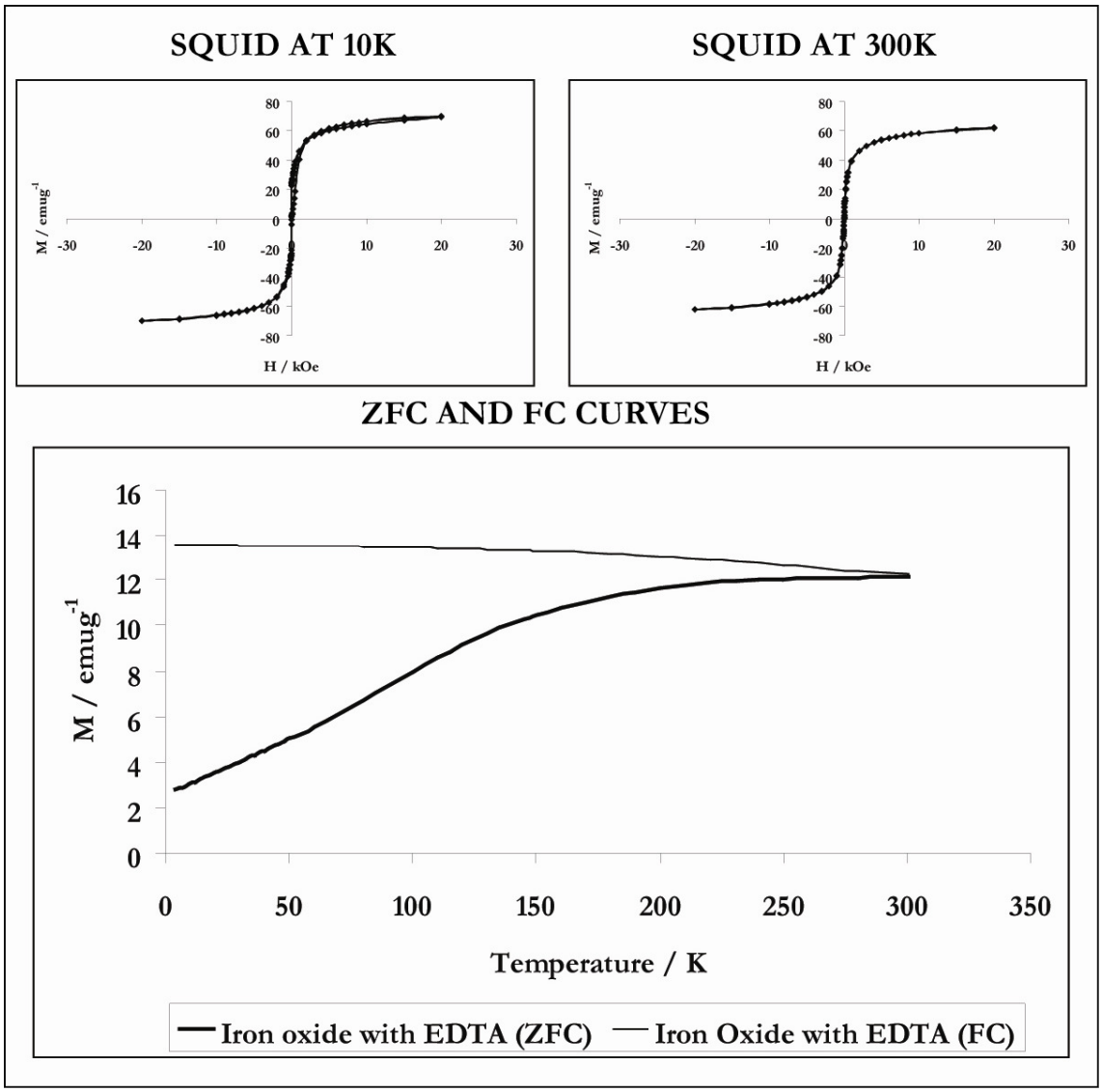

Figure 4-25 SQUID data collected for iron oxide nanoparticles synthesised using a coprecipitation method in the presence of EDTA. The two M-H diagrams are at 10 K and 300 K. The bottom graph is the zero field and field cooled (ZFC and FC) data collected.

The $SPION_{EDTA}$ was tested for heating efficiency in the MACH. It was largely unresponsive with a SAR value of 25.8 W/g and an ILP of 5.5 x 10^{-13} Hm^2/kg, cf. $SPION_{Tiopronin}$ which was several orders of magnitude greater. Thus, no further testing for antimicrobial properties was pursued.

4.5.6. The Antibacterial Activity of the Tiopronin Coated Sample

Due to the high ILP and SAR values from the $SPION_{Tiopronin}$ sample further investigation into the heating ability in an antibacterial capacity using a heat bath system was investigated in collaboration with the Eastman Dental Institute, London, UK. The bacterium chosen was *Staphylococcus aureus* NCTC 6571 and the heating response from $SPION_{Tiopronin}$ was induced using an inhouse patented system named MACH (see Chapter 2).

Initially the toxicity of the $SPION_{Tiopronin}$ was tested, in all control cases there were no bacterial deaths, confirming that the $SPION_{Tiopronin}$ is non toxic under normal conditions; when no magnetic field is present. The initial experiment used a $SPION_{Tiopronin}$ concentration of 50 mg/ml. The solution was exposed to the MACH and a total kill of 10^7 cfu/ml was recorded with a boiling reached within 30s. Following this positive result the antibacterial properties of the sample was investigated over time, varying concentrations and length and type of magnetic field exposure.

Six days after $SPION_{Tiopronin}$ preparation a 50 mg/ml concentration was studied under varying the length of time and type of exposure to the MACH. The variations were a continuous 2 minutes, continuous 1 minute, 3 exposures of 20 seconds and 6 exposures of 10 seconds. The results that show that with decreasing exposure time and decreasing continuous exposure the kills recorded are less can be seen in Figure 4-26.

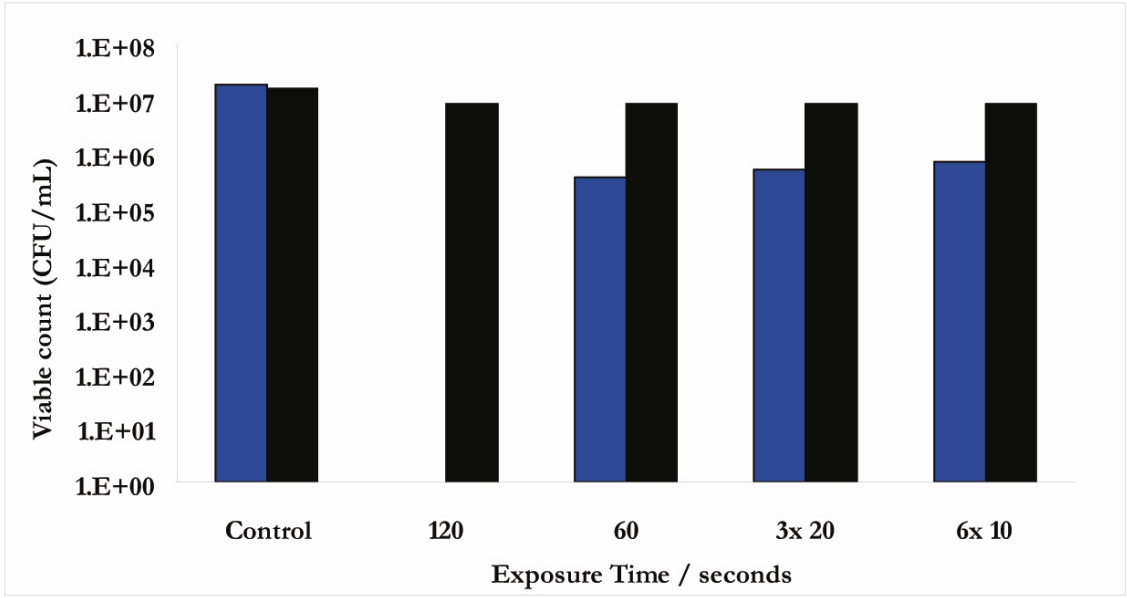

Figure 4-26 The bacterial count of *S.aureus* after exposure to iron oxide nanoparticles synthesised in a coprecipitation method in the presence of tiopronin, and at a concentration of 50 mg/ml in an inducing magnetic field. The field exposure time was varied to be continuous for 120s or 60s or to be pulsed for 3 x 20s and 6 x 10s. The experiment was run 6 days after SPION preparation.

Figure 4-27 shows the antibacterial study taken 7 days after $SPION_{Tiopronin}$ was prepared. Again, the 50 mg/ml conctration was recording total kills and the bath reached a maximum temperature of 100^0C (boiling). This maximum temperature was also found in the 25 mg/ml but the rate at which it reached this was slower; 6^0C per minute. The maximum bath heating temperatures and bacterial kills reduced with decreasing $SPION_{Tiopronin}$ concentration.

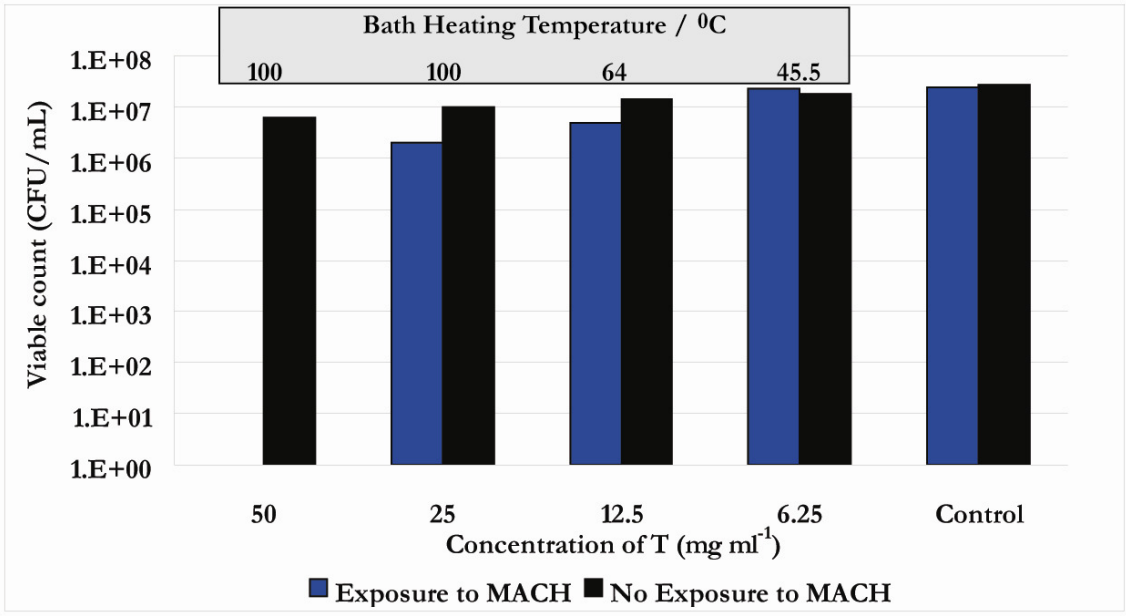

Figure 4-27 The bacterial count of *S.aureus* after exposure to iron oxide nanoparticles synthesised in a coprecipitation method in the presence of tiopronin (T) in an inducing magnetic field (MACH). The concentration of the nanoparticles was varied to be 50, 25, 12.5 and 6.25 mg/ml. In the case of the 50 mg/ml result, no blue bar shows that when exposed to the MACH there was a total kill of bacteria. The temperature that the water bath reached in each case due to the heat effect from the hyperthermic response of the particles is indicated above. The experiment was run 7 days after the particles had been prepared.

Figure 4-28 shows the results 19 days after $SPION_{Tiopronin}$ preparation. Both 25 mg/ml and 50 mg/ml concentrations were used in this investigation to see how sample aging affects the bacterial kill count. The *S.aureus* was as neat, diluted 1:10 with PBS and diluted 1:100 in PBS. The 50 mg/ml sample consistently gave a 3 log_{10} kill at all dilutions.

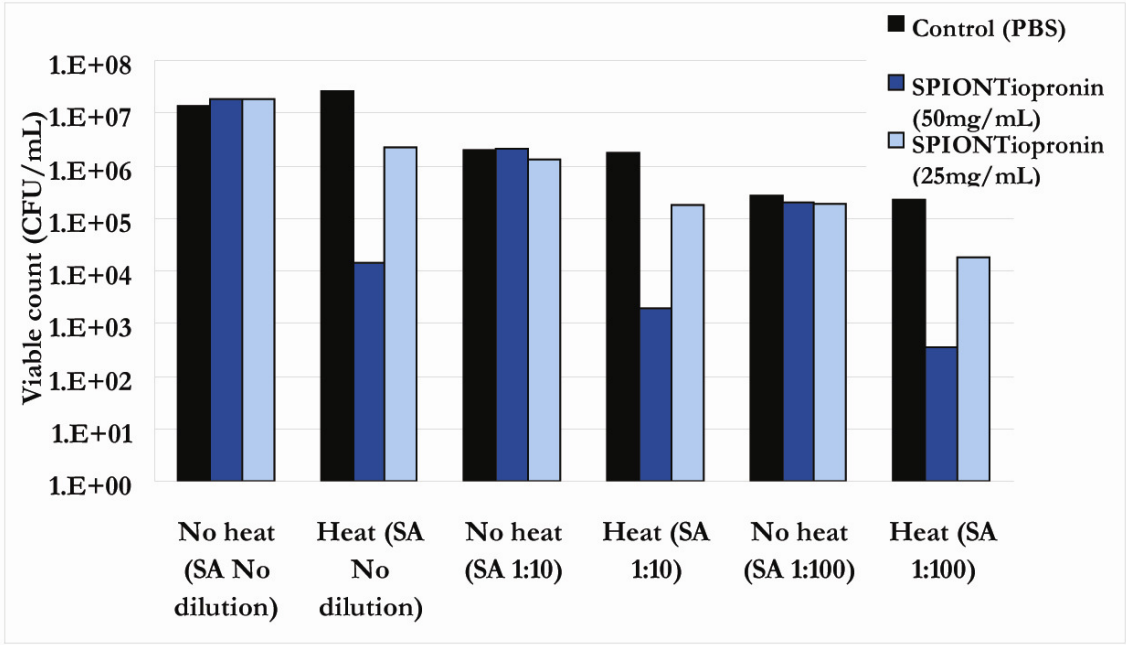

Figure 4-28 The bacterial count of *S.aureus* after exposure to iron oxide nanoparticles synthesised in a coprecipitation method in the presence of tiopronin, and at concentrations of 50 mg/ml (dark blue) and 25 mg/ml (light blue) in an inducing magnetic field. The *S.aureus* was wither not diluted, diluted to 1 part in 10 of PBS or 1 part in 100 of PBS. The experiment was run 19 days after the nanoparticle preparation.

4.6. Discussion

4.6.1. Sample Analysis

The data collected for all four samples showed similar results. FT-IR presented evidence for ligand coordination with νC-N and νO-H prevalent on all spectra. νFe-O stretches were strongly evident. In all cases the elemental analysis showed that very low concentrations of the organic ligand were attached to the iron oxide surface. Cases where TGA analysis was obtained did not correspond to any significant mass losses, however in the case of $SPION_{Tiopronin}$, $SPION_{Succinic}$ and $SPION_{EDTA}$ the first mass losses showed tentatively to corroborate with the elemental analysis of the coated nanoparticles. This information indicates that the carboxylic acids were present but were in small amounts coordinated to the nanoparticle. It is important to note that the pH values for all the samples varied

when the powder was resuspended in deionised water, particularly, that of the samples $SPION_{EDTA}$ and $SPION_{Oxamic}$ which at a pH of 5.38 and 3.95 were significantly lower than the other two samples and strongly indicate the presence of the acid. If there was any excess of the base TMAOH a high pH would have been seen. Without the presence of the carboxylic acids, it was not possible to collect isolated nanoparticles as following the dialysis purification the particles were noted to have precipitated out of solution. The pH changes can be explained by the presence of free unattached molecules of tiopronin, oxamic acid, succinic acid, and EDTA, however the intense purification process would have vastly eliminated this. The IR and Raman show that the total mass of the relatively heavy nanoparticle makes the stretches on the ligands difficult to observe, further indicating only a low presence of ligand attached to the iron oxide nanoparticles.

Hydrodynamic size measurements gave an average particle diameter of 135.2 nm for $SPION_{Tiopronin}$ with a polydispersity index of 0.265. The hydrodynamic size measurements for $SPION_{Succinic}$, $SPION_{Oxamic}$ and $SPION_{EDTA}$ gave larger results, 317, 870 and 378 nm respectively, with the measurement for $SPION_{Oxamic}$ being very polydisperse, 0.40, compared with 0.18 for $SPION_{EDTA}$ and 0.33 for $SPION_{Succinic}$. These hydrodynamic measurements are significantly larger than the crystallite sizes observed by XRD line-broadening, however this is because they are taken of full particle measurements in an aqueous environment.

M-H curves produced using the MPMS at 300 K and 10 K show that all four samples have little/no remnant magnetisation at 300 K, indicative of superparamagnetism. The zero field cooling (ZFC) curves all demonstrated a broad peak. A possible, although by no means conclusive explanation for this, could be that this is the Verwey Transition temperature. The deviation from the literature value may indicate that there has been some oxidation of the Fe(II) to Fe(III), which is likely to have occurred at the surface and not throughout the bulk. If this is the case, it would also imply that the particle size is small, thus having a large surface area.[189 190]

4.6.2. Antibacterial Evaluation

$SPION_{Tiopronin}$, $SPION_{Oxamic}$ and $SPION_{EDTA}$ all responded to an AC magnetic field producing an increase in temperature of the surroundings, $SPION_{Oxamic}$ was not tested as was too acidic to be further considered for any biomedical application. The strongest and most efficient was $SPION_{Tiopronin}$ which was then compared to two samples that are commercially available (Bayer Schering's Resovist and Micromod's Nanomag 100 nm), these two were identified as being useful for comparison after a study that was completed by Kallumadil in this group.[133] It was found to be over 4 times a better heater when placed inside the MACH system, when comparing the specific absorption rate and the intrinsic loss power. The measurements taken of the commercially available samples are in agreement with the measurements previously taken by Kallumadil. It is probable that the tiopronin in solution with the iron precursors limits the growth time after nucleation, giving rise to smaller particles that have high stability, thus low aggregation at neutral pH. This size optomisation of the particles leads to the superparamagnetism desired and an efficient response to the AC magnetic field.

This preliminary data meant $SPION_{Tiopronin}$ was suitable for further investigation as it was able to cause a significant heating effect that was potentially able to denature cells. The experiments showed that at concentrations of 25 mg/ml and 50 mg/ml it is possible to achieve killing of *S. aureus* by several orders of magnitude after a 2 minutes exposure in the MACH system. There was a direct correlation between the concentration of the ferrofluid and the kills achieved. The rate of killing was very much dependent on the temperature achieved. The initial testing showed that at a concentration of 50 mg/ml a total bacterial kill was seen and the sample was readily heated to 100^0C. A concentration of 50 mg/ml was still producing the same results more than one week after initial testing when the nanoparticles were stored at 4^0C. At the lowest concentration tested (6.25 mg/ml), the temperature reached was only 45.5^oC and consequently no significant bacterial kills were seen, a reasonable

explanation of this is that *S. aureus* is a mesophile and is known to tolerate short exposure (10 minutes) to a temperature of 50^{o}C.

After 19 days and sonication, the antibacterial effectiveness of the iron oxide nanoparticles was reduced but at 50 mg/ml they were still achieving more than a 3 log kill. This suggests that aging does have an effect on the composition and time and sonication oxidise the iron oxide. Indeed, there was a colour change from black to brown of the particles that is indicative of this. For longevity it would be best to keep the particles in an inert atmosphere until they needed to be used, however it is important to note that they will not degrade instantly and this makes them useful for the commercial and biological purpose they are intended for.

The exposure time to the MACH is also an important parameter which affects the bacterial kill, when using a 50 mg/ml concentration it was shown that total kill of a suspension containing 10^7 cfu/ml of bacteria was achieved after a two minute constant exposure. At one minute there was less kill, approximately 1.5 orders of magnitude being acheived. When bacteria were added to nanoparticles that had previously been exposed to a magnetic field in the MACH system, no killing was detectable. This finding suggests that the bactericidal effect observed in the other experiments is solely due to the heating effect of the particles rather than potential heat-induced release of toxic moieties from the nanoparticles. Functionalisation of the nanoparticles with bacteria-targeting moieties would enable the achievement of a localised heating effect and consequent bacterial killing without an accompanying temperature rise in host tissues. Following such a development, this novel means of killing bacteria could form the basis of a new approach to the treatment of infectious diseases.

4.7. Conclusions

The synthesis of iron oxide nanoparticles in the presence of four carboxylic acid functionalised ligands has been shown to change both the solubility properties, pH

in water and overall particle size. The particles which gave the best heating response to an alternating AC magnetic field were those which were formed with the ligand N-(2-Mercaptopropionyl)glycine (Tiopronin), $SPION_{Tiopronin}$. This gave a stable solution of iron oxide nanoparticles suspended in water at a biomedically favourable pH. This nanoparticle solution was shown to have an outstanding response to an AC magnetic field at various concentrations. The heating ability of this solution was over 4 times better than that of the best commercial samples; Bayer Schering's Resovist and Micromod's Nanomag 100 nm.

There was a direct correlation between the nanoparticle concentration and the kills of *S. aureus*. At 50 mg/ml a total kill of over 10^7 cfu of the bacteria was reported. Total kills were also achieved after a week using 50 mg/ml. Log magnitude bacterial kills were seen up to 19 days after initial testing, although there was evidence that the solution did degrade with time and sonication. The concentration of the $SPION_{Tiopronin}$ sample, and its AC field exposure time and type (pulse or continuous) varied heating efficiency and thus kill rates. We believe this to be the first time magnetic hyperthermia has been used to kill bacteria. It is possible that this approach may offer, following the development of a specific targeting system, a novel approach for the treatment of a variety of infectious diseases, an example of which is septacemia.

Chapter 5

Iron Oxide in the Presence of Phosphonate Functionalised Ligands

5.1. Introduction

As detailed in Chapter 4, phosphonates and bisphosphonates are a group of organic compounds that are being investigated in the stabilisation of iron oxide nanoparticles. Various phosphonates and bisphosphonates have previously successfully coated iron oxide nanoparticles whilst also promoting dissolution into aqueous media. A bisphosphonate has 2 phosphonate groups connected to a carbon, this is not to be confused with a diphosphonate that has 2 phosphonate groups but does not have a characteristic P-C-P backbone. The phosphonates have been used as coatings due to their strong chelating ability with metal ions, in

particular iron, and also for their proven biocompatibility. Examples include, but are not exclusive to, nitrilo tri(methanephosphonic) acid, diphosphoglyceric acid, etidronic acid, imino di(methanephosphonic) acid and 5-hydroxy-5,5-bis(phosphono)pentanoic acid, with the bisphosphonates proving to be better than the phosphonates.[154, 155]

The di- and bisphosphonates have been developed as pharmaceuticals due to their affinity for calcium which is abundant in bone. The bisphosphonate structure is analogous to the naturally occurring pyrophosphates which have a P-O-P backbone. These drugs are prescribed for illnesses including; osteoporosis, Paget's disease and myeloma, because they stop bone resorption by interfering with osteoclasts,[191] the cells which break down the bone matrix.[35]

Due to their metal chelating abilities bisphosphonate magnetic nanoparticles have been used to remove toxins from water and blood; an example of such is the work by Wang et al. that was able to remove UO_2^{2+} ions from blood.[192]

Shafi et al. investigated the interaction between various ligands and maghemite nanoparticles.[193] In comparison to the carboxylates and sulphonates they found that the extra negative charge in the phosphonate group causes it to be a strong bridging bidentate ligand, which has a stronger ionic bond with the Fe (III) of the nanoparticle. They put forward a theory that this also reduces the number of unpaired spins on the nanoparticle *via* a double superexchange from Fe(III)-O-P-O-Fe(III). Their results also showed that the presence of this bridging ligand resulted in a reduction in the magnetisation and they suggested that these surface ions are antiferromagnetically coupled with the phosphonate and this leads to superantiferromagnetic particles, as the phosphonate did not alter the particle size. Yee et al. also described low saturation magnetisation values when surface functionalising maghemite with octadecanephosphonic acid.[194] They too believe this to be due to interactions between the empty d orbitals on phosphorus and the Fe(III) spins on the surface.

In stark contrast to this work, Ngo et al. suggested that polyphosphate maghemite particles had no decrease in magnetisation.[195] Likewise, Daou et al. carried out similar experiments on 39 nm magnetite particles. They found that a carboxylate will cause spin canting in the oxidised surface of the nanoparticle resulting in a decrease in net magnetisation, whereas no such effect was observed when a covalently linked phosphonate was attached.[196] Figure 5-1 is taken from this paper and demonstrates these differences.

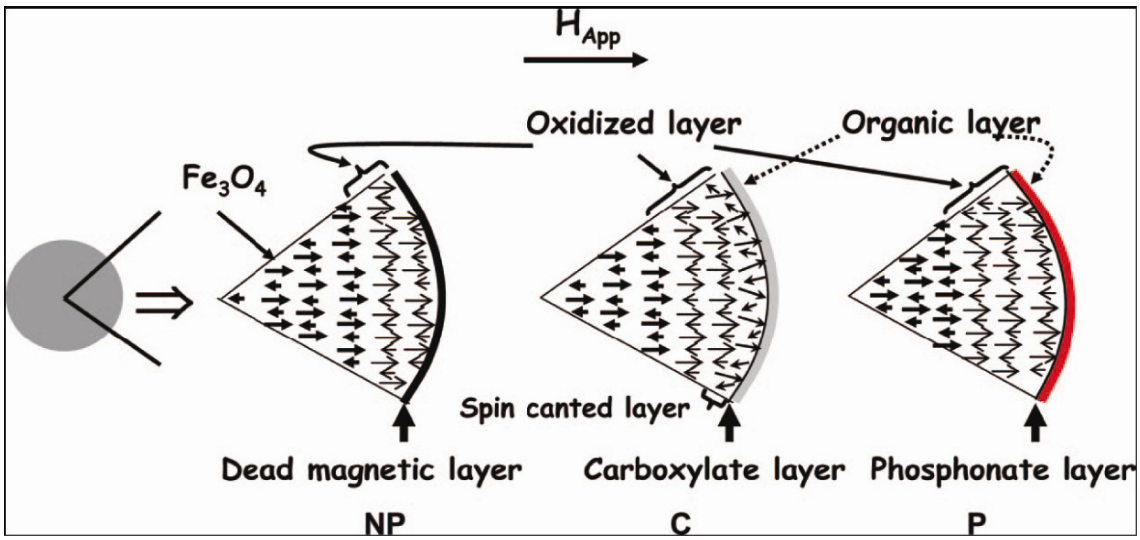

Figure 5-1 Diagram taken from Daou et al. demonstrating the effect of a carboxyl or a phosphonate ligand to the magnetism of a magnetite nanoparticle. The arrows within the nanoparticle cross sections represent the direction of the magnetic moments.[196]

5.2. Chapter Motivation

The phosphonates have been chosen for further investigation in the stabilisation of iron oxide nanoparticles in magnetic hyperthermia. The reasoning behind this thread of exploration, is that it has been shown that the carboxyl binding on metal oxide nanoparticle surfaces are much weaker, causing them to be washed away, whereas the phosphonates are much more strongly bound, and are preferentially attached over a carboxyl group causing them to still be interesting to research in the stabilisation of iron oxides.[197]

Due to the strong anchoring that a phosphonate has to the magnetic nanoparticle surface, and by selecting ligands that have alternative organic functional groups on them, it has been shown that further attachment chemistry can be performed to fix other moieties to the particle. Such an example of this ability is the attachment of the enzyme β-glucosidase using 4-(aminomethyl)benzylphosphonic acid as a linker.[198] This property is attractive for the application of magnetic hyperthermia for cancer therapy, as antibody fragment attachment is required to ensure heat targeting is specific to cancer cells.

Excitingly, some bisphosphonates have been shown to have antitumor properties of their own. An example of such is Zoledronate which is targeting to breast and prostate tumour cell lines.[199] By adhesion to a nanoparticle surface it is possible to ensure a dosage to these tumour cells as opposed to the drug being accumulated to its preferential tissue; the bone.

The methodologies reported for the complexation of phosphonate ligands include long periods of sonocation,[154] dialysis at low temperatures and using exchange resins.[155] This chapter looks at a new approach to see if the synthesis is possible using a one pot method that was reported in Chapter 4.

Finally, it cannot be ignored, as mentioned in section 5.1, that there is disagreement within the community regarding the effect a phosphonate has on the magnetic properties of a magnetic nanoparticle. However, until there is firm accord the phosphonates should not be discounted, this chapter looks to shed further light on these magnetic capabilities, and if this will indeed mean that phosphonated nanoparticles can be used in magnetic hyperthermia.

5.2.1. Ligand Selection

The desired outcomes of this chapter meant that the ligands selected needed to satisfy certain criteria. These were:

- water solubility so that a one pot synthesis could be achieved without the need for a phase transfer agent
- had two phosphonate groups
- at least one ligand needed to have a P-C-P backbone
- further attachment chemistry could be achieved by the presence of at least one other functional group
- they had proven biocompatibility

Due to availability, the two ligands selected were *N,N*-bis(phosphonomethyl) glycine (DPG) and 1-hydroxyethylidenediphosphonic acid (etidronic acid) (Figure 5-2). Both of these ligands have been studied previously by Portet et al.[155] where they investigated the attachment and stability of the phosphonate-iron oxide colloid through a different synthetic route, however, no further investigation into the magnetic properties, and most certainly their use in magnetic hyperthermia, has been performed to the best of the authors knowledge.

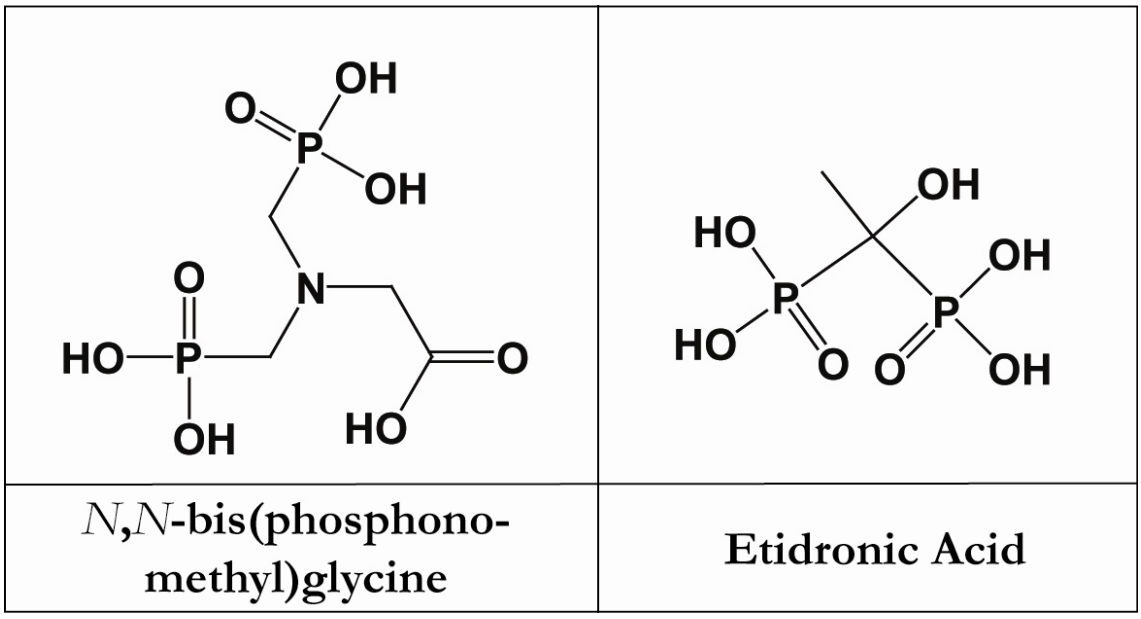

Figure 5-2 The two phosphonate functionalised ligands selected for the coating of the iron oxide nanoparticles synthesised *via* a coprecipitation method.

Etidronic acid is prescribed extensively as a treatment for many bone diseases.[200-202] Examples include osteoporosis and Paget's disease which are the first and second most common forms of bone disease respectively.[203]

DPG is normally used in agriculture,[204, 205] however, it is under investigation in a clinical capacity. DPG has been attached to platinum (II) antitumour drugs to increase targeting to bone metastasis that occur in breast cancer patients.[206]

5.3. Synthesis

5.3.1. Materials

All chemicals were purchased from Sigma Aldrich and were used as received with no further purification; iron (III) chloride hexahydrate (99%), iron (II) chloride tetrahydrate (≥99%), tetramethylammonium hydroxide (25% in water w/w) (TMAOH), *N*,*N*-bis(phosphonomethyl)glycine (≥98%), 1-hydroxyethylenediphosphonic acid monohydrate (etidronic acid) (≥95%). All water used was distilled.

5.3.2. Methodology

Similarly as to what was seen in the EDTA coating of iron oxide nanoparticles by coprecipitation (Section 4.3.3.), when the phosphonates were in the reaction vessel with the iron salts, an intractable mixture formed due to the strongly chelating properties of the ligands. Therefore an adapted methodology was pursued.

10 mmol of $FeCl_3.6H_2O$ in degassed water was placed into a round bottomed flask under constant nitrogen flow. To this was added 5 mmol of $FeCl_2.4H_2O$ in degassed water solvent. Due to the magnetic nature of the desired product the reactants were stirred mechanically using an overhead stirrer. The flask was heated in a silicone oil bath to 70^0C. Once at temperature 21 ml of TMAOH (25% in water w/w) was

added dropwise to the vigorously stirred solution. A black precipitate formed. After addition of the TMAOH the flask was immediately removed from the heat source but stirring continued. Once at room temperature an aqueous solution containing 5 mmol of the phosphonate ligand (DPG or etidronic acid) was added and the solution stirred overnight. This was then made up to 50 ml with distilled water and then transferred to a wet 20 cm strip of dialysis tubing (cellulose membrane, M.W. 12,400, average flat width 79 mm). This was secured and fastened at both ends and a magnetic stirrer attached. The membrane was placed into a 5 L beaker with approximately 4.5 L of 15 MΩ distilled water and stirred by placing on a magnetic stirrer plate. The water was recharged daily for 7 days. Upon completion of dialysis, the membrane was removed and the product was placed in a -80^{0}C freezer overnight, frozen and put under a high vacuum to remove the solvent. This freeze drying process took between 2-3 days and left a dry, brown powder.

Both the nanoparticle-DPG ($SPION_{DPG}$) and nanoparticle-etidronic acid ($SPION_{Etidronic}$) samples were readily resuspended in water without the need of any extra assistance such as heating or sonocation. The pH of the solutions made were 6.24 for $SPION_{DPG}$ and 5.79 for $SPION_{Etidronic}$ when at a concentration of 50 mg/ml in water and at room temperature.

5.3.3. Characterisation

Analysis of iron oxide nanoparticles formed in the presence of phosphonate functionalised ligands *via* a coprecipitation method was carried out using X-Ray diffraction (XRD) on a Bruker DX8 using CuK_α radiation, 1.54 Å ; Raman using a Renishaw inVia Raman Microscope with a laser wavelength of 785 nm and power of 1%; Infrared (IR) spectroscopy using a Perkin Elmer FT-IR Spectrometer Spectrum RX1; Thermogravimmetric analysis (TGA) using a Netzsh STA 449C instrument with helium gas; Magnetometry on a Quantum Design magnetic property measurement system MPMS-7 and photon correlation spectroscopy (PCS)

on a Zetasizer 3000 (Malvern, UK) was used to measure the hydrodynamic diameter of the nanoparticles in a plastic cuvette in distilled water at 25°C.

5.4. Results

XRD was run for all samples and, in all cases, tentatively confirmed a core composition of iron oxide in both magnetite and maghemite forms (Figures 5-3 and 5-8). The crystallite sizes for the samples were estimated using the Scherrer equation and peak broadening was taken into account using a Gaussian fit. The comparison was made to a LaB_6 standard.

5.4.1. DPG

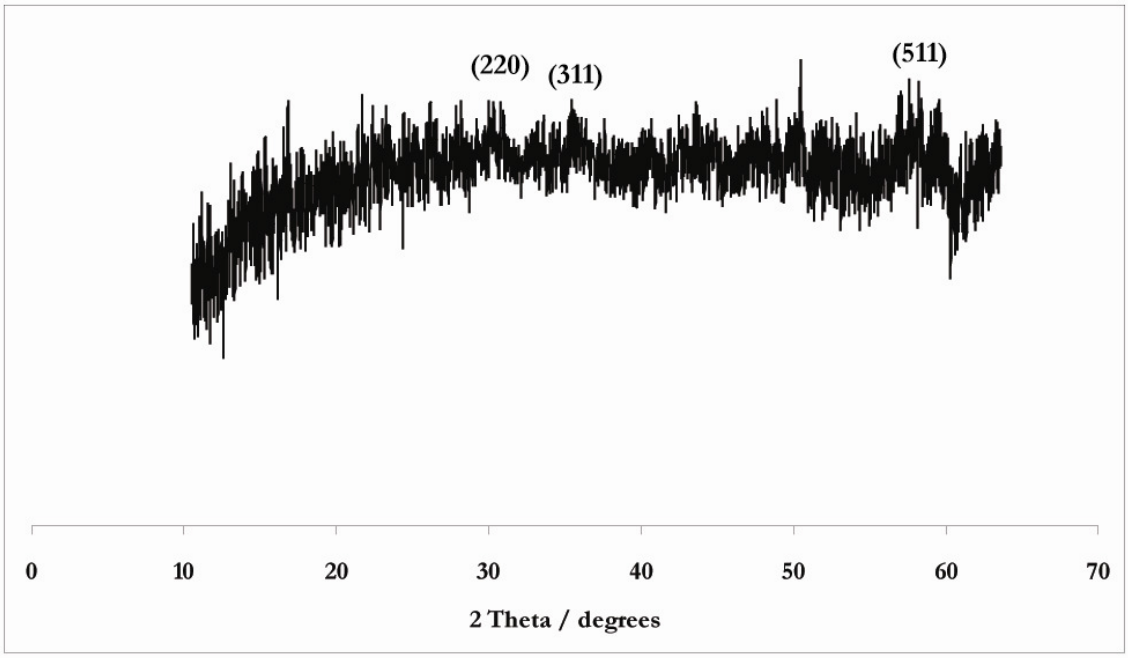

Figure 5-3 XRD pattern of DPG coated iron oxide nanoparticles synthesised *via* a coprecipitation method at 70^{0}C.

The $SPION_{DPG}$ particles were made using a one pot, two step modified coprecipitation synthesis. The use of the Scherrer equation in analysing the XRD data (Figure 5-3) gave an average crystallite size of 6.6 nm. The composition is a

magnetite-maghemite mix.[184, 185] The hydrodynamic diameter was measured to be 962 nm with a polydispersity index of 0.40.

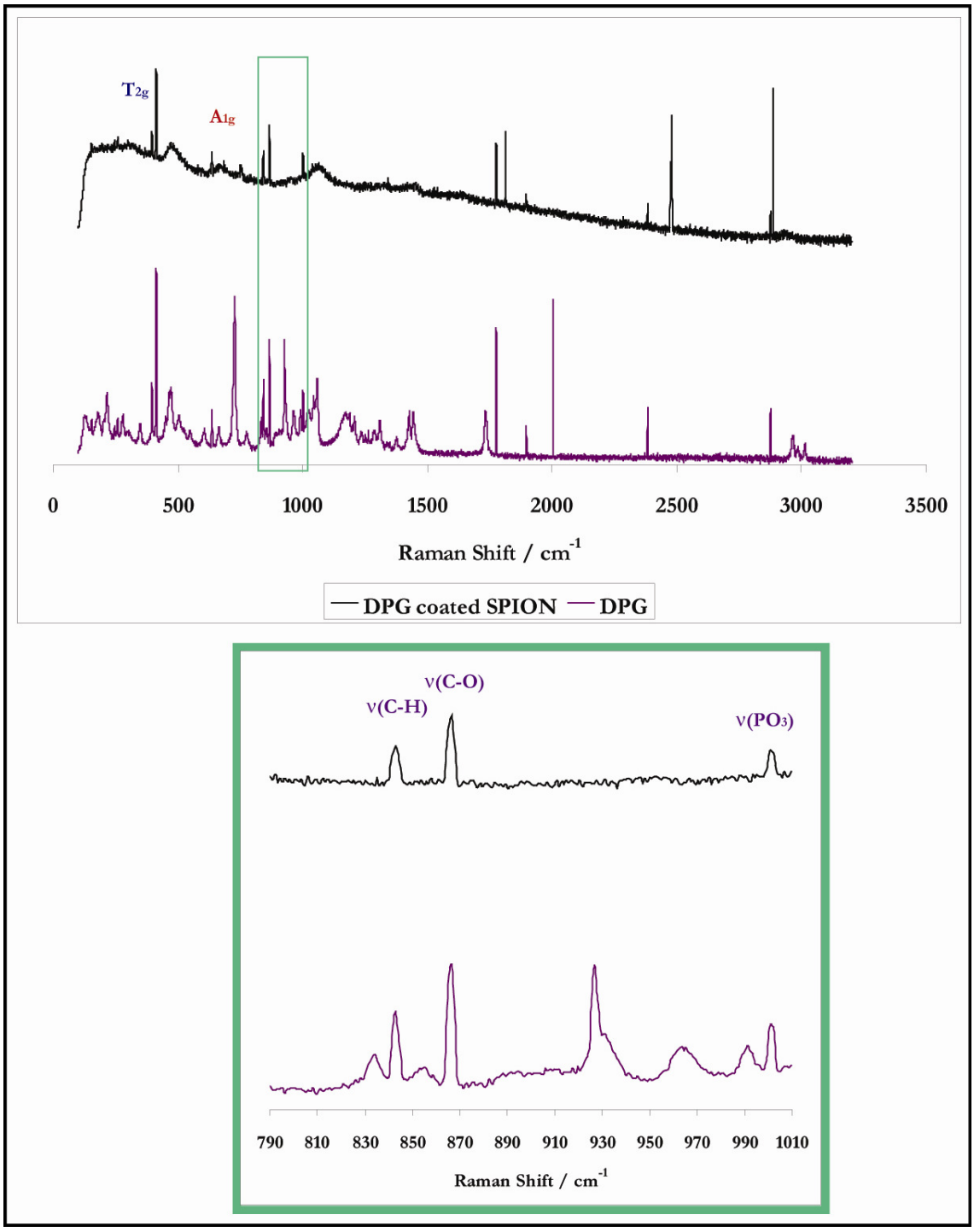

Figure 5-4 Raman spectra of DPG coated iron oxide nanoparticles formed *via* a coprecipitation method. There are corresponding peaks on the sample to that of the DPG ligand. The area between 790-1010cm^{-1} is highlighted for better clarity. Raman shifts are coloured blue for maghemite, red for magnetite, and purple for DPG.

Raman spectroscopy was run (Figure 5-4) and confirmed that there was a broad peak around 620 cm^{-1} that is indicative of an iron oxide, magnetite/maghemite, core.[186-188] The Raman spectra also confirm the presence of peaks arising from the DPG ligand in the $SPION_{DPG}$ sample around 930-1000 cm^{-1}.[207 208] This has been highlighted and a close up taken (Figure 5-4).

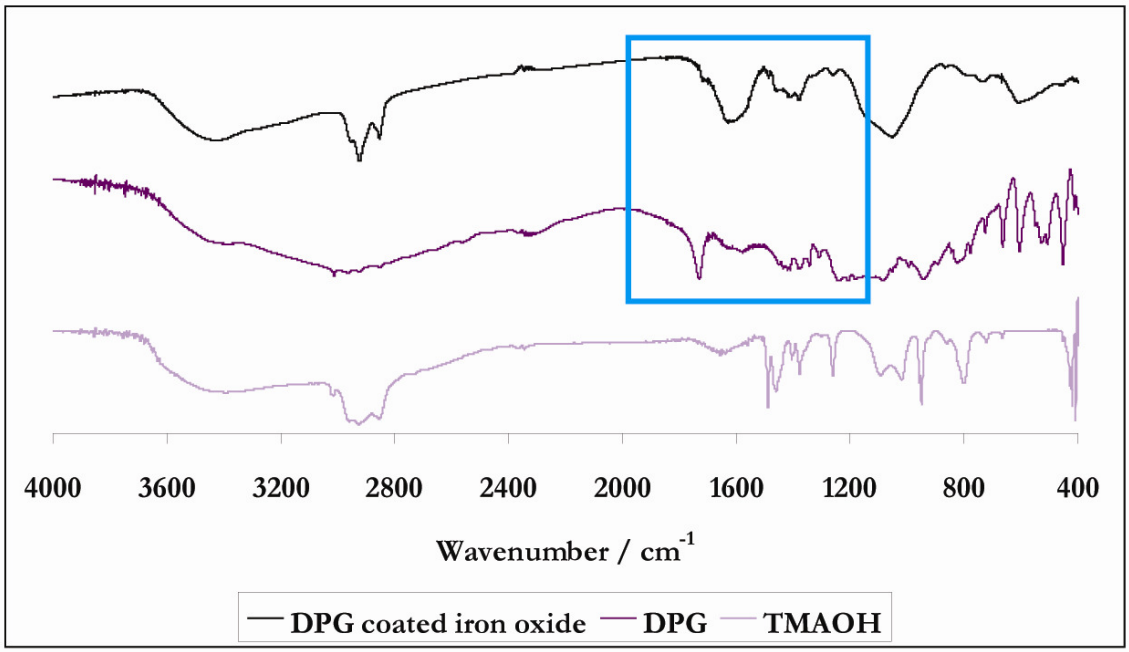

Figure 5-5 FTIR spectra of DPG coated iron oxide nanoparticles formed via a coprecipitation method. The spectrum of the free DPG and free tetramethylammonium hydroxide (TMAOH) that was used as a reducing agent are also shown. The area showing similar characteristics between the nanoparticle and the ligand which are not like that seen in the TMAOH are highlighted.

FTIR spectroscopy (Figure 5-5) confirmed Fe-O stretches from Fe(III) in the octahedral and tetrahedral sites. These can be seen in the artefact under 650 cm^{-1}. The peak at 580 cm^{-1} is less obvious in this sample due to the interference from the ligand stretches. There are some peaks that match both the ligand and TMAOH. However, there are some identifiable regions in the $SPION_{DPG}$ sample that seem to mimic those seen in the free ligand, and are not seen in free TMAOH. This area, ~1100-2000 cm^{-1}, has been highlighted for clarity. In all 3 spectra there is a strong

OH characteristic around 3500 cm^{-1}, which due to the abundance of OH, is unsurprising.

Elemental analysis advised that carbon content was 12.53% of the mass, hydrogen; 3.43% and nitrogen 3.67%. After the TGA was run, there was a residual mass of 57% likely to be the nanoparticle core (Figure 5-6).

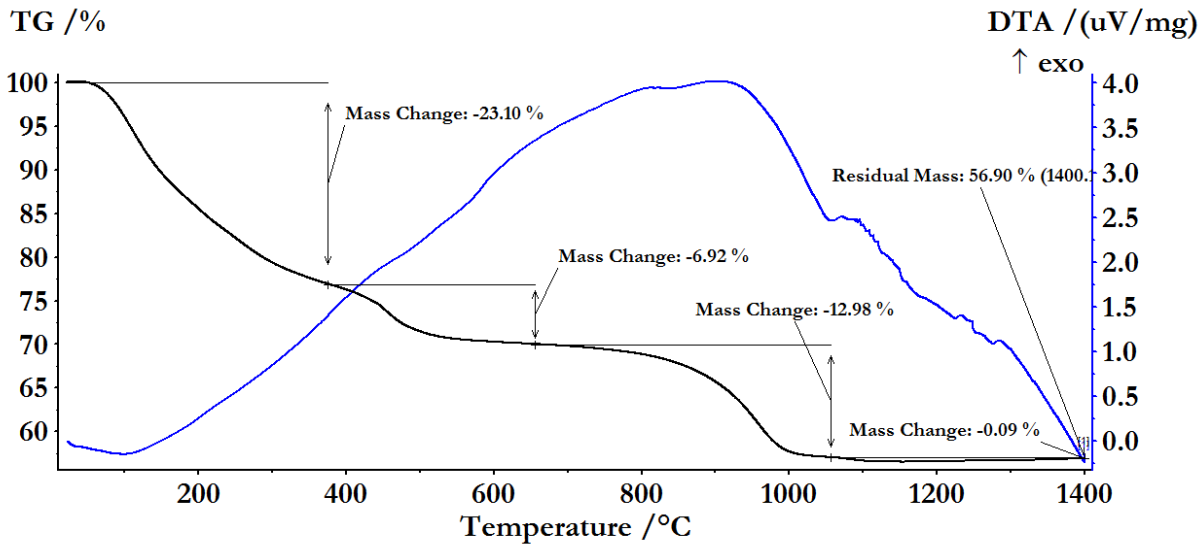

Figure 5-6 TGA analysis of iron oxide nanoparticles coated in DPG using an adapted coprecipitation method.

Figure 5-7 is the magnetic analysis of $SPION_{DPG}$. There is a small amount of coercivity, 60 Oe, at 10 K. At 300 K the curve has no coercivity; this indicates that the sample is superparamagnetic. M_s is 12 emu g^{-1}. The ZFC and FC curves are also seen and the broad shoulder at 120 K being the broadened Verwey transition because of surface oxidation of magnetite to maghemite.

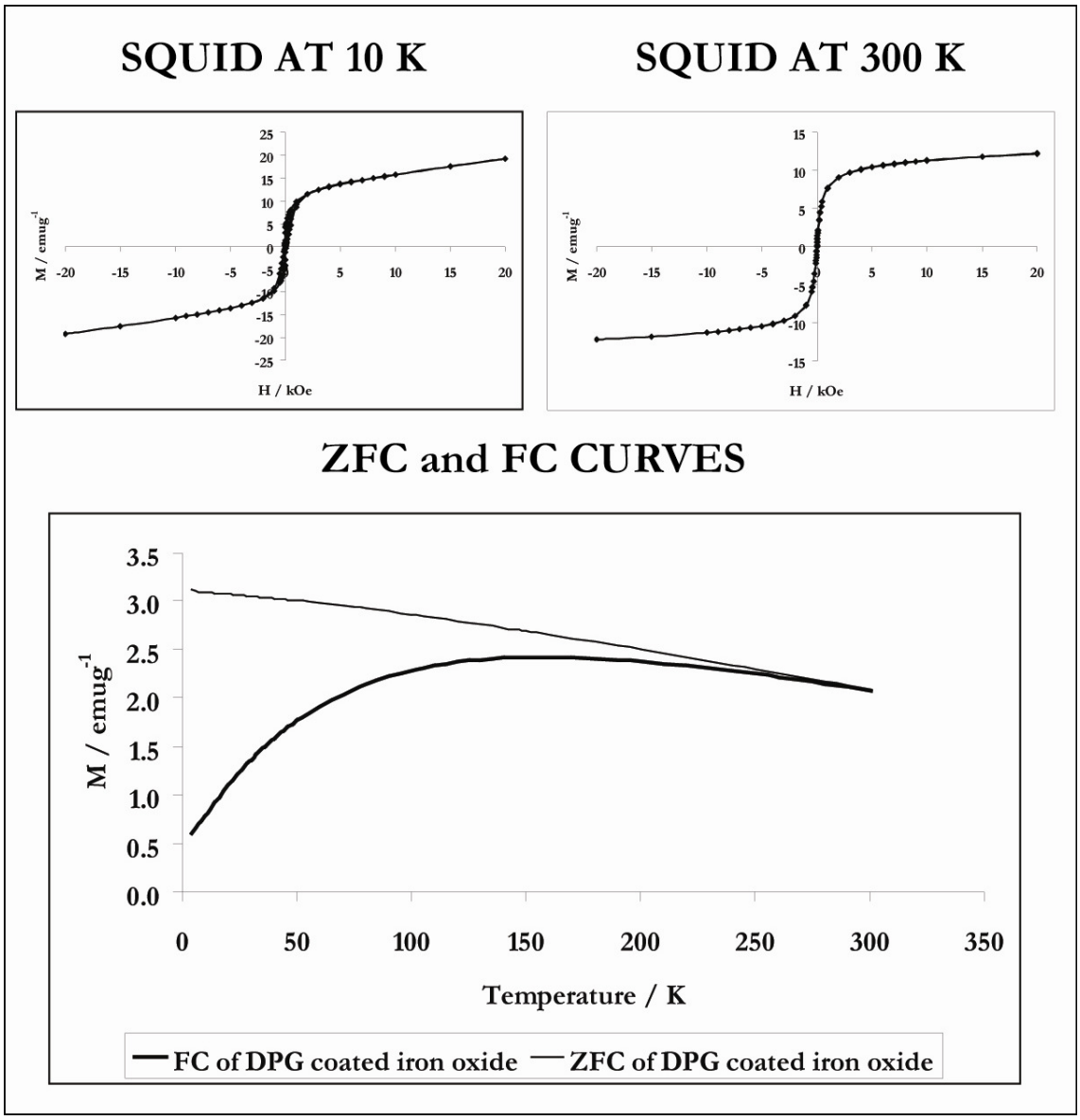

Figure 5-7 MH curves taken at 10 K and 300 K of etidronic acid coated iron oxide nanoparticles synthesised using an adapted coprecipitation method. The zero field cooling (ZFC) and field cooling (FC) curves are also shown.

The material underwent testing in the MACH system (see Chapter 2) to measure its heating response to the magnetic field. The SAR value was 3.28 W/g and the ILP was 7.04 x 10^{-14} Hm^2/kg. This material was the least efficient of those tested and synthesised (see Table 5-1).

5.4.2. Etidronic Acid

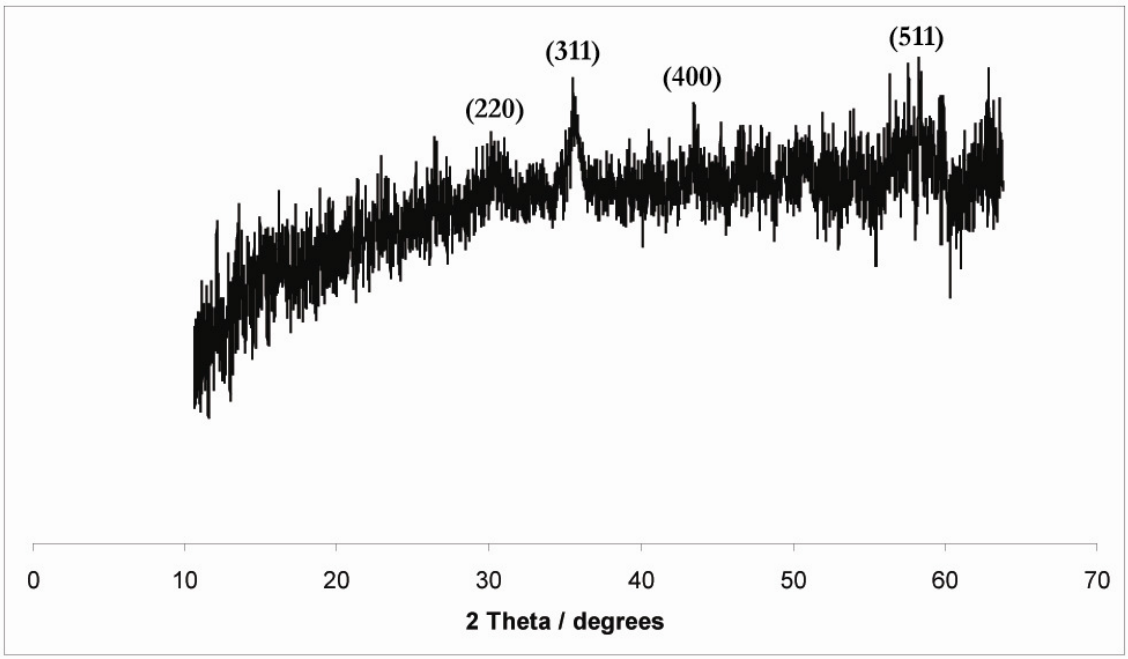

Figure 5-8 XRD pattern of Etidronic acid coated iron oxide nanoparticles synthesised *via* a coprecipitation method at 70^{0}C.

The XRD and Raman spectra of the $SPION_{Etidronic}$ showed there were peaks that were indicative of an iron oxide nanoparticle.[184, 185, 187, 188] The synthesis used was a coprecipitation technique with the addition of the etidronic acid ligand post nanoparticle formation within the same pot. The use of the Scherrer equation in analysing the XRD data (Figure 5-8) gave an average crystallite size of 17.3 nm. The hydrodynamic diameter was measured to be 177 nm with a polydispersity index of 0.28.

The strong etidronic acid peaks of PO_3 were also prevalent in the Raman spectrum for the $SPION_{Etidronic}$ (Figure 5-9).[207 208] A close up around of 985-1015 cm^{-1} has been highlighted so that this peak is easier to identify in both spectra.

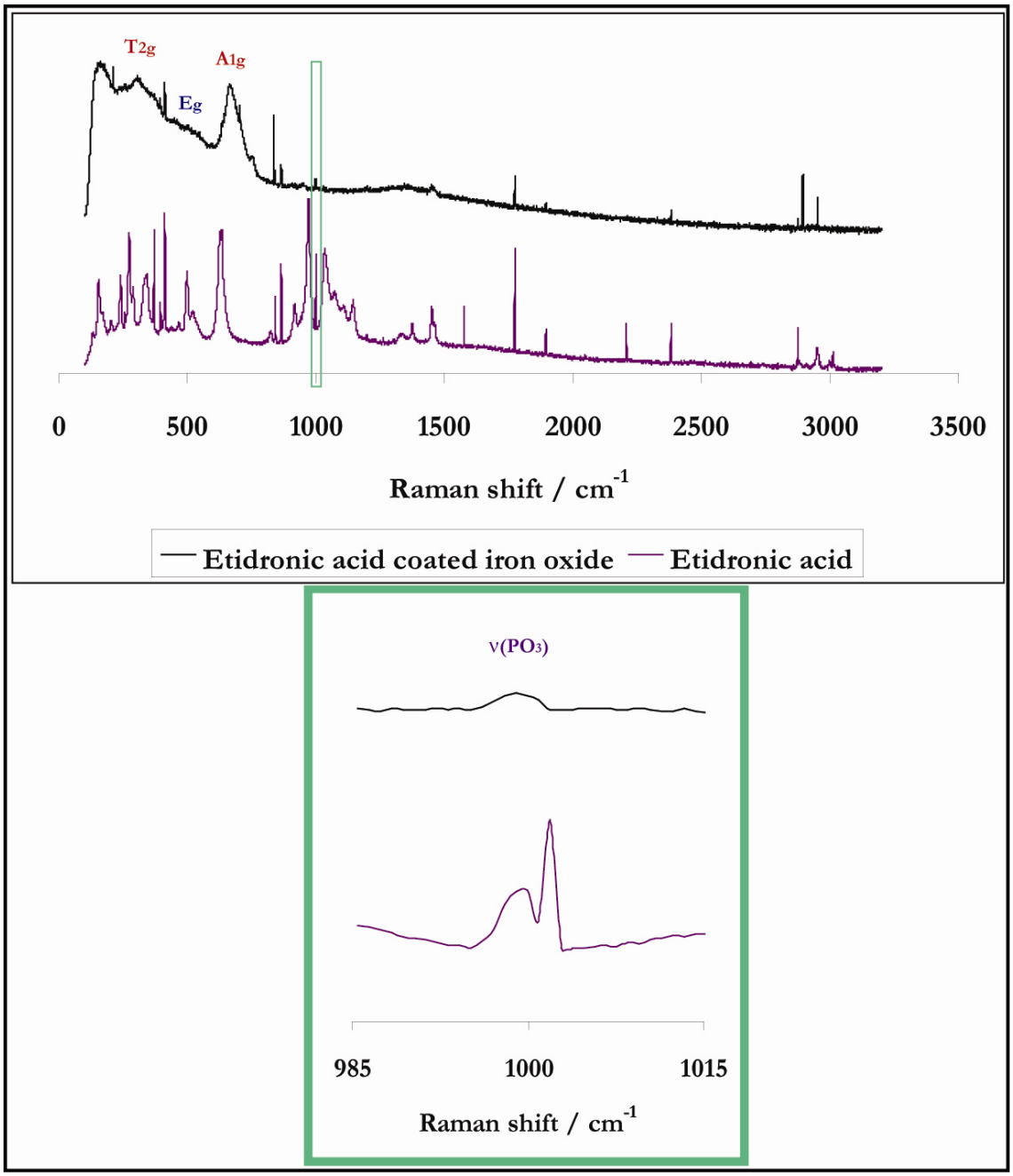

Figure 5-9 Raman spectra of etidronic acid coated iron oxide nanoparticles formed *via* a coprecipitation method. There are corresponding peaks on the sample to that of the DPG ligand. The area between 985-1015 cm^{-1} is highlighted for better clarity. Raman shifts are coloured blue for maghemite, red for magnetite, and purple for etidronic acid.

Alongside the expected υFe-O stretch, seen in all the other samples at the sub 650 cm^{-1} part of the FT-IR spectrum, there are two areas that seem to have strong characteristics of the etidronic acid ligand and cannot be attributed to an excess TMAOH (Figure 5-10). The artefacts are the broad gap between peaks at 1050-1450

cm^{-1} and the two small peaks that are seen between 600-900 cm^{-1}. Again the υOH characteristic around 3500 cm^{-1} is very strong in all spectra.

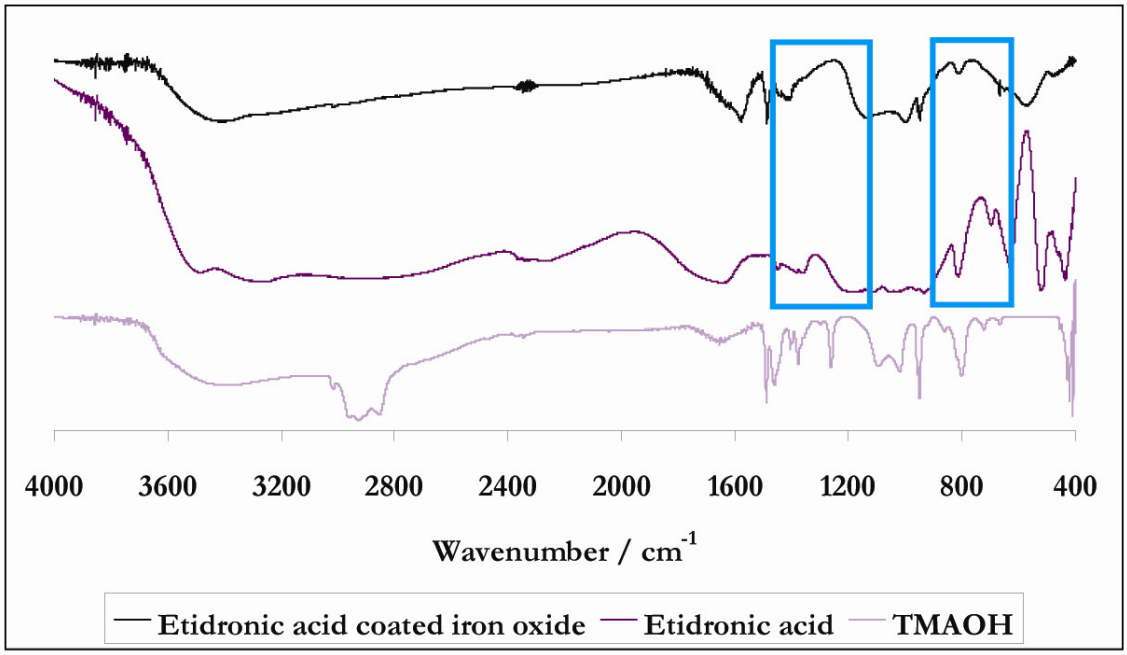

Figure 5-10 FTIR spectra of etidronic acid coated iron oxide nanoparticles formed via a coprecipitation method. The spectrum of the free etidronic acid and free tetramethylammonium hydroxide (TMAOH) that was used as a reducing agent is also shown. The area showing similar characteristics between the nanoparticle and the ligand which are not like that seen in the TMAOH are highlighted.

Elemental analysis showed that the carbon content was 12.52% of the mass, hydrogen; 4.13% and nitrogen 2.65%. Following the TGA a residual mass of 61% remained; the inorganic component (Figure 5-11).

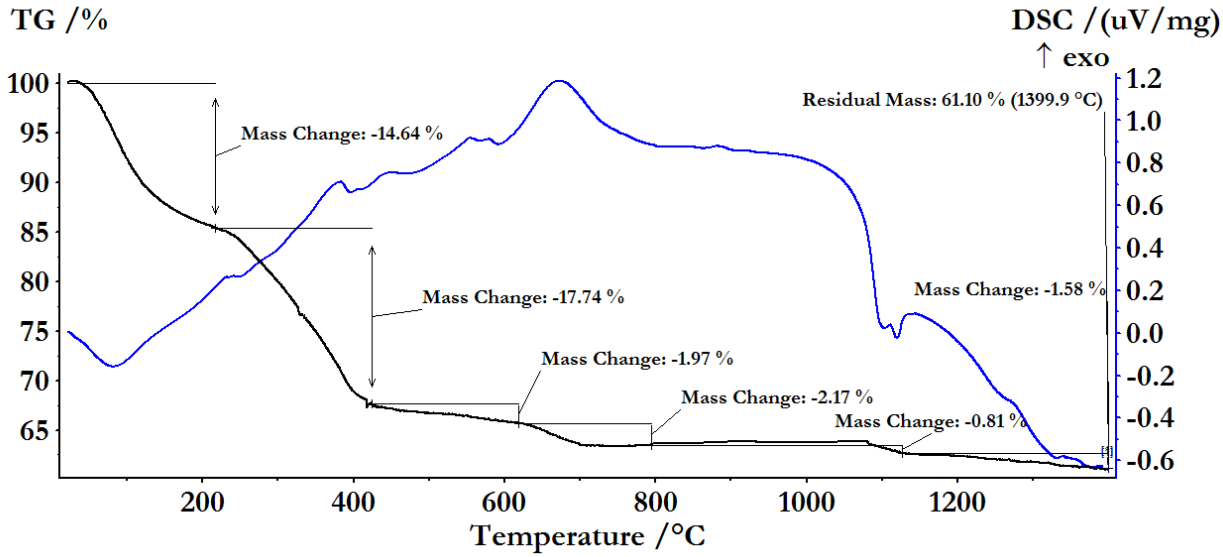

Figure 5-11 TGA analysis of iron oxide nanoparticles coated in etidronic acid using an adapted coprecipitation method.

Figure 5-12 shows the sample to be superparamagnetic due to there being no coercivity at 300 K but approximately 20 Oe at 10 K. The M_s of $SPION_{Etidronic}$ is 25 emu g^{-1} at 300 K.

Sample	SAR / W/g	ILP / Hm^2/kg
$SPION_{Tiopronin}$	1179	6.1×10^{-9}
$SPION_{DPG}$	3	7.0×10^{-14}
$SPION_{Etidronic}$	7	1.5×10^{-13}
Resovist	279	1.5×10^{-9}
Nanomag 100 nm	263	1.4×10^{-9}

Table 5-1 Table showing the SAR and ILP values of $SPION_{DPG}$ and $SPION_{Etidronic}$ compared to $SPION_{Tiopronin}$ (Chapter 4) and commercially available samples Resovist and Nanomag 100 nm.

The MACH testing of the material showed that of the two phosphonate functionalised SPIONs, $SPION_{Etidronic}$ was the best with a SAR value of 7 W/g and an ILP of 1.5×10^{-13} Hm^2/kg. However, these values were still significantly less that

those measured for carboxylic acid functionalised $SPION_{Tiopronin}$ and commercially available samples (Table 5-1) and so no further testing of the material for cell denaturing was carried out.

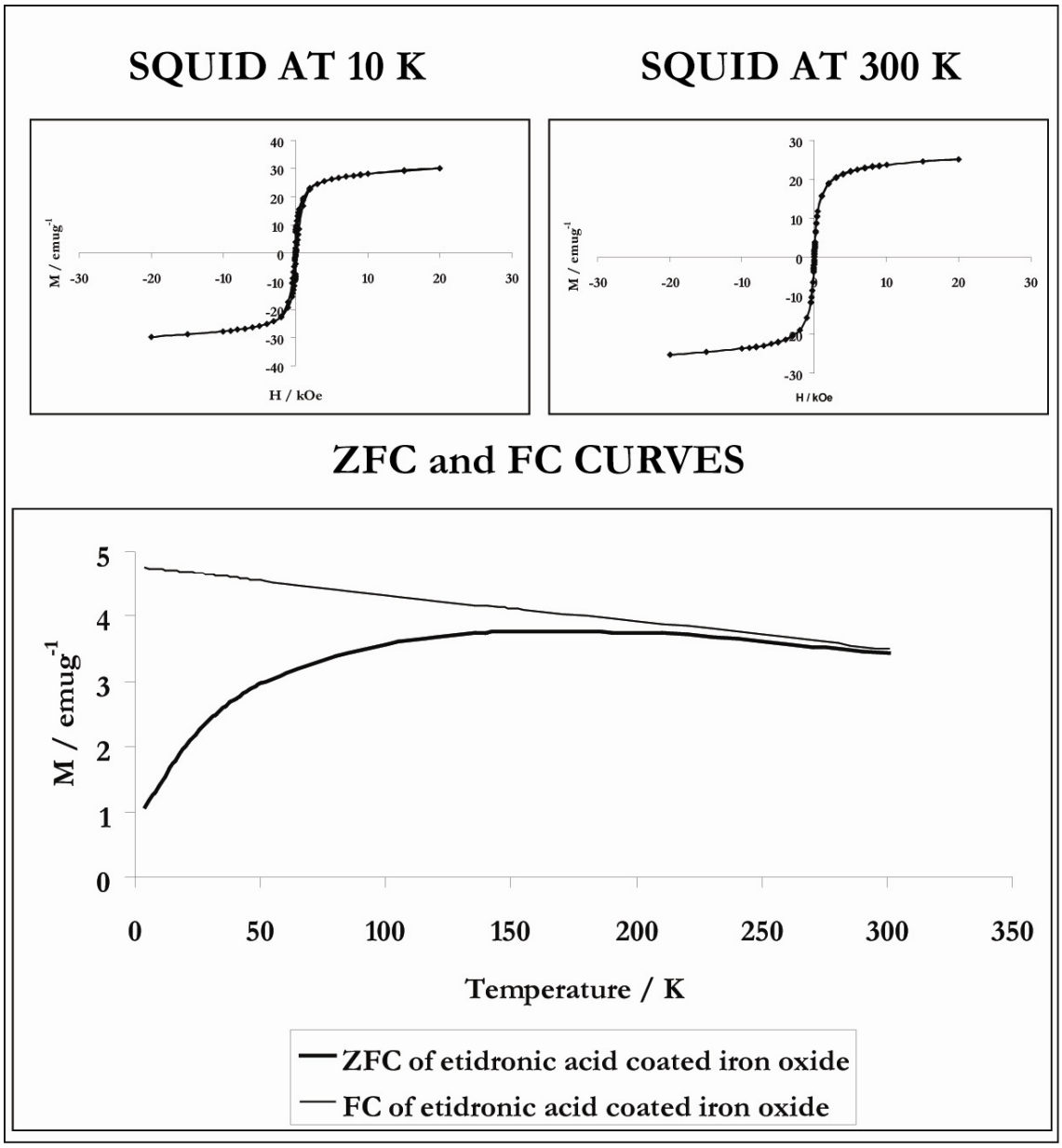

Figure 5-12 MH curves taken at 10 K and 300 K of etidronic acid coated iron oxide nanoparticles synthesised using an adapted coprecipitation method. The zero field cooling (ZFC) and field cooling (FC) curves are also shown.

5.5. Discussion

Both $SPION_{DPG}$ and $SPION_{Etidronic}$ were confirmed as being magnetite cores with oxidised maghemite surfaces, using XRD (Figures 5-3 and 5-8), FTIR (Figures 5-5 and 5-10) and Raman (Figures 5-4 and 5-9) to confirm this.

FTIR and Raman spectroscopy identified strong peaks from the phosphonate ligands in both of the phosphonated nanoparticles. TGA showed the residual masses for $SPION_{DPG}$ and $SPION_{Etidronic}$ to be 57% and 61% respectively. If the residual mass is taken to be the inorganic core component, this would indicate that roughly 40% of the mass is made up of the phosphonate organic shrubbery. Elemental analysis showed that significant amounts of the constituents of each ligand were detectable. This is strong evidence for the attachment of phosphonate to an iron oxide nanoparticle using a simple, two steps, one pot, methodology; coprecipitation followed by stirring with the ligand.

An anomaly in the CHN analysis of $SPION_{Etidronic}$ showed a reasonable amount of nitrogen still remaining (3.67%). This is even more than had been seen in the elemental analysis of the carboxylated SPIONS seen in Chapter 4, which may have come from traces of left over surfactant/reducing agent. Considering dialysis of the phosphonated SPIONS took place over a longer period of time, an extra 3 days, it would be expected that N content would at least be less than that seen in Chapter 4. A logical conclusion from this is that an *in situ* side reaction has occurred at the –OH terminus of the etidronic acid. Etidronic acid is a first generation bisphosphonate and is used as a starting material to synthesise N-containing bisphosphonates,[98, 155, 209 7] and the evidence looks to indicate that that this has happened upon addition to the TMAOH rich solution in the synthetic process. A possible mechanism for this is detailed in Figure 5-13.

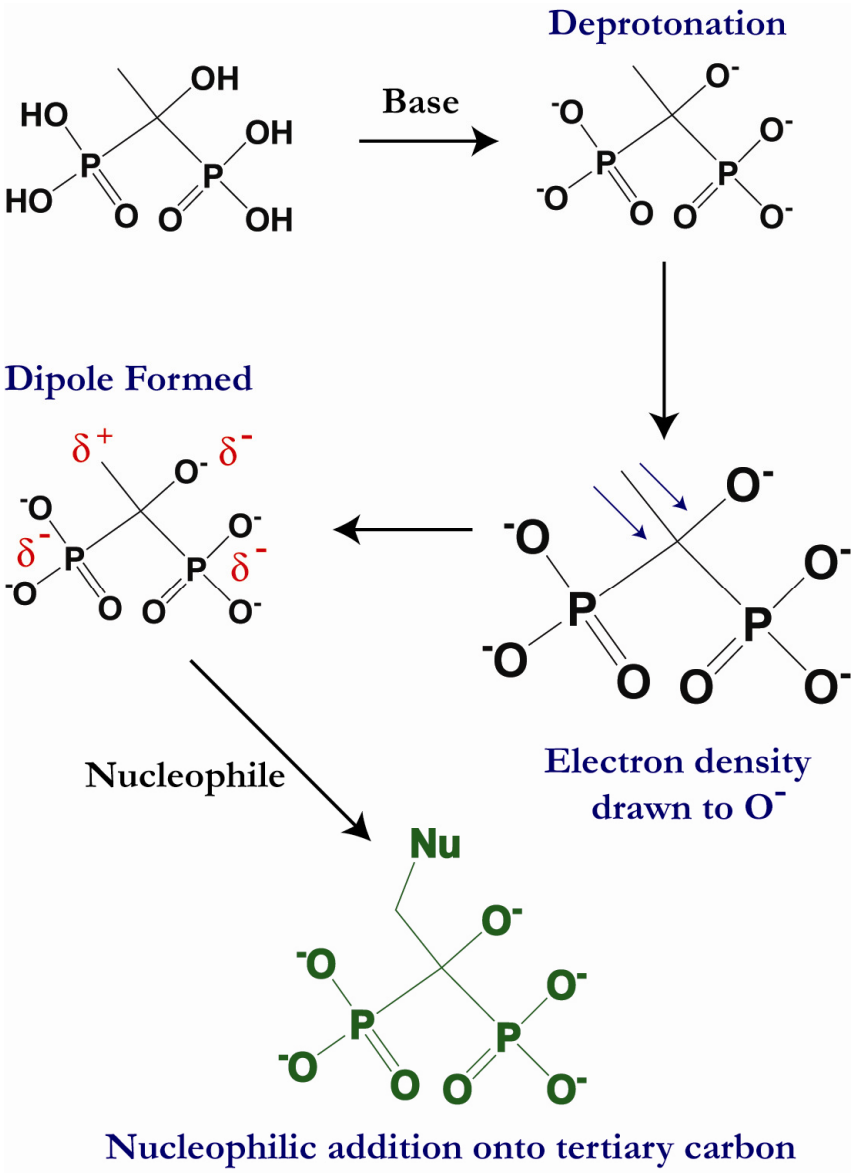

Figure 5-13 Schematic showing a possible mechanism for a nucleophilic addition to etidronic acid, following etidronic acid addition immediately after iron oxide nanoparticle formation in a coprecipitation synthesis using a base as the reducing agent.

This shows that in base, deprotonation of the etidronic acid will occur. The electronegative oxygen atoms would draw the electron density towards them, creating a dipole with the positive dipole at the tertiary carbon. This tertiary carbon is then open to attack from a nucleophile and a nucleophilic addition can occur. In this example the base is the TMAOH and the nucleophile the nitrogen component of the TMAOH. Further investigation, particularly using NMR, without the magnetic particle, would be useful to determine this. Although not desired in this

process, this may be of importance in future development, whereby targeting antibody fragments could be anchored to the bisphosphonate in a simple step. Instead of using a nitrogen containing reducing agent, the iron salts could be reduced to iron oxide using sodium hydroxide and this could then preferentially attach a nitrogen containing an antibody fragment.

The pH of the 50 mg/ml SPIONs in water was 6.24 and 5.79 for DPG and etidronic acid stabilised nanoparticles respectively. These indicate that the phosphonate ligands are present, as without these the pH of a stable iron oxide nanoparticle solution formed in a basic environment would have been in the basic range. The acidity of $SPION_{Etidronic}$ is something that would need further investigation to see if this could be tolerated physiologically. However, this should not be discounted as the strong bond between the bisphosphonate and the particle surface make it an ideal candidate for the anchorage of further targeting moieties. With further functionalisation the etidronic acid coated nanoparticle could be better suited for magnetic hyperthermia by increasing its pH to near neutral, particularly if this is to be injected intravenously where the blood pH tolerance is very narrow, between 7.35 and 7.45.[210 8]

The SQUID run at 10 K and 300 K does prove that $SPION_{DPG}$ and $SPION_{Etidronic}$ are superparamagnetic. This is because superparamagnetic materials behave differently above and below the blocking temperature; below the temperature coercivity is seen but above the material displays paramagnetic properties whereby there is nil coercivity. This was seen in the SQUID data taken of the nanoparticles. As described in Chapter 1, it is important for the biomedical applications that the SPIONs are superparamagnetic. The magnetic data indicates that the phosphonate attachment does not hinder this.

The SQUID also indicates that the M_s values for both samples are less than that which is seen in the samples stabilised using a carboxylic acid functionalised ligand (Chapter 4). $SPION_{DPG}$ was only approximately 12 emu g^{-1} and $SPION_{Etidronic}$ was

25 emu g^1. Also, unlike in the case of the carboxylated-nanoparticles where the saturation magnetisations values were equivalent, there is a marked difference between the two phosphonate ligands. This is unlikely to be because of the amount of magnetic material, as both TGA data sets gave residual masses of around 60%. This implies that there are equivalent masses of ligand present; this is because despite the etidronic acid being smaller and around 78% of the mass of DPG, due to sterics more of the ligand is able to associate to the nanoparticle. Alternatively, based on the hypothesis that the etidronic acid was modified by the TMAOH in the synthesis, the ligand may be larger and therefore carry a greater mass. Crystallite size estimations gave the $SPION_{DPG}$ core as an average of 6 nm and $SPION_{Etidronic}$ as an average of 17 nm. This could explain the difference in the saturation magnetisation. Further investigation, by addition of the ligands to the same initial nanoparticle solution could look to verify if the phosphonates affect the size, or if the nanoparticle size was already predetermined.

If the difference in M_s is because of the ligand used, this indicates that $SPION_{Etidronic}$ may be of more use in magnetic hyperthermia. It has been shown that SAR values are not necessarily bigger with larger M_s values,[130] however, the SAR value for $SPION_{Etidronic}$ is double that of $SPION_{DPG}$ (6.8 and 3.28 W/g respectively) which mirrors that which is seen for the M_s values. In the case of $SPION_{Tiopronin}$ (Chapter 4), the SAR value is 1179 W/g, when the M_s is 49 emu/g. The M_s of $SPION_{Tiopronin}$ is twice that of $SPION_{Etidronic}$ and the SAR is over 173 times larger. This again shows that the SAR is larger when the M_s is larger, however, if these two values are intrinsically linked then the relationship is more complex than being directly proportional.

5.6. Conclusions

It has been shown that it is possible to stabilise iron oxide nanoparticles using a phosphonate functionalised ligand in a simple one pot process. This straightforward methodology shows that by immediately adding the ligand to a newly formed iron

oxide nanoparticle solution, and following stirring at room temperature, the ligand will attach. After purification from the excess surfactant/reducing agent used to synthesise the nanoparticles, the powder is readily soluble in water with no aggravation required. The type of ligand used does affect the pH of the ferrofluid, and therefore this should be a consideration when selecting phosphonate ligands for biomedical applications. Around 40% of the total mass of a powder came from the phosphonate indicating the abundance of ligand present, this is due to the strength of the nanoparticle-phosphonate interaction meaning washing and purification does not remove much of the ligand.

The particles were superparamagnetic, which is highly desirable for the clinic. The saturation magnetisation, SAR and ILP values for $SPION_{Etidronic}$ were twice that of $SPION_{DPG}$, this indicates that $SPION_{Etidronic}$ may be more useful in magnetic hyperthermia, however these values were considerably lower than $SPION_{Tiopronin}$ at 1179 W/g.

Chapter 6
Conclusion

6.1. Results Summary

This thesis has investigated the synthesis and stabilisation of iron oxide nanoparticles prepared using a coprecipitation methodology, using either carboxylic acid or phosphonate functionalised ligands. This was for the purpose of improving biocompatibility and heating response when used in magnetic hyperthermia for biomedical applications.

The coprecipitation method is a common synthetic route to nanoparticle formation by reducing the iron salts to iron oxide by pH adjustment. However, the chaotic reaction process occurring within the reaction vessel has meant that size, and thus property, control is difficult. The growth process that occurs in the literature is often cited to be Ostwald ripening, whereby due to the need to reduce surface energy, larger particles engulf smaller particles. With the desire to reach a better understanding of the growth process and to gain more control of size

determination, the effects of temperature and rate of addition of the reducing agent in the coprecipitation reaction to produce functionalised iron oxide nanoparticle was investigated. The results of these experiments showed that average particle and cluster size were co-dependent, and early evidence suggests they were proportional to temperature and inversely proportional to the addition rate of the reducing agent. The polydispersity of the nanoparticle was found to be linked in the same way.

Using these results the growth mechanism in the formation of iron oxide nanoparticles was investigated. Interestingly, it has been shown that it cannot be assigned to just one type; Ostwald ripening. An alternative view is that depending on the reaction conditions different mechanisms would dominate. The theory put forward in this thesis is that increasing temperature means the coalescence mechanism is favoured, whereby growth occurs due to increased Brownian motion, and correctly orientated collisions between nanoparticles are more probable. Alternatively, with lower addition rate of the reducing agent, the traditional Ostwald ripening mechanism is preferred in this system. This is because there is more distance between nucleation points and more time between growth periods, causing the particles formed at the beginning to grow and internalise the newer, smaller particles.

Alongside the formation of a magnetic core, stabilisation at neutral pH had to be achieved. Short chained carboxylic acid functionalised ligands and ligands with two phosphonate groups were chosen. The literature shows that phosphonates and long chain carboxylic acids are useful in stabilising SPIONs. The particles were synthesised in a one pot coprecipitation method where the ligand was either *in situ* ($SPION_{Tiopronin}$, $SPION_{Succinic}$, $SPION_{Oxamic}$) or added post magnetite formation ($SPION_{EDTA}$, $SPION_{DPG}$, $SPION_{Etidronic}$). The weaker bond between the carboxylic acid and the nanoparticle was evident, because analysis showed only trace levels of the ligand in comparison to the phosphonate ligands, which were much easier to identify. The shelf life and ease of solubility were both better with phosphonated SPIONs.

Magnetic analysis of the ligand stabilised nanoparticles showed that the carboxylated SPIONs gave greater M_s values than their phosphonate analogues. Initially, it would seem that this may be because, per unit gram, there is less magnetic material in a phosphonate SPION. However, taking this into account, even $SPION_{Etidronic}$ which had the largest M_s, has an average of only three quarters the M_s value of the carboxylated SPIONs. This gives further support to the groups that believe that the phosphonate groups interfere with the magnetism of the iron oxide nanoparticles. The thoughts being that the empty d orbitals on phosphorus interact with the Fe(III) spins and a possible double superexchange takes place.[182]

Many of the samples reported in Chapters 4 and 5 were tested in the MACH for a positive heating response to an AC magnetic field. The only sample not to be tested was $SPION_{Oxamic}$ which was too acidic to be investigated further for biomedical applications. The SPIONs which were coated in a phosphonate functionalised ligand were less responsive to the field than the SPIONs coated in a carboxylic acid functionalised ligand. This mirrored that magnetic behaviour seen in the SQUID analysis.

The $SPION_{Tiopronin}$ had the largest SAR/ILP reported to date. This was explored further and used in antimicrobial testing of *Staphylococcus aureus* using a water bath kill technique. The particles were non toxic when away from the inductive field of the MACH. Concentrations of 50 mg/ml gave consistent total kills and bath heating temperatures of 100^0C. Total kill counts were proportional to particle concentration. It was also shown that a continuous exposure to the alternating field was more efficient than a pulsed field exposure in killing bacteria. This is an alternative application to cancer cell thermoblation, and it is hoped this may be of use in treating patients with bacterial infections, such as septicaemia, as the kill is indiscriminate and would therefore reduce the need for antibiotics. It is believed this is the first ever application of magnetic hyperthermia in antimicrobial studies.

6.2. Future Work

As touched upon in Chapter 3, to understand the pathways to nanoparticle growth in a coprecipitation synthesis a new and thorough model is needed. This would give the experimentalist greater understanding and thus the ability to gain control of the synthesis for repeatable results. An experiment looking into each variable would need to be run followed by TEM imaging and DLS measurements. The variables not investigated in this thesis are; reactant concentrations, strength of reducing agent, surfactant contributions and mixing conditions. To each of these, trends in particle sizes could be indentified, and a hypothesis of the type of growth mechanism that dominates could be put forward. With this full set of data, an extensive and thorough model could be produced. The ability to control the nanoparticle coprecipitation synthesis is useful to all experimentalists using this technique, not just in the synthesis of magnetic nanoparticles. However, with size control comes the control on the magnetic properties, and this will be useful in fine tuning the "designer nanoparticle" for magnetic hyperthermia.

The $SPION_{Tiopronin}$ has been shown to be an excellent heater. The thiol end group of the tiopronin would be useful in attachment chemistry and this could be attempted. The antimicrobial study could also be developed beyond a bath heating exercise to make it more useful in clinical applications.

Further investigation on a suite of GMP approved bisphosphonates coated nanoparticles in the MACH would be useful to identify optimum heaters. It is the intention of this project that the particles can be used in the magnetic hyperthermia treatment of cancer cells. The attachment of targeting moieties to these stabilised nanoparticles is the next step in this work to be carried out at the Cancer Institute at UCL, London. It has been shown that this attachment could be made possible by a nucleophilic addition onto the tertiary carbon of etidronic acid all in the one pot process. This would certainly need further analysis, particularly using NMR, to establish where the nitrogen content of the sample has arisen from, but is an

interesting strand for consideration. The bisphosphonate functionalised ligands should also be studied *in vivo*, to see where they accumulate. It is proposed there might be preferential uptake in the bone, but this cannot be ascertained without full scrutinisation. If the affinity that the bisphosphonates have for the bone is still dominant upon nanoparticle attachment, they may also be used in targeting bone metastases which are common with breast cancer, thus being targeting without any further attachment chemistry. Finally, an antimicrobial examination, such as that seen with $SPION_{Tiopronin}$, may also be interesting to develop.

References

1. Editorial, "Small is different." *Nature Nanotechnology* 2006, 1, (1), 1-1.

2. Gao, J. H.; Gu, H. W.; Xu, B., "Multifunctional Magnetic Nanoparticles: Design, Synthesis, and Biomedical Applications." *Accounts of Chemical Research* 2009, 42, (8), 1097-1107.

3. Maynard, A. D.; Aitken, R. J.; Butz, T.; Colvin, V.; Donaldson, K.; Oberdorster, G.; Philbert, M. A.; Ryan, J.; Seaton, A.; Stone, V.; Tinkle, S. S.; Tran, L.; Walker, N. J.; Warheit, D. B., "Safe handling of nanotechnology." *Nature* 2006, 444, (7117), 267-269.

4. Rai, M.; Yadav, A.; Gade, A., "Silver nanoparticles as a new generation of antimicrobials." *Biotechnology Advances* 2009, 27, (1), 76-83.

5. Kroto, H. W.; Heath, J. R.; O'Brien, S. C.; Curl, R. F.; Smalley, R. E., "C60: Buckminsterfullerene." *Nature* 1985, 318, (6042), 162-163.

6. Toumey, C., "The man who understood the Feynman machine." *Nature Nanotechnology* 2007, 2, (1), 9-10.

7. Gerber, C.; Lang, H. P., "How the doors to the nanoworld were opened." *Nature Nanotechnology* 2006, 1, (1), 3-5.

8. Kreuter, J., "Nanoparticles - a historical perspective." *International Journal of Pharmaceutics* 2007, 331, (1), 1-10.

9. Asiyanbola, B.; Soboyejo, W., "For the surgeon: An introduction to nanotechnology." *Journal of Surgical Education* 2008, 65, (2), 155-161.

10. Darling, S. B.; Bader, S. D., "A materials chemistry perspective on nanomagnetism." *Journal of Materials Chemistry* 2005, 15, (39), 4189-4195.

11. Orchard, A. F., *Magnetochemistry*. Oxford University Press: Oxford, 2003.

12. Atkins, P. W.; de Paula, J., *Atkins' Physical Chemistry*. 7th Edition ed.; Oxford University Press: Oxford, 2002.

13. Jiles, D., *Introduction to Magnetism and Magnetic Materials*. Chapman & Hall: London, 1991.

14. Bertotti, G.; Basso, V.; Beatrice, C.; LoBue, M.; Magni, A.; Tiberto, P., "Hysteresis in magnetic materials: the role of structural disorder, thermal relaxation, and dynamic effects." *Journal of Magnetism and Magnetic Materials* 2001, 226-230, (Pt. 2), 1206-1212.

15. Schwarz, J. A.; Contescu, C. I.; Putyera, K., *Dekker Encylcopedia of Nanoscience and Nanotechnology*. Marcel Dekker: 2004; Vol. 2.

16. Hergt, R.; Hiergeist, R.; Hilger, I.; Kaiser, W. A.; Lapatnikov, Y.; Margel, S.; Richter, U., "Maghemite nanoparticles with very high AC-losses for application in RF-magnetic hyperthermia." *Journal of Magnetism and Magnetic Materials* 2004, 270, (3), 345-357.

17. Aharoni, A., *Intoduction to the Theory of Ferromagnetism*. Clarendon Press: Oxford, 1996.

18. Fischer, B.; Huke, B.; Lucke, M.; Hempelmann, R., "Brownian relaxation of magnetic colloids." *Journal of Magnetism and Magnetic Materials* 2005, 289, 74-77.

19. Buschow, K. H. J.; De Boer, F. R., *Physics of Magnetism and Magnetic Materials*. Kluwer Academic/ Plenum Publishers New York, 2003.

20. Spaldin, N. A., *Magnetic materials: fundamentals and device applications*. Cambridge University Press: 2003.

21. Tilley, R. J. D., *Understanding Solids: the science of materials*. John Wiley and Sons Ltd: 2004.

22. Shriver, D. F.; Atkins, P. W.; Overton, T. L.; Rourke, J. P.; Weller, M. T.; Armstrong, F. A., *Inorganic Chemistry*. 4th Edition ed.; oxford University Press: Oxford, 2006.

23. Chikazumi, S., *Physics of Ferromagnetism*. 2nd Edition ed.; Oxford University Press: 1997.

24. Anderson, P. W., "Antiferromagnetism - Theory of Superexchange Interaction." *Physical Review* 1950, 79, (2), 350-356.

25. Smart, J. S., "The Néel Theory of Ferrimagnetism." *American Journal of Physics* 1955, 23, (6), 356-370.

26. Willard, M. A.; Kurihara, L. K.; Carpenter, E. E.; Calvin, S.; Harris, V. G., "Chemically prepared magnetic nanoparticles." *International Materials Reviews* 2004, 49, (3-4), 125-170.

27. Lai, W.; Wang, T.; Shem, J., "Theory of the Speromagnetism Phase-Transition." *Journal of Applied Physics* 1979, 50, (3), 1785-1786.

28. Coey, J. M. D.; Readman, P. W., "Characterisation and magnetic properties of natural ferric gel." *Earth and Planetary Science Letters* 1973, 21, (1), 45-51.

29. Coey, J. M. D.; Readman, P. W., "New Spin Structure in an Amorphous Ferric Gel." *Nature* 1973, 246, (5434), 476-478.

30. Coey, J. M. D., "Amorphous Magnetic Order." *Journal of Applied Physics* 1978, 49, (3), 1646-1652.

31. Tissier, B.; Buder, R.; Coey, J. M. D., "Domains in an Asperomagnet - Amorphous Dycu." *Journal of Magnetism and Magnetic Materials* 1980, 15-8, (JAN-), 1393-1394.

32. Coey, J. M. D.; Freitas, P. P.; Plaskett, T. S., "Giant Transverse Hysteresis in an Asperomagnet." *Physical Review B* 1990, 41, (13), 9585-9587.

33. du Trémolet de Lacheisserie E., G. D., Schlenker M., *Magnetism: Fundamentals*. Springer Science+Business Media Inc: 2005.

34. Pepperhoff, W.; Acet, M., *Constitution and Magnetism of Iron and its Alloys*. Springer: 2001.

35. Thain, M.; Hickman, M., *The Penguin Dictionary of Biology*. 11th Edition ed.; Penguin Books: 2004.

36. Symons, M. R. C.; Gutteridge, J. M. C., *Free radicals and iron: Chemistry, Biology and Medicine*. Oxford University Press: 1998.

37. Cornell R.M., S. U., *The Iron Oxides Structure Properties, Reactions, Occurrences and Uses*. 2nd Edition ed.; Wiley: Weinheim, 2003.

38. Mao, H. K.; Shu, J. F.; Fei, Y. W.; Hu, J. Z.; Hemley, R. J., "The wustite enigma". *Physics of the Earth and Planetary Interiors* 1996, 96, (2-3), 135-145.

39. Press, M. R.; Ellis, D. E., "Defect Clusters in Wustite $Fe_{1-X}O$." *Physical Review B* 1987, 35, (9), 4438-4454.

40. Ozdemir, O.; Dunlop, D. J.; Berquo, T. S., "Morin transition in hematite: Size dependence and thermal hysteresis." *Geochemistry Geophysics Geosystems* 2008, 9.

41. Danno, T.; Asaoka, H.; Nakanishi, M.; Fujii, T.; Ikeda, Y.; Kusano, Y.; Takada, J., "Formation mechanism of nano-crystalline β-Fe2O3 particles with bixbyite structure and their magnetic properties" *Journal of Physics: Conference Series* 2010, 200, (082003).

42. Dronskowski, R., The little maghemite story: A classic functional material. *Advanced Functional Materials* 2001, 11, (1), 27-29.

43. Verwey, E. J. W., "Electronic conduction of magnetite (Fe3O4) and its transition point at low temperatures." *Nature* 1939, 144, 327-8.

44. Rosencwaig, A., "Double exchange and the metal-nonmetal transition in magnetite." *Physical Review* 1969, 181, (2), 946-8.

45. Walz, F., "The Verwey transition-a topical review." *Journal of Physics: Condensed Matter* 2002, 14, (12), R285-R340.

46. Grimes, N. W., "Antiferroelectricity among compounds with spinel structure." *Journal of Physics C: Solid State Physics* 1973, 6, (4), L78-L79.

47. Heuer, A. H.; Mitchell, T. E., "Space group of spinel." *Journal of Physics C: Solid State Physics* 1975, 8, (23), L541-L543.

48. Schwertmann, U.; Cornell, R. M., *Iron Oxides in the Laboratory*. 2nd Edition ed.; Wiley-VCH: 2000.

49. Ramanujan, R. V.; Chong, W. T., "The synthesis and characterization of polymer coated iron oxide microspheres." *Journal of Materials Science: Materials in Medicine* 2004, 15, (8), 901-908.

50. Davila, A. F.; Winklhofer, M.; Shcherbakov, V. P.; Petersen, N., "Magnetic pulse affects a putative magnetoreceptor mechanism." *Biophysical Journal* 2005, 89, (1), 56-63.

51. Blakemore, R., "Magnetotactic Bacteria." *Science* 1975, 190, (4212), 377-379.

52. Faivre, D.; Schuler, D., "Magnetotactic Bacteria and Magnetosomes." *Chemical Reviews* 2008, 108, (11), 4875-4898.

53. Elmore, W. C., "Ferromagnetic colloid for studying magnetic structures." *Physical Review* 1938, 54, 309-10.

54. LaMer, V. K.; Dinegar, R. H., "Theory, Production and Mechanism of Formation of Monodispersed Hydrosols." *Journal of the American Chemical Society* 1950, 72, (11), 4847-4854.

55. Vengrenovitch, R. D., "On the Ostwald Ripening Theory." *Acta Metallurgica* 1982, 30, (6), 1079-1086.

56. Lifshitz, I. M.; Slyozov, V. V., "The Kinetics of Precipitation from Supersaturated Solid Solutions." *Journal of Physics and Chemistry of Solids* 1961, 19, (1-2), 35-50.

57. Bowker, M., "Surface science - The going rate for catalysts." *Nature Materials* 2002, 1, (4), 205-206.

58. Tavakoli, A.; Sohrabi, M.; Kargari, A., "A review of methods for synthesis of nanostructured metals with emphasis on iron compounds." *Chemical Papers* 2007, 61, (3), 151-170.

59. Ge, S.; Shi, X. Y.; Sun, K.; Li, C. P.; Uher, C.; Baker, J. R.; Holl, M. M. B.; Orr, B. G., "Facile Hydrothermal Synthesis of Iron Oxide Nanoparticles with Tunable Magnetic Properties." *Journal of Physical Chemistry C* 2009, 113, (31), 13593-13599.

60. Teja, A. S.; Koh, P. Y., "Synthesis, properties, and applications of magnetic iron oxide nanoparticles." *Progress in Crystal Growth and Characterization of Materials* 2009, 55, (1-2), 22-45.

61. Mooney, J. B.; Radding, S. B., "Spray Pyrolysis Processing." *Annual Review of Materials Science* 1982, 12, (1), 81-101.

62. Kodas, T.; Datye, A.; Lee, V.; Engler, E., "Single-Crystal $YBa_2Cu_3O_7$ Particle Formation by Aerosol Decomposition." *Journal of Applied Physics* 1989, 65, (5), 2149-2151.

63. Lu, Y.; Fan, H.; Stump, A.; Ward, T. L.; Rieker, T.; Brinker, C. J., "Aerosol-assisted self-assembly of mesostructured spherical nanoparticles." *Nature* 1999, 398, (6724), 223-226.

64. Xia, B.; Lenggoro, I. W.; Okuyama, K., "Novel route to nanoparticle synthesis by salt-assisted aerosol decomposition." *Advanced Materials* 2001, 13, (20), 1579-1582.

65. Gonzalez Carreno, T.; Mifsud, A.; Serna, C. J.; Palacios, J. M., "Preparation of homogeneous zinc/cobalt mixed oxides by spray pyrolysis." *Materials Chemistry and Physics* 1991, 27, (3), 287-96.

66. Gonzalez-Carreno, T.; Morales, M. P.; Gracia, M.; Serna, C. J., "Preparation of uniform γ-Fe_2O_3 particles with nanometer size by spray pyrolysis." *Materials Letters* 1993, 18, (3), 151-5.

67. Gurav, A.; Kodas, T.; Pluym, T.; Xiong, Y., "Aerosol processing of materials." *Aerosol Science and Technology* 1993, 19, (4), 411-52.

68. Wang, W. N.; Purwanto, A.; Lenggoro, I. W.; Okuyama, K.; Chang, H.; Jang, H. D., "Investigation on the correlations between droplet and particle size

distribution in ultrasonic spray pyrolysis." *Industrial & Engineering Chemistry Research* 2008, 47, (5), 1650-1659.

69. Miguel, O. B.; Morales, M. P.; Serna, C. J.; Veintemillas-Verdaguer, S., "Magnetic nanoparticles prepared by laser pyrolysis." *IEEE Transactions on Magnetics* 2002, 38, (5, Pt. 1), 2616-2618.

70. Veintemillas-Verdaguer, S.; Morales, M. P.; Serna, C. J., "Effect of the oxidation conditions on the maghemite produced by laser pyrolysis." *Applied Organometallic Chemistry* 2001, 15, (5), 365-372.

71. Veintemillas-Verdaguer, S.; Morales, M. P.; Serna, C. J., "Continuous production of gamma-Fe2O3 ultrafine powders by laser pyrolysis." *Materials Letters* 1998, 35, (3-4), 227-231.

72. Atkins, P. W.; Jones, L. L., *Chemical principles: the quest for insight*. 3rd Edition ed.; W.H. Freeman and Company: 2005.

73. Gupta, A. K.; Gupta, M., "Synthesis and surface engineering of iron oxide nanoparticles for biomedical applications." *Biomaterials* 2005, 26, (18), 3995-4021.

74. Kinoshita, T.; Seino, S.; Okitsu, K.; Nakayama, T.; Nakagawa, T.; Yamamoto, T. A., "Magnetic evaluation of nanostructure of gold-iron composite particles synthesized by a reverse micelle method." *Journal of Alloys and Compounds* 2003, 359, 46-50.

75. Muller, R.; Steinmetz, H.; Hiergeist, R.; Gawalek, W., "Magnetic particles for medical applications by glass crystallisation." *Journal of Magnetism and Magnetic Materials* 2004, 272-276, (Pt. 2), 1539-1541.

76. Dunlop, D. J., "Superparamagnetic and Single-Domain Threshold Sizes in Magnetite." *Journal of Geophysical Research* 1973, 78, (11), 1780-1793.

77. Dunlop, D. J., Magnetite. "Behavior near the single-domain threshold." *Science)* 1972, 176, (4030), 41-3.

78. Ramanujan, R. V. In *Clinical Applications of Magnetic Nanomaterials*, Proceedings of the First International Bioengineering Conference, Singapore, 2004; Fuss F.K., C. S. L., Venkatraman S.S., Krishnan S.M., Schmidt B., Ed. Singapore, 2004; p 174.

79. Majewski, P.; Thierry, B., "Functionalized magnetite nanoparticles - Synthesis, properties, and bio-applications." *Critical Reviews in Solid State and Materials Sciences* 2007, 32, (3-4), 203-215.

80. Berger, P.; Adelman, N. B.; Beckman, K. J.; Campbell, D. J.; Ellis, A. B.; Lisensky, G. C., "Preparation and properties of an aqueous ferrofluid." *Journal of Chemical Education* 1999, 76, (7), 943-948.

81. Davis, S. S., "Biomedical applications of nanotechnology - Implications for drug targeting and gene therapy." *Trends in Biotechnology* 1997, 15, (6), 217-224.

82. Burgos-Asperilla, L.; Darder, M.; Aranda, P.; Vazquez, L.; Vazquez, M.; Ruiz-Hitzky, E., "Novel magnetic organic-inorganic nanostructured materials." *Journal of Materials Chemistry* 2007, 17, (40), 4233-4238.

83. Harris, L. A.; Goff, J. D.; Carmichael, A. Y.; Riffle, J. S.; Harburn, J. J.; St Pierre, T. G.; Saunders, M., "Magnetite nanoparticle dispersions stabilized with triblock copolymers." *Chemistry of Materials* 2003, 15, (6), 1367-1377.

84. Pradhan, P.; Giri, J.; Banerjee, R.; Bellare, J.; Bahadur, D., "Cellular interactions of lauric acid and dextran-coated magnetite nanoparticles." *Journal of Magnetism and Magnetic Materials* 2007, 311, (1), 282-287.

85. Sonvico, F.; Mornet, S.; Vasseur, S.; Dubernet, C.; Jaillard, D.; Degrouard, J.; Hoebeke, J.; Duguet, E.; Colombo, P.; Couvreur, P., "Folate-Conjugated Iron Oxide

Nanoparticles for Solid Tumor Targeting as Potential Specific Magnetic Hyperthermia Mediators: Synthesis, Physicochemical Characterization, and in Vitro Experiments." *Bioconjugate Chemistry* 2005, 16, (5), 1181-1188.

86. Jain Tapan, K.; Morales Marco, A.; Sahoo Sanjeeb, K.; Leslie-Pelecky Diandra, L.; Labhasetwar, V., "Iron oxide nanoparticles for sustained delivery of anticancer agents." *Molecular pharmaceutics* 2005, 2, (3), 194-205.

87. Berry, C. C.; Curtis, A. S. G., "Functionalisation of magnetic nanoparticles for applications in biomedicine." *Journal of Physics D-Applied Physics* 2003, 36, (13), R198-R206.

88. Torchilin, V. P., Weissig, V., *Liposomes*. 2nd Edition ed.; Oxford University Press: Oxford, 2003.

89. Yatvin, M. B.; Weinstein, J. N.; Dennis, W. H.; Blumenthal, R., "Design of liposomes for enhanced local release of drugs by hyperthermia." *Science* 1978, 202, (4374), 1290-3.

90. Hodenius, M.; De Cuyper, M.; Desender, L.; Muller-Schulte, D.; Steigel, A.; Lueken, H., "Biotinylated Stealth magnetoliposomes." *Chemistry and Physics of Lipids* 2002, 120, (1-2), 75-85.

91. Gabizon, A.; Shmeeda, H.; Horowitz, A. T.; Zalipsky, S., "Tumor cell targeting of liposome-entrapped drugs with phospholipid-anchored folic acid-PEG conjugates." *Advanced Drug Delivery Reviews* 2004, 56, (8), 1177-1192.

92. Shinkai, M.; Yanase, M.; Honda, H.; Wakabayashi, T.; Yoshida, J.; Kobayashi, T., "Intracellular hyperthermia for cancer using magnetite cationic liposomes: in vitro study." *Japanese Journal of Cancer Research* 1996, 87, (11), 1179-1183.

93. Shinkai, M.; Yanase, M.; Suzuki, M.; Honda, H.; Wakabayashi, T.; Yoshida, J.; Kobayashi, T., "Intracellular hyperthermia for cancer using magnetite cationic liposomes." *Journal of Magnetism and Magnetic Materials* 1999, 194, (1-3), 176-184.

94. Kong, G.; Dewhirst, M. W., "Hyperthermia and liposomes". *International Journal of Hyperthermia* 1999, 15, (5), 345-370.

95. De, M.; Ghosh, P. S.; Rotello, V. M., "Applications of Nanoparticles in Biology." *Advanced Materials* 2008, 20, (22), 4225-4241.

96. Sun, C.; Lee, J. S. H.; Zhang, M. Q., "Magnetic nanoparticles in MR imaging and drug delivery." *Advanced Drug Delivery Reviews* 2008, 60, (11), 1252-1265.

97. Mornet, S.; Vasseur, S.; Grasset, F.; Duguet, E., "Magnetic nanoparticle design for medical diagnosis and therapy." *Journal of Materials Chemistry* 2004, 14, (14), 2161-2175.

98. Babes, L.; Denizot, B.; Tanguy, G.; Le Jeune, J. J.; Jallet, P., "Synthesis of iron oxide nanoparticles used as MRI contrast agents: A parametric study." *Journal of Colloid and Interface Science* 1999, 212, (2), 474-482.

99. Neuberger, T.; Schopf, B.; Hofmann, H.; Hofmann, M.; von Rechenberg, B., "Superparamagnetic nanoparticles for biomedical applications: Possibilities and limitations of a new drug delivery system." *Journal of Magnetism and Magnetic Materials* 2005, 293, (1), 483-496.

100. Tiefenauer, L. X.; Kuehne, G.; Andres, R. Y., "Antibody-magnetite nanoparticles: In vitro characterization of a potential tumor-specific contrast agent for magnetic resonance imaging." *Bioconjugate Chemistry* 1993, 4, (5), 347-52.

101. Paul, F.; Melville, D.; Roath, S.; Warhurst, D. C., "A Bench Top Magnetic Separator for Malarial Parasite Concentration." *Ieee Transactions on Magnetics* 1981, 17, (6), 2822-2824.

102. Liberti, P. A.; Rao, C. G.; Terstappen, L., "Optimization of ferrofluids and protocols for the enrichment of breast tumor cells in blood." *Journal of Magnetism and Magnetic Materials* 2001, 225, (1-2), 301-307.

103. Pankhurst, Q. A.; Connolly, J.; Jones, S. K.; Dobson, J., "Applications of magnetic nanoparticles in biomedicine." *Journal of Physics D: Applied Physics* 2003, 36, (13), R167-R181.

104. Tartaj, P.; Morales, M. d. P.; Veintemillas-Verdaguer, S.; Gonzalez-Carreno, T.; Serna, C. J., "The preparation of magnetic nanoparticles for applications in biomedicine." *Journal of Physics D: Applied Physics* 2003, 36, (13), R182-R197.

105. Jordan, A.; Scholz, R.; Wust, P.; Schirra, H.; Schiestel, T.; Schmidt, H.; Felix, R., "Endocytosis of dextran and silan-coated magnetite nanoparticles and the effect of intracellular hyperthermia on human mammary carcinoma cells in vitro." *Journal of Magnetism and Magnetic Materials* 1999, 194, (1-3), 185-196.

106. Johannsen, M.; Gneveckow, U.; Eckelt, L.; Feussner, A.; Waldofner, N.; Scholz, R.; Deger, S.; Wust, P.; Loening, S. A.; Jordan, A., "Clinical hyperthermia of prostate cancer using magnetic nanoparticles: Presentation of a new interstitial technique." *International Journal of Hyperthermia* 2005, 21, (7), 637-647.

107. Ito, A.; Fujioka, M.; Yoshida, T.; Wakamatsu, K.; Ito, S.; Yamashita, T.; Jimbow, K.; Honda, H., "4-S-cysteaminylphenol-loaded magnetite cationic liposomes for combination therapy of hyperthermia with chemotherapy against malignant melanoma." *Cancer Science* 2007, 98, (3), 424-430.

108. Gazeau, F.; Levy, M.; Wilhelm, C., "Optimizing magnetic nanoparticle design for nanothermotherapy." *Nanomedicine* 2008, 3, (6), 831-844.

109. Bahadur, D.; Giri, J., "Biomaterials and magnetism." In 2003; pp 639-656.

110. Cancer Research UK, Incidence Statistics 2004. Available from: http://info.cancerresearchuk.org/cancerstats/incidence/?a=5441UK Cancer [Last accessed 22nd May 2008].

111. Knowles, M. A.; Selby P.J., *Introduction to the Cellular and Molecular Biology of Cancer*. 4th Edition ed.; Oxford University Press: 2005.

112. DNA Learning Center, Inside Cancer. Available From: http://www.insidecancer.org/. [Last accessed 6th June 2010].

113. Campbell, N. A. R., Jane B. , *Biology*. 6th Edition ed.; Pearson Education Inc: San Francisco, 2002.

114. Macmillian Cancer Support, Cancer Treatments. Available from: http://www.macmillan.org.uk/Cancerinformation/Cancertreatment/Treatments.aspx. [Last accessed 6th June 2010].

115. Hergt, R.; Dutz, S.; Mueller, R.; Zeisberger, M., "Magnetic particle hyperthermia: nanoparticle magnetism and materials development for cancer therapy." *Journal of Physics: Condensed Matter* 2006, 18, (38), S2919-S2934.

116. Yanase, M.; Shinkai, M.; Honda, H.; Wakabayashi, T.; Yoshida, J.; Kobayashi, T., "Intracellular hyperthermia for cancer using magnetite cationic liposomes: Ex vivo study." *Japanese Journal of Cancer Research* 1997, 88, (7), 630-632.

117. Song, H. T.; Choi, J. S.; Huh, Y. M.; Kim, S.; Jun, Y. W.; Suh, J. S.; Cheon, J., "Surface modulation of magnetic nanocrystals in the development of highly efficient

magnetic resonance probes for intracellular labeling." *Journal of the American Chemical Society* 2005, 127, (28), 9992-9993.

118. Weissleder, R.; Stark, D. D.; Engelstad, B. L.; Bacon, B. R.; Compton, C. C.; White, D. L.; Jacobs, P.; Lewis, J., "Superparamagnetic Iron-Oxide - Pharmacokinetics and Toxicity." *American Journal of Roentgenology* 1989, 152, (1), 167-173.

119. Soenen, S. J.; De Cuyper, M., "Assessing iron oxide nanoparticle toxicity in vitro: current status and future prospects." *Nanomedicine (Lond)* 5, (8), 1261-75.

120. Tran, N.; Webster, T. J., "Magnetic nanoparticles: biomedical applications and challenges." *Journal of Materials Chemistry* 20, (40), 8760-8767.

121. Green, R.; Charlton, R.; Seftel, H.; Bothwell, T.; Mayet, F.; Adams, B.; Finch, C.; Layrisse, M., "Body Iron Excretion in Man - a Collaborative Study." *American Journal of Medicine* 1968, 45, (3), 336-&.

122. Cook, J. D.; Skikne, B. S.; Lynch, S. R.; Reusser, M. E., "Estimates of Iron Sufficiency in the United-States Population." *Blood* 1986, 68, (3), 726-731.

123. Craik, D., *Magnetism: principles and applications*. John Wiley and Sons: 1995.

124. Jenks, W. G.; Sadeghi, S. S. H.; Wikswo, J. P., "SQUIDs for nondestructive evaluation." *Journal of Physics D-Applied Physics* 1997, 30, (3), 293-323.

125. Silver, A. H.; Zimmerma.Je, "Quantum States and Transitions in Weakly Connected Superconducting Rings." *Physical Review* 1967, 157, (2), 317-&.

126. Ryhanen, T.; Seppa, H.; Ilmoniemi, R.; Knuutila, J., "Squid Magnetometers for Low-Frequency Applications." *Journal of Low Temperature Physics* 1989, 76, (5-6), 287-386.

127. Josephson, B. D., "Possible New Effects in Superconductive Tunnelling." *Physics Letters* 1962, 1, (7), 251-253.

128. Koelle, D.; Kleiner, R.; Ludwig, F.; Dantsker, E.; Clarke, J., "High-transition-temperature superconducting quantum interference devices." *Reviews of Modern Physics* 1999, 71, (3), 631-686.

129. Liu, Y.; Sellmyer, D. J.; Shindo, D., *Handbook of Advanced Magnetic Materials*. Springer: 2006; Vol. Volume 1: Nanostructural effects.

130. Baker, I.; Zeng, Q.; Li, W.; Sullivan, C. R., "Heat deposition in iron oxide and iron nanoparticles for localized hyperthermia." *Journal of Applied Physics* 2006, 99, (8, Pt. 2), 08H106/1-08H106/3.

131. Chou, C. K., "Use of Heating Rate and Specific Absorption Rate in the Hyperthermia Clinic." *International Journal of Hyperthermia* 1990, 6, (2), 367-370.

132. Babincova, M.; Leszczynska, D.; Sourivong, P.; Cicmanec, P.; Babinec, P., "Superparamagnetic gel as a novel material for electromagnetically induced hyperthermia." *Journal of Magnetism and Magnetic Materials* 2001, 225, (1-2), 109-112.

133. Kallumadil, M.; Tada, M.; Nakagawa, T.; Abe, M.; Southern, P.; Pankhurst, Q. A., "Suitability of commercial colloids for magnetic hyperthermia." *Journal of Magnetism and Magnetic Materials* 2009, 321, (10), 1509-1513.

134. Atkinson, W. J.; Brezovich, I. A.; Chakraborty, D. P., Usable Frequencies in "Hyperthermia with Thermal Seeds." *Ieee Transactions on Biomedical Engineering* 1984, 31, (1), 70-75.

135. Glockl, G.; Hergt, R.; Zeisberger, M.; Dutz, S.; Nagel, S.; Weitschies, W., "The effect of field parameters, nanoparticle properties and immobilization on the

specific heating power in magnetic particle hyperthermia." *Journal of Physics-Condensed Matter* 2006, 18, (38), S2935-S2949.

136. Hergt, R.; Dutz, S., "Magnetic particle hyperthermia-biophysical limitations of a visionary tumour therapy." *Journal of Magnetism and Magnetic Materials* 2007, 311, (1), 187-192.

137. Massart, R.; Cabuil, V., "Effect of Some Parameters on the Formation of Colloidal Magnetite in Alkaline-Medium - Yield and Particle-Size Control." *Journal De Chimie Physique Et De Physico-Chimie Biologique* 1987, 84, (7-8), 967-973.

138. Verges, M. A.; Costo, R.; Roca, A. G.; Marco, J. F.; Goya, G. F.; Serna, C. J.; Morales, M. P., "Uniform and water stable magnetite nanoparticles with diameters around the monodomain-multidomain limit." *Journal of Physics D-Applied Physics* 2008, 41, (13).

139. Turkevich, J.; Stevenson, P. C.; Hillier, J., "A Study of the Nucleation and Growth Processes in the Synthesis of Colloidal Gold." *Discussions of the Faraday Society* 1951, (11), 55-&.

140. Watzky, M. A.; Finke, R. G., "Transition metal nanocluster formation kinetic and mechanistic studies. A new mechanism when hydrogen is the reductant: Slow, continuous nucleation and fast autocatalytic surface growth." *Journal of the American Chemical Society* 1997, 119, (43), 10382-10400.

141. Park, J.; Lee, E.; Hwang, N. M.; Kang, M. S.; Kim, S. C.; Hwang, Y.; Park, J. G.; Noh, H. J.; Kini, J. Y.; Park, J. H.; Hyeon, T., "One-nanometer-scale size-controlled synthesis of monodisperse magnetic iron oxide nanoparticles." *Angewandte Chemie-International Edition* 2005, 44, (19), 2872-2877.

142. Tiemann, M.; Marlow, F.; Hartikainen, J.; Weiss, O.; Linden, M., "Ripening effects in ZnS nanoparticle growth." *Journal of Physical Chemistry C* 2008, 112, (5), 1463-1467.

143. Tan, Y. W.; Zhuang, Z. B.; Peng, Q.; Li, Y. D., "Room-temperature soft magnetic iron oxide nanocrystals: Synthesis, characterization, and size-dependent magnetic properties." *Chemistry of Materials* 2008, 20, (15), 5029-5034.

144. Chin, S. F.; Makha, M.; Raston, C. L.; Saunders, M., 2Magnetite ferrofluids stabilized by sulfonato-calixarenes." *Chemical Communications* 2007, (19), 1948-1950.

145. Giri, J.; Thakurta, S. G.; Bellare, J.; Nigam, A. K.; Bahadur, D., "Preparation and characterization of phospholipid stabilized uniform sized magnetite nanoparticles." *Journal of Magnetism and Magnetic Materials* 2005, 293, (1), 62-68.

146. Min, Y.; Akbulut, M.; Kristiansen, K.; Golan, Y.; Israelachvili, J., "The role of interparticle and external forces in nanoparticle assembly." *Nature Materials* 2008, 7, (7), 527-538.

147. Jolivet, J. P.; Tronc, E.; Chaneac, C., "Synthesis of iron oxide- and metal-based nanomaterials." *European Physical Journal-Applied Physics* 2000, 10, (3), 167-172.

148. Banfield, J. F.; Welch, S. A.; Zhang, H.; Ebert, T. T.; Penn, R. L., "Aggregation-Based Crystal Growth and Microstructure Development in Natural Iron Oxyhydroxide Biomineralization Products." *Science* 2000, 289, (5480), 751-754.

149. Penn, R. L.; Banfield, J. F., "Imperfect Oriented Attachment: Dislocation Generation in Defect-Free Nanocrystals." *Science* 1998, 281, (5379), 969-971.

150. Boistelle, R., "Fundamentals of Nucleation and Crystal Growth". *Garti, N. and K. Sato (Ed.). Surfactant Science Series, Vol. 31. Crystallization and Polymorphism of Fats and Fatty Acids.* 1988, 189-226.

151. Yan, F.; Xu, H.; Anker, J.; Kopelman, R.; Ross, B.; Rehemtulla, A.; Reddy, R., "Synthesis and characterization of silica-embedded iron oxide nanoparticles for magnetic resonance imaging." *Journal of Nanoscience and Nanotechnology* 2004, 4, (1-2), 72-76.

152. Moreno, E. M.; Zayat, M.; Morales, M. P.; Serna, C. J.; Roig, A.; Levy, D., "Preparation of narrow size distribution superparamagnetic g-Fe2O3 nanoparticles in a sol-gel transparent SiO2 matrix." *Langmuir* 2002, 18, (12), 4972-4978.

153. Bumb, A.; Brechbiel, M. W.; Choyke, P. L.; Fugger, L.; Eggeman, A.; Prabhakaran, D.; Hutchinson, J.; Dobson, P. J., "Synthesis and characterization of ultra-small superparamagnetic iron oxide nanoparticles thinly coated with silica." *Nanotechnology* 2008, 19, (33).

154. Lalatonne, Y.; Paris, C.; Serfaty, J. M.; Weinmann, P.; Lecouvey, M.; Motte, L., "Bis-phosphonates - ultra small superparamagnetic iron oxide nanoparticles: a platform towards diagnosis and therapy." *Chemical Communications* 2008, (22), 2553-2555.

155. Portet, D.; Denizot, B.; Rump, E.; Lejeune, J. J.; Jallet, P., "Nonpolymeric coatings of iron oxide colloids for biological use as magnetic resonance imaging contrast agents." *Journal of Colloid and Interface Science* 2001, 238, (1), 37-42.

156. Portet, D.; Denizot, B.; Rump, E.; Hindre, F.; Le Jeune, J. J.; Jallet, P., "Comparative biodistribution of thin-coated iron oxide nanoparticles TCION: Effect of different bisphosphonate coatings." *Drug Development Research* 2001, 54, (4), 173-181.

157. Sahoo, Y.; Pizem, H.; Fried, T.; Golodnitsky, D.; Burstein, L.; Sukenik, C. N.; Markovich, G., "Alkyl phosphonate/phosphate coating on magnetite nanoparticles: A comparison with fatty acids." *Langmuir* 2001, 17, (25), 7907-7911.

158. Wan, S. R.; Huang, J. S.; Yan, H. S.; Liu, K. L., "Size-controlled preparation of magnetite nanoparticles in the presence of graft copolymers." *Journal of Materials Chemistry* 2006, 16, (3), 298-303.

159. Kohler, N.; Fryxell, G. E.; Zhang, M. Q., "A bifunctional poly(ethylene glycol) silane immobilized on metallic oxide-based nanoparticles for conjugation with cell targeting agents." *Journal of the American Chemical Society* 2004, 126, (23), 7206-7211.

160. Gupta, A. K.; Wells, S., "Surface-modified superparamagnetic nanoparticles for drug delivery: Preparation, characterization, and cytotoxicity studies." *Ieee Transactions on Nanobioscience* 2004, 3, (1), 66-73.

161. Zalipsky, S.; Mullah, N.; Harding, J. A.; Gittelman, J.; Guo, L.; DeFrees, S. A., "Poly(ethylene glycol)-grafted liposomes with oligopeptide or oligosaccharide ligands appended to the termini of the polymer chains." *Bioconjugate Chemistry* 1997, 8, (2), 111-118.

162. Chen, S.; Li, Y.; Guo, C.; Wang, J.; Ma, J. H.; Liang, X. F.; Yang, L. R.; Liu, H. Z., "Temperature-responsive magnetite/PEO-PPO-PEO block copolymer nanoparticles for controlled drug targeting delivery." *Langmuir* 2007, 23, 12669-12676.

163. Samanta, B.; Yan, H.; Fischer, N. O.; Shi, J.; Jerry, D. J.; Rotello, V. M., "Protein-passivated Fe3O4 nanoparticles: low toxicity and rapid heating for thermal therapy." *Journal of Materials Chemistry* 2008, 18, (11), 1204-1208.

164. Li, G. Y.; Huang, K. L.; Jiang, Y. R.; Ding, P.; Yang, D. L., "Preparation and characterization of carboxyl functionalization of chitosan derivative magnetic nanoparticles." *Biochemical Engineering Journal* 2008, 40, (3), 408-414.

165. Peng, Z. G.; Hidajat, K.; Uddin, M. S., "Adsorption of bovine serum albumin on nanosized magnetic particles." *Journal of Colloid and Interface Science* 2004, 271, (2), 277-283.

166. Ivanova, E. P.; Papiernik, M.; Oliveira, A.; Sbarski, I.; Smekal, T.; Grodzinski, P.; Nicolau, D. V., "Feasibility of using carboxylic-rich polymeric surfaces for the covalent binding of oligonucleotides for microPCR applications." *Smart Materials & Structures* 2002, 11, (5), 783-791.

167. Yu, S.; Chow, G. M., "Carboxyl group (-CO_2H) functionalized ferrimagnetic iron oxide nanoparticles for potential bio-applications." *Journal of Materials Chemistry* 2004, 14, (18), 2781-2786.

168. Chen, Z. P.; Zhang, Y.; Zhang, S.; Xia, J. G.; Liu, J. W.; Xu, K.; Gu, N., "Preparation and characterization of water-soluble monodisperse magnetic iron oxide nanoparticles via surface double-exchange with DMSA." *Colloids and Surfaces a-Physicochemical and Engineering Aspects* 2008, 316, (1-3), 210-216.

169. Decuyper, M.; Joniau, M., "Mechanistic Aspects of the Adsorption of Phospholipids onto Lauric Acid Stabilized Fe_3O_4 Nanocolloids." *Langmuir* 1991, 7, (4), 647-652.

170. Avdeev, M. V.; Bica, D.; Vekas, L.; Marinica, O.; Balasoiu, M.; Aksenov, V. L.; Rosta, L.; Garamus, V. M.; Schreyer, A., "On the possibility of using short chain length mono-carboxylic acids for stabilization of magnetic fluids." *Journal of Magnetism and Magnetic Materials* 2007, 311, (1), 6-9.

171. Mohapatra, S.; Mallick, S. K.; Maiti, T. K.; Ghosh, S. K.; Pramanik, P., "Synthesis of highly stable folic acid conjugated magnetite nanoparticles for targeting cancer cells." *Nanotechnology* 2007, 18, (38).

172. Dancer, S. J., "Importance of the environment in meticillin-resistant Staphylococcus aureus acquisition: the case for hospital cleaning." *Lancet Infectious Diseases* 2008, 8, (2), 101-113.

173. Page, K.; Wilson, M.; Parkin, I. P., "Antimicrobial surfaces and their potential in reducing the role of the inanimate environment in the incidence of hospital-acquired infections." *Journal of Materials Chemistry* 2009, 19, (23), 3819-3831.

174. Page, K.; Palgrave, R. G.; Parkin, I. P.; Wilson, M.; Savin, S. L. P.; Chadwick, A. V., "Titania and silver-titania composite films on glass-potent antimicrobial coatings." *Journal of Materials Chemistry* 2007, 17, (1), 95-104.

175. Narband, N.; Mubarak, M.; Ready, D.; Parkin, I. P.; Nair, S. P.; Green, M. A.; Beeby, A.; Wilson, M., "Quantum dots as enhancers of the efficacy of bacterial lethal photosensitization." *Nanotechnology* 2008, 19, (44).

176. Narband, N.; Tubby, S.; Parkin, I. P.; Gil-Tomas, J.; Ready, D.; Nair, S. P.; Wilson, M., "Gold Nanoparticles Enhance the Toluidine Blue-Induced Lethal Photosensitisation of *Staphylococcus aureus*." *Current Nanoscience* 2008, 4, (4), 409-414.

177. Gil-Tomas, J.; Tubby, S.; Parkin, I. P.; Narband, N.; Dekker, L.; Nair, S. P.; Wilson, M.; Street, C., "Lethal photosensitisation of *Staphylococcus aureus* using a toluidine blue O-tiopronin-gold nanoparticle conjugate." *Journal of Materials Chemistry* 2007, 17, (35), 3739-3746.

178. Kim, G. H.; Kellner, C. P.; Hickman, Z. L.; Zacharia, B. E.; Starke, R. M.; Hwang, B. Y.; Ducruet, A. F.; Fernandez, L.; Mayer, S. A.; Tracey, K. J.; Connolly, E. S., "A phase I clinical trial of tiopronin, a putative neuroprotective agent, in aneurysmal subarachnoid hemorrhage." *Neurosurgery* 67, (1), 182-6.

179. Tiselius, H. G., "New horizons in the management of patients with cystinuria." *Current Opinion in Urology* 20, (2), 169-173.

180. Zhang, M.; Wong, I. G.; Gin, J. B.; Ansari, N. H., "Assessment of methylsulfonylmethane as a permeability enhancer for regional EDTA chelation therapy." *Drug Delivery* 2009, 16, (5), 243-248.

181. House, E.; Collingwood, J.; Khan, A.; Korchazkina, O.; Berthon, G.; Exley, C., "Aluminium, iron, zinc and copper influence the in vitro formation of amyloid fibrils of A beta(42) in a manner which may have consequences for metal chelation therapy in Alzheimer's disease." *Journal of Alzheimers Disease* 2004, 6, (3), 291-301.

182. Hagiwara, M.; Watanabe, E.; Barrett, J. C.; Tsutsui, T., "Assessment of genotoxicity of 14 chemical agents used in dental practice: Ability to induce chromosome aberrations in Syrian hamster embryo cells." *Mutation Research-Genetic Toxicology and Environmental Mutagenesis* 2006, 603, (2), 111-120.

183. Daou, T. J.; Pourroy, G.; Begin-Colin, S.; Greneche, J. M.; Ulhaq-Bouillet, C.; Legare, P.; Bernhardt, P.; Leuvrey, C.; Rogez, G., "Hydrothermal Synthesis of Monodisperse Magnetite Nanoparticles." *Chemistry of Materials* 2006, 18, (18), 4399-4404.

184. Jung, C. W.; Jacobs, P., "Physical and Chemical-Properties of Superparamagnetic Iron-Oxide Mr Contrast Agents - Ferumoxides, Ferumoxtran, Ferumoxsil." *Magnetic Resonance Imaging* 1995, 13, (5), 661-674.

185. Cheng, F. Y.; Su, C. H.; Yang, Y. S.; Yeh, C. S.; Tsai, C. Y.; Wu, C. L.; Wu, M. T.; Shieh, D. B., "Characterization of aqueous dispersions of Fe3O4 nanoparticles and their biomedical applications." *Biomaterials* 2005, 26, (7), 729-738.

186. Rubim, J. C.; Sousa, M. H.; Silva, J. C. O.; Tourinho, F. A., "Raman spectroscopy as a powerful technique in the characterization of ferrofluids." *Brazilian Journal of Physics* 2001, 31, (3), 402-408.

187. Jubb, A. M.; Allen, H. C., "Vibrational Spectroscopic Characterization of Hematite, Maghemite, and Magnetite Thin Films Produced by Vapor Deposition." *Acs Applied Materials & Interfaces* 2, (10), 2804-2812.

188. Shebanova, O. N.; Lazor, P., "Raman spectroscopic study of magnetite (FeFe2O4): a new assignment for the vibrational spectrum." *Journal of Solid State Chemistry* 2003, 174, 424-430.

189. Ozdemir, O.; Dunlop, D. J.; Moskowitz, B. M., "The effect of oxidation on the Verwey transition in magnetite." *Geophysical Research Letters* 1993, 20, (16), 1671-4.

190. Prozorov, R.; Prozorov, T.; Mallapragada, S. K.; Narasimhan, B.; Williams, T. J.; Bazylinski, D. A., "Magnetic irreversibility and the Verwey transition in nanocrystalline bacterial magnetite." *Physical Review B: Condensed Matter and Materials Physics* 2007, 76, (5), 054406/1-054406/10.

191. Russell, R. G. G.; Rogers, M. J., "Bisphosphonates: From the laboratory to the clinic and back again." *Bone* 1999, 25, (1), 97-106.

192. Wang, L.; Yang, Z. M.; Gao, J. H.; Xu, K. M.; Gu, H. W.; Zhang, B.; Zhang, X. X.; Xu, B., "A biocompatible method of decorporation: Bisphosphonate-modified magnetite nanoparticles to remove uranyl ions from blood." *Journal of the American Chemical Society* 2006, 128, (41), 13358-13359.

193. Shafi, K.; Ulman, A.; Yan, X. Z.; Yang, N. L.; Estournes, C.; White, H.; Rafailovich, M., "Sonochemical synthesis of functionalized amorphous iron oxide nanoparticles." *Langmuir* 2001, 17, (16), 5093-5097.

194. Yee, C.; Kataby, G.; Ulman, A.; Prozorov, T.; White, H.; King, A.; Rafailovich, M.; Sokolov, J.; Gedanken, A., "Self-assembled monolayers of

alkanesulfonic and -phosphonic acids on amorphous iron oxide nanoparticles." *Langmuir* 1999, 15, (21), 7111-7115.

195. Ngo, A. T.; Bonville, P.; Pileni, M. P., "Nanoparticles of CoxFey square O-z(4): Synthesis and superparamagnetic properties." *European Physical Journal B* 1999, 9, (4), 583-592.

196. Daou, T. J.; Greneche, J. M.; Pourroy, G.; Buathong, S.; Derory, A.; Ulhaq-Bouillet, C.; Donnio, B.; Guillon, D.; Begin-Colin, S., "Coupling agent effect on magnetic properties of functionalized magnetite-based nanoparticles." *Chemistry of Materials* 2008, 20, (18), 5869-5875.

197. Pawsey, S.; Yach, K.; Reven, L., "Self-assembly of carboxyalkylphosphonic acids on metal oxide powders." *Langmuir* 2002, 18, (13), 5205-5212.

198. Georgelin, T.; Moreau, B.; Bar, N.; Villemin, D.; Cabuil, V.; Horner, O., "Functionalization of gamma-Fe_2O_3 nanoparticles through the grafting of an organophosphorous ligand." *Sensors and Actuators B-Chemical* 2008, 134, (2), 451-454.

199. Benyettou, F.; Lalatonne, Y.; Sainte-Catherine, O.; Monteil, M.; Motte, L., "Superparamagnetic nanovector with anti-cancer properties: gamma Fe_2O_3@Zoledronate." *International Journal of Pharmaceutics* 2009, 379, (2), 324-327.

200. Russell, R. G. G.; Smith, R.; Preston, C.; Walton, R. J.; Woods, C. G., "Diphosphonates in Pagets-Disease." *Lancet* 1974, 1, (7863), 894-898.

201. Diamond, T.; Campbell, J.; Bryant, C.; Lynch, W., "The effect of combined androgen blockade on bone turnover and bone mineral densities in men treated for prostate carcinoma - Longitudinal evaluation and response to intermittent cyclic etidronate therapy." *Cancer* 1998, 83, (8), 1561-1566.

202. Mulder, H.; Struys, A., "Intermittent Cyclical Etidronate in the Prevention of Corticosteroid-Induced Bone Loss." *British Journal of Rheumatology* 1994, 33, (4), 348-350.

203. Service, N. H., Paget's disease. In NHS, UK: 2010.

204. Jaggard, K. W., "Some Effects of Growth-Retardant Glyphosine [N,N-Bis (Phosphonomethyl) Glycine] on Sugar-Beet Crop." *Annals of Applied Biology* 1975, 79, (3), 343-&.

205. Podesta, F. E.; Gonzalez, D. H.; Andreo, C. S., "Glyphosine Inhibits Maize Leaf Phosphoenolpyruvate Carboxylase." *Plant and Cell Physiology* 1987, 28, (2), 375-378.

206. Galanski, M.; Slaby, S.; Jakupec, M. A.; Keppler, B. K., "Synthesis, characterization, and in vitro antitumor activity of osteotropic diam(m)ineplatinum(II) complexes bearing a N,N-bis(phosphonomethyl)glycine ligand." *Journal of Medicinal Chemistry* 2003, 46, (23), 4946-4951.

207. Bauer, S.; Muller, H.; Bein, T.; Stock, N., "Synthesis and characterization of the open-framework barium bisphosphonate [$Ba_3(O_3PCH_2NH_2CH_2PO_3)_2(H_2O)_4$].$3H_2O$." *Inorganic Chemistry* 2005, 44, (25), 9464-9470.

208. Juillard, A.; Falgayrac, G.; Cortet, B.; Vieillard, M. H.; Azaroual, N.; Hornez, J. C.; Penel, G., "Molecular interactions between zoledronic acid and bone: An in vitro Raman microspectroscopic study." *Bone* 47, (5), 895-904.

209. Widler, L.; Jaeggi, K. A.; Glatt, M.; Muller, K.; Bachmann, R.; Bisping, M.; Born, A. R.; Cortesi, R.; Guiglia, G.; Jeker, H.; Klein, R.; Ramseier, U.; Schmid, J.; Schreiber, G.; Seltenmeyer, Y.; Green, J. R., "Highly potent geminal

bisphosphonates. From pamidronate disodium (Aredia) to zoledronic acid (Zometa)." *Journal of Medicinal Chemistry* 2002, 45, (17), 3721-3738.

210. White, L., *Foundations of Nursing*. 2nd Edition ed.; Thomson Delmar Learning: 2005.